ABSTRACT

Title of Document: LOCAL MEASUREMENT AND CHARACTERIZATION VIA FLUORESCING MATERIALS FOR PHASE CHANGE HEAT TRANSFER APPLICATIONS

Husain Al Hashimi, PhD, 2017

Directed By: Professor Jungho Kim, Department of Mechanical Engineering

Better understanding of phase change phenomena can be obtained through local measurements of the heat transfer process, which cannot be attained by traditional thermocouple point measurements. Infrared (IR) technology, which has been used by many researchers in the past, cannot be used under certain circumstances due to spectral transparency issues present in some materials. In the current study, the optical properties of fluorescing materials are proposed as a novel tool for heat transfer measurements. Two fluorescing materials were examined within the framework of the current dissertation: Namely Quantum dots and Ruthenium based temperature sensitive paint, which tend to fluoresce upon excitation by blue or Ultraviolet (UV) light. The light intensity emitted by those fluorescing materials tends to drop with temperature, which can be utilized to obtain the surface temperature distribution at a pixel resolution, for a given monochromic camera. Advantages of the

fluorescing materials include feasibility, applicability to various surface geometries, and the ability to resolve submicron features. The main objective behind the current research work was to develop and assess the optical measurement technique of fluorescing materials, where phase change heat transfer applications, including ethanol drop evaporation and pool boiling, were used to quantify the advantages and limitations of the current temperature measurement technique. Furthermore, a thermofluid study was conducted in order to examine the mechanism of rapid vapor patch formation near critical heat flux (CHF) conditions. Results from the current research work show a correlation between the fluid velocity gradient near the wall and surface heat flux, where both tend to follow similar trend with surface super heat. Thus, it's believed that the incomplete wetting of previous vapor patches near CHF is associated with restricted capillary motion near the surface, where the wetting liquid fails to reach the dry areas with the increased bubble generation activity, due to the local heating caused by the mushroom bubble ebullition.

LOCAL MEASUREMENT AND CHARACTERIZATION VIA FLUORESCING MATERIALS FOR PHASE CHANGE HEAT TRANSFER APPLICATIONS

By

Husain Al Hashimi

Dissertation submitted to the Faculty of the Graduate School of the
University of Maryland, College Park, in partial fulfillment
of the requirements for the degree of
Doctor of Philosophy
2017

Advisory Committee:
Professor Jungho Kim, Chair and Advisor
Professor Bao Yang
Professor Marino diMarzo
Associate Professor Gary A. Pertmer
Associate Professor Kenneth Yu, Dean's Representative

Acknowledgement

In the beginning, I would like to give my special thanks and gratitude to my advisor and mentor: Professor Jungho Kim. I deeply appreciate the research opportunity I have developed from working through his line of work, where the acquired skills and knowledge would go long ways through my future career.

I would also like to dedicate my gratitude to Mr. Majid Aroom for his continuous support through the past 3 years, where he has guided me through the various technical difficulties encountered in my research. The hand-on skills I have gained from working in his machine shop are priceless, and were critical in the design and fabrication of my experimental setup.

I appreciate Dr. Dan Zhang for his help in operating the pool boiling facility, and I would like to thank Dr. Valentin Solotych and Dr. Alex Scammel for providing the necessary feedback on instrumentation usage. I would also like to thank Jason Thompson for the constructive discussions, which aided in the operation and data analysis of the pool boiling experiment. Caleb Hammer software skills came in handy within the operation of the monochromic cameras, which was of great help within the ethanol drop experiment.

I would like to thank Abu Dhabi National Oil Company (ADNOC) for the opportunity of studying abroad and to pursue my Ph.D degree through their fellowship program. ADNOC attaché office at DC provided real-time support and was of great aid in resolving some of the issues pertaining to my scholarship.

I would also like to thank my family back at the UAE for believing in me, and for providing the necessary support throughout my journey of the PhD program. I never felt alone while studying abroad because of them and I made it upon myself to reach the end line, regardless of the obstacles encountered along the way.

Last but not least, I would like to thank my previous colleagues and my friends in the US, with special appreciation dedicated to Jan Muehlbauer, who was of great help in my previous research project. Also, special thanks to my previous roommates: Dr. Abdullah Al Tamimi and Dr. Hesham Ismail. It was a pleasure having you guys around through the past years. Dibesh Shrestha, I will never forget your friendship and your aid during my time of predicament. Thank you!

Table of Contents

List of Figures

List of Tables

Nomenclature

A	Area
C	Proportionality constant
c	Specific heat
CHF	Critical heat flux
CLD	Contact line density
Cov	Covariance
D	Number of times dryout occurs
E	Bang gap energy
f	Focal Length or dryout frequency
Fo	Fourier number
fps	Frames per second
G	Gibbs free energy
g	Gravity
H	Enthalpy
Hi	Hickman number
I	Intensity
IHCP	Inverse heat conduction problem
IR	Infrared
Ja	Jakob number
k	Boltzmann constant or thermal conductivity
L	Thickness
M	Mass
N	Sample size
$\vec{n}$	Unit normal vector
ONB	Onset of nucleate boiling
P	Pressure or vapor patch perimeter
$\vec{P}_r$	Vapor recoil pressure
q”	Heat flux
QD	Quantum dot
r	Radius

T	Temperature or number of times a transition from wet to dry occurs
t	time or dryout duration
TSP	Temperature sensitive paint
u	Heat penetration speed
$\bar{u}$	Mean fluid velocity
$\vec{v}$	Velocity
WF	Wet fraction
x	Spatial resolution

Greek

α	Varshni's Parameter or thermal diffusivity
β	Varshni's Parameter
Δ	Change
η	Mass flux
θ	Contact angle or temperature difference
λ	Wavelenth
ρ	Density or Pearson product-moment correlation coefficient
σ	Surface tension, uncertainty, or standard deviation
ϕ	Plate orientation
δ	Boundary layer thickness

Superscript

‘	Fluctuating component

Subscript

a	Advancing
c	Cavity
D	Helmholtz wavelength
e	Electron
evap	Evaporation

g	bulk
gen	Heat generation
GS	Ground state
h	Hole
i	Initial, reference, index
int	Interface
l	Liquid
M	Nodal distribution
max	Maximum
min	Minimum
N	Nodal distribution
o	Constant or initial
p	Constant pressure
rms	Root mean square
s	Superheat
sat	Saturation or superheat
t	thermal
v	Vapor
w	Wall or subcool
wait	Transient time prior new bubble formation
x	x-coordinate or variable
y	Distance from the wall, y-coordinate, or variable
z	z-coordinate

1. Introduction:

Phase change heat transfer envelopes a variety of fields, starting from the power supply chain associated with the plant cooling, and extending to other applications pertaining to HVAC, cryogenic, and Metallurgy. In addition, phase change heat transfer facilitates a better thermal management within the electronic applications and equipment miniaturization. The efficient thermal removal within a phase change process is associated with its high latent heat, which enables large heat transfer over relatively low temperature gradients [1-4].

Phase change phenomenon involves instantaneous variations of the local heat transfer, which is coupled to the unsteady fluid currents overlying the surface. An example is the sessile drop, which is of interest in several fields including coating, combustion, and cooling facilities. Understanding of these mechanisms requires fine spatial and temporal measurements, which is essential for applications associated with design optimization and safety consideration of a process. Such consideration is crucial within the operations of boilers for instance, where the evolved heat flux is restricted by the boiling crisis. This operational regime is often associated with equipment failure. Within the miniaturized electronics applications such as transistors, high heat fluxes up to 200 W/cm^2 can be liberated from such instruments, where a low wall superheat is desired with respect to the cooling fluid. Thus, operating within the correct boiling regime becomes paramount in the thermal management of the operating equipment [5-8].

Various theoretical and experimental works attempted to model different phase change phenomena under various thermal and physical conditions. In the case

of pool boiling application, the former work fell short in establishing a unified theory for various boiling conditions, where a lot of numerical work formulations on wall-fluid interactions are based on “ad-hoc” hypothesis. For example, various operational conditions within a pool boiling phenomenon entail different modeling approach, which cannot be modeled under a single theory. Such properties are associated with surface conditions and fluid properties, as well as the boiling regime characteristics. In addition, some of the proposed models are not well validated due to the limited resolution of the available data, which might bring about a misinterpretation of the phase change phenomenon under study. Such situations can be encountered with respect to models based on point measurements, which cannot resolve fine spatial resolutions associated with phase change phenomenon [9-10].

The current dissertation proposes the utilization of fluorescing materials optical properties within phase change heat transfer applications, whose temperature dependency can be calibrated practically for fine spatial resolution measurements. In addition, the temperature sensitivity of one of the utilized fluorescing materials is as high as 2% / K, which is a relatively high percentage change in the emitted light intensity. Thus, accurate local temperature measurements with great fidelity can be achieved, which can be competitive to infrared thermography technique. On the other hand, the data acquired from such novel technique can be used to tune various empirical formulations, due to the insight acquired from resolving the fine thermal interaction at the wall boundary. The present study can be considered as one of the first attempts to utilize fluorescing material optical properties for local heat flux measurements, within phase change heat transfer applications.

Research approach involved developing a sensor on a flexible substrate for local temperature measurement purposes. Preliminary attempts involved fabrication of resistive based sensor via photolithography and liftoff technique, where a photoresist was used to pattern the sensor. Technical difficulties in the sensor development, associated with its cost, application approach and its intrusive nature with the flow phenomenon, led to its demise as a potential sensor.

The other technique and the focus of this dissertation associated with the optical properties of fluorescing materials, which was more successful in the sense of its applicability and feasibility within local measurement application. Evaluation of the fluorescing sensor was conducted within two application of phase change heat transfer, where its advantages and limitations were characterized in the light of local measurement and feature extraction capability. Applications of phase change heat transfer include ethanol drop evaporation experiment and pool boiling

Finally the adopted technique was used to examine the mechanism of rapid vapor patch formation near CHF, in conjunction with a CFD study of the fluid turbulence behavior, in the vicinity of the wall. Such study would give further insight into the thermofluid dynamics of surface dryout, which can aid in resolving issues pertaining to equipment failure and improve the performance of cooling equipment.

2. Review of Temperature Measurement Techniques

2.1 Introduction

A review of some of the relevant temperature measurement techniques are provided in the following subsections, which include point measurement techniques and IR thermography. A review of fluorescing materials and their usage within temperature measurement applications are given by the chapter closure.

2.2 Point Measurements

A conventional point measurement technique is the thermocouple, which operates on the basis of Seebeck effect. In principle, two dissimilar metals are connected at a junction, which generates a small voltage with respect to a given temperature. Such technique was used to acquire average heat flux measurement over a surface of interest [10]. In parallel to this technique, Truong [11] considered using a heat fluxmeter, so as to evaluate the heat transfer coefficient associated with a heat sink, via Newton's law of cooling. The drawback of such methods is that its usage is limited to quasi-steady state regime, which cannot be used for complex flow phenomena, due to multi-dimensionality and the instantaneous local changes of the fluid-wall interaction [10-11]. In case of the heat fluxmeter, significant measurement error can incur, in case the thermal properties of the instrument was not well quantified [11].

2.3 Resistive Based Sensors

In the past decades, thermal resistance based sensors has been the focus of wide of variety of applications. These include thermal actuator, flow rate and temperature measuring devices, and sensors pertaining to gas monitoring within food logistics [12-14]. Several studies focused on developing high compact microheater sensors, with competitive spatial resolution performance. Such advances were permitted with development of microfabrication, which enable one to realize fine features as small as a submicron length. Such sensors can play a crucial role in detailed examination of adverse flow condition, as in phase change application for instance, which can be achieved by its instantaneous measurement at multipoint resolution and its conformity to non-planar surfaces [16-19]. Among the various works on resistive sensors, is the one done by Guereca [20] in the field of microelectromechanical systems, which was used in boiling application. The instrument used in Guereca [20] study was fabricated via ion beam milling and photolithography, which had a dual function of providing heat to surrounding fluid and for temperature measurement purposes. The latter used to measure the nucleation temperature, based on sudden changes in the observed temperature, with respect to the temperature coefficient of the instrument resistance [20].

Some of the major challenges with respect to the sensors fabrication regard the dimensional scale difference between the patterned lead connection and the deposited sensor metal, which is one of the main causes for electrical disconnection, due to the sensor's breakage along the leads edges. Such issues is further complicated if an adhesion layer exist between the flexible substrate and the pattern

leads. In addition, it's crucial to include a thermal insulation within the metal sensor design, which can affect its performance criteria, such as measurement sensitivity and resolution [16-17, 21-23]. Also, some studies have indicated deviation of the material properties from bulk metal value for thicknesses close to the mean free path. For instance, Siegel et al [24] observed an inverse relation between resistance and temperature for gold thickness of several nm, as opposed to the proportional correlation between resistance and temperature for bulkier gold thicknesses. Inhomogeneity in the deposited sensor can lead to large temperature gradient on the sensor's surface, which can affect the integrity of the temperature measurement. For instance, Guereca [20] noticed that the acquired temperature measurement was lower for thinner fabricated resistive sensor. Lastly and not least, such temperature measurement requires direct contact with fluid of interest, and it has an element of Joule's heating. Thus, there is some form of intrusion upon the investigated phenomenon, which might induce some form of error.

2.4 Infrared Thermography

A breakthrough in surface temperature measurement has been achieved recently, via infrared (IR) technology, which permitted local heat flux measurements at fine spatial resolution. Such technique proved to be of an essence in proper understanding of heat transfer mechanism, and to further elaborate existing models and correlations. Several studies utilized IR technique in order to resolve the local wall heat transfer in both pool and flow boiling applications. An example is the study conducted by Scammell and Kim [25], where they examined the effect of vortex shedding upon the local wall heat transfer in flow boiling applications. The IR measurements in such

studies are based on black coating of the wall surface, adjacent to the working fluid, which acted as temperature markers for the IR camera. The temperature profile across the wall was deduced numerically, in a coupled radiation-conduction problem from which the local heat flux profile was resolved [25].

Some of the major obstacles associated with IR thermography, pertains to the availability of the IR optical properties, which is required to resolve the temperatures across IR transparent materials, such as silicon and Kapton tape [10, 26-27]. Not to mention that IR transparent materials are not easy to machine, such as in the case of CaF_2 [28]. In addition, in case there is a sharp temperature gradient, there is a restriction on the minimal number of pixels covering an area, so as to resolve the spatial temperature distribution at a region of interest [26-27]. Jason [27] has also raised an issue pertaining to the integration time with respect to the calibration range, where an error in the order of 10 degrees can incur, in case the measurement was done outside the calibration range.

2.5 Other Measuring Technique

Thermographic techniques based on liquid crystals and fluorophores has been suggested as a temperature indicator. One such an attempt is the work done by Kenning [29], where he examined the wall temperature profile within nucleate boiling application, via a thermochromic liquid crystal. However, such techniques can involve tedious calibration procedures and limitations associated with equipment availability and operating costs [30-33]. Not to mention, the narrow temperature operating range by liquid crystal technique [28].

2.6 Fluorescing Materials

2.6.1 Quantum Dots

Quantum dots (QDs) are semiconductors whose length scale is in the order of nanometers and thus subject to 3D confinement. QDs have unique optical properties relative to traditional fluorophores in which it can be excited by a wide range of wavelengths. In addition, it emits light over a narrow spectrum at a longer wavelength. Solid-state lamps in the form of LEDs are usually used for QD excitation purposes. As a direct consequence of the QD length scale, the color of the emitted light can be tuned by changing the QD size via temperature and synthesis time control of the fabrication process. QDs are prepared in a colloidal liquid and it can easily be transferred to surfaces of interest via spray or spin coating. Such versatile fabrication processes can greatly downsize the expenses, pertaining to facility complexity [34-41]. Other QDs delivery methods include electrostatic coating, UV curable solutions, as well as sol-gel approach [41-45]. According to the airy diffraction theory, the minimum spatial resolution that can be detected by a camera (x) is related to the observed wavelength (λ) by Equation 1. In Equation 1, *f* is the distance between the lens and object and d is diameter of the aperture. Thus, QD has a spatial resolution advantage over IR thermography, where local heat flux measurements can be acquired at submicron ranges, due to its smaller wavelength emission [46].

$$\frac{x}{f} = 1.22\,\frac{\lambda}{d} \tag{1}$$

Another characteristic of QDs is the temperature dependency of their optical properties as shown in figure 1, which can be exploited for temperature measurement purposes. This can be related to stoke shift behavior of QDs, which is related to the photoluminescence peak shift, as was observed in previous studies [36, 40, 47-49]. The temperature variation alters the QD optical properties due to thermal expansion of the QD structural lattice [33, 39]. Two trends are evident. The intensity of the emitted light tends to decrease with temperature and the peak in the emitted spectrum tends to shift to longer wavelengths. The changes in the intensity and peak wavelength spectra are not necessarily proportional with temperature. The emitted light intensity changes with temperature tend to be quadratic, which makes it less precise than spectral measurement over large temperature ranges [40, 48].

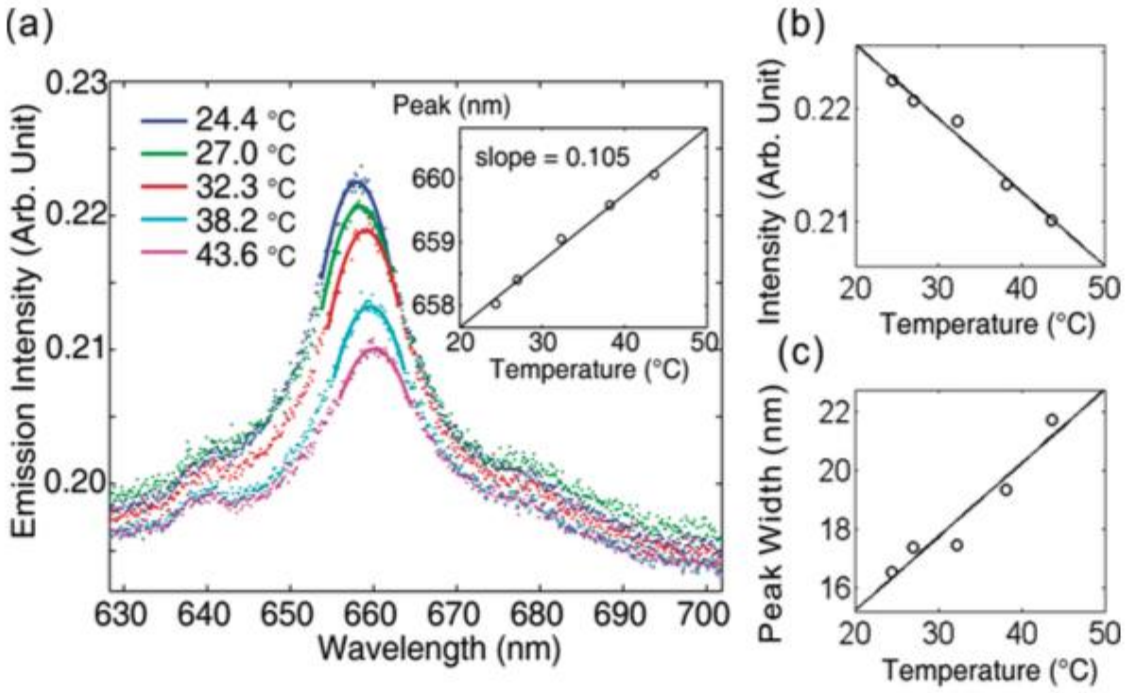

Figure 1: Quantum dot optical property variation with temperature [47]

Several studies have used QDs to measure temperature. Matsuda et al [36] used ZnS-AgInS2 QDs for surface temperature measurement due to their low toxicity and high temperature sensitivity. Jorge et al [36] achieved independency from the excitation source intensity by using multiple QDs with different emission spectra and looking at the intensity ratio. Sakaue et al [37] developed a QD temperature sensor for cryogenic application. Li et al [47] examined the temperature profile of a micro-heater by calibrating the spectral shift of QDs with temperature. They emphasized the importance of QDs particle concentration on a surface so as to achieve a certain temperature precision as a result of particle size variation [47]. The average temperature precision was enhanced at a higher number of QD particles, according to Li et al [47]. Wang et al [42] developed a miniaturized temperature sensor in the form of a reflective fiber for high temperature applications. In a similar line of work to Wang et al [42], Bueno et al [40] developed a photonic planar waveguide temperature sensor using nanocomposites of CdTe and CdSe, which were embedded in PMMA. QDs-PMMA nanocomposites have a peak spectral emission at a shorter wavelength than colloidal solutions of QDs, due to the particles agglomeration and waveguide effects introduced by PMMA matrix. In addition, PMMA tends to be hydrophobic, which minimizes the effect of humidity upon temperature measurement [40].

One of the issues pertaining to QDs can be related to the photobleaching degradation of the emission, which is associated with the breakdown of QDs as a result of continuous light excitation. Other issues pertain to the temperature calibration, which is sensitive to the observed noise in the QD emission readings. Such issues can be remediated by utilizing a high quantum yield of QDs, or

photoluminescence emission, and by utilizing CCD cameras instead of CMOS cameras for higher signal to noise ratio [36-37, 50-51]. Yu et al [48] reported an initial blue shift of the QDs peak spectral emission to shorter wavelengths during the first heating and cooling cycles. Such behavior was resolved by exposing the QDs to several thermal cycles, which resulted in a reproducible spectral peak emission with respect to temperature. Other issues pertain to photooxidation, which can cause an irreversible blue shift due to interaction with surrounding gases [50]. Also, the concentration variation of QDs on a particular area can bring about an uneven intensity distribution, since it's difficult to control the uniformity of QDs over a surface [41, 47].

2.6.2 Quantum Dot Theoretical Background

The thermal quenching is the decrease in QD emitted light intensity with temperature, which is related to the variation in the bandgap energy within QD due to the thermal expansion of QD crystal lattice. The bandgap energy variation of QDs with temperature is given by Equation 2, which is based on the solution to Schrödinger Equation [52].

$$E = \frac{\pi^2 h^2}{2m_e R^2} + \frac{\pi^2 h^2}{2m_h R^2} + E_g \tag{2}$$

Where m_e and m_h in Equation 2 are the effective masses of the electron-hole couple, which is a constituent of an exciton liberating from an excited QD particle. h is the Planck's constant and R is the QD particle radius. The first two terms in Equation 1 represents the nanoscale effect upon the QD bandgap energy, which tends to deviate from the bulk value as was noticed in a study by Franceschetti [53]. This effect

diminishes as the particle radius increases in size. Bulk bandgap (E_g) in Equation 1 is given by Varshni's [54] relation in Equation 3,

$$E_g = E_o - \frac{\propto T^2}{(T+\beta)} \tag{3}$$

where α and β in Equation 2 are Varshni's parameters and E_o is the bulk band gap energy at zero Kelvin. Varshni's relation can be rewritten with respect to an arbitrary reference temperature (T_i) and it is given by Equation 4 [52].

$$E_g = E_i + \propto \left(\frac{T_i^2}{(T_i+\beta)} - \frac{T^2}{(T+\beta)}\right) \tag{4}$$

Figure 2 shows a plot of the calculated QD bandgap values as a function of temperature, which is computed using Equation 3 for both CdSe/Zns and InP QDs. The band gap variation with temperature is governed by the chosen material intrinsic properties, which can bring about different temperature dependence as shown in Figure 2 **[52, 55]**.

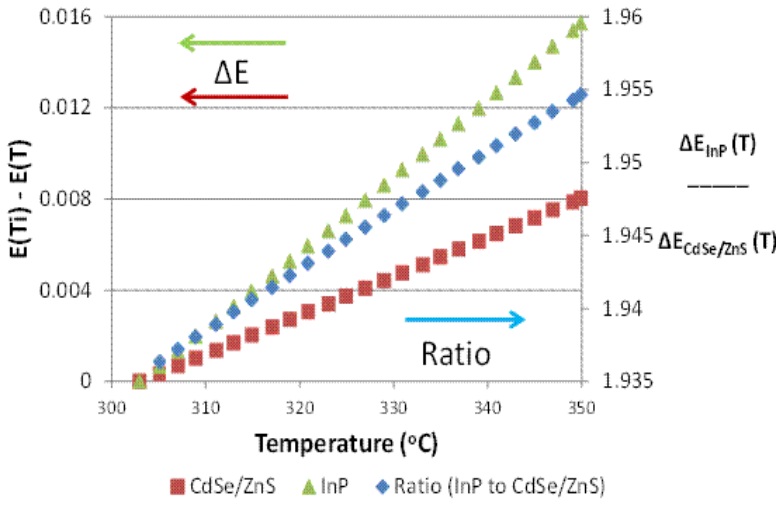

Figure 2: Estimate of QD Bandgap energy variation with temperature

From the empirical fittings to various photoluminescence intensity data in the literature, it was noticed that the quantum dots have an exponential decay behavior with temperature and it can be approximated by Equation 5 [56-57].

$$I \approx Ce^{\frac{E_{GS}^{QD}}{kT}} \tag{5}$$

k in Equation 1 is Boltzmann constant, while C is the proportionality constant representing the lifetime of the radiative and non-radiative processes, as well as the exciton capture and escape rates [57]. E_{Gs}^{QD} is the ground state band gap energy within quantum dots, which can be taken from Varshni's relation in Equation 2. Equation 2 can be combined with Equation 4, where a relation between the relative emitted intensity and temperature is acquired and it's given by Equation 6.

$$\frac{I(T)}{I(T_{ref})} \approx e^{\frac{\frac{\propto T_i^2}{(T_i+\beta)}}{kT_i} - \frac{\propto T^2}{\frac{(T+\beta)}{kT}}} \tag{6}$$

Table 1 gives the Varshni parameters used in the empirical calculation of the relative intensity, while Figure 3 plots the calculated results for CdTe and CdSe/ZnS QDs. As shown in Figure 3, one can approximate the temperature dependency of the emitted light intensity to be of a linear nature over small temperature ranges. Such result was experimentally observed by Maruyama et al. [51].

Table 1: Varshni's parameters

QD Material	**α(J/K)**	**β(K)**
CdSe/ZnS [58]	6.09E-23	150
CdTe [59]	8.57E-23	160

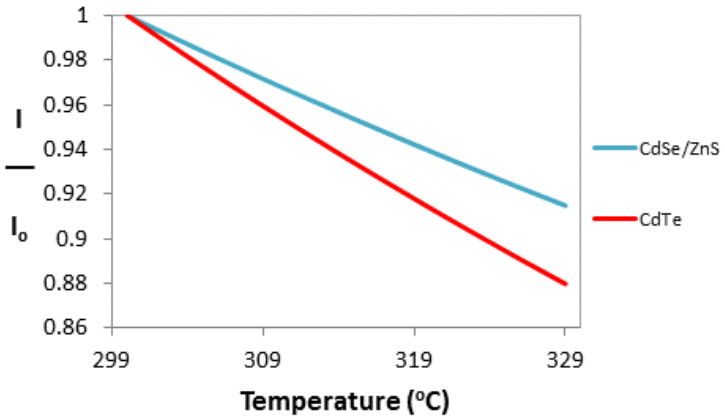

Figure 3: Relative intensity versus temperature

2.6.3 Temperature Sensitive Paint

Another fluorescing material that works under the same principle as the quantum dots is the temperature sensitive paint (TSP), which comprises of a light emitting luminophores and a binder. As shown in Figure 4, the luminophores gets excited to a higher energy state upon absorption of photons from a short wavelength light source. Afterwards, the excited luminophores undergoes a decay to a lower energy state, where it emits light at a longer wavelength. This process is called photoluminescence. Two conversion processes compete with the photoluminescence of the TSP, which causes the luminophores to decay closer to its ground state: first, the external conversion of the luminophores energy, which is associated with its emitted light quenching via molecular interaction. Such process is relevant within pressure sensitive paint applications, where various oxygen concentrations are associated with different light emission intensity from the luminophores. The second type of the luminophores conversion processes is the internal conversion, which is associated with the energy state variation of luminophore with temperature. Such process is called thermal quenching [28].

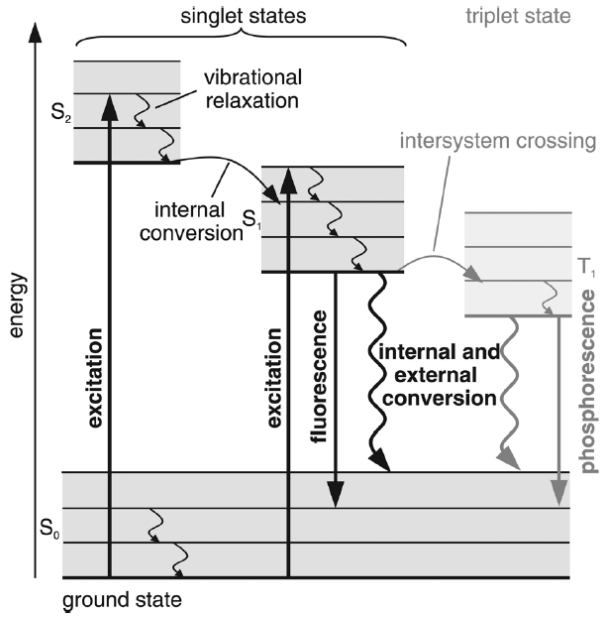

Figure 4: Jablonsky energy-level diagram [28]

The material selection for the luminophores and the binder governs the optical characteristics of the yielded TSP. For instance, the temperature dependency of the luminophore's light emission varies from one material to another. In addition, the operation of the paint as a temperature sensitive or pressure sensitive paint depends on the binder permeability to oxygen [60].

Recent interest in TSP has emerged in several applications, as a local temperature measurement mean. One of those attempts is the work by Shibuya et al, pertaining to surface wall temperature within heat sink application. In Shibuya et al [61] study, local temperature variation was captured in form of TSP intensity changes, as a consequence of a passing bubble. Several studies utilized TSP optical properties for surface temperature measurement within wind tunnel facilities some of which were involved in hypersonic flow conditions. Among the various wind tunnel experiments are the work by Kurits [62], Bhandari [63], Lee et al [60], Schramm et al [64], Huang [65], Yang et al [66], and Ozawa et al [67], where the local temperature

distributions were deduced from surface of interest, based on the observed TSP emission. Long [68] utilized multiple luminophores one of which is temperature insensitive, so as to account for the intensity variation within the excitation light source. Other work by Huang et al [69] examined the temperature profile within a microchannel flow application, via the optical properties of the TSP.

The luminophores suffer from similar shortcomings as the quantum dots. For instance, paint thickness inhomogeneities over the surface as well as non-uniform excitation light illumination are among several factors attributed to the observed noise within optical measurements. Background noise and particulates can also interfere with the optical properties of the TSP, which can bring about a shift in the observed intensities. Photobleaching effect tends to be more severe in the case of TSP [70].

3. Review of Phase Change Phenomena

3.1 Introduction

The following subsections provide relevant background on ethanol drop vaporization, as well as on pool boiling phenomena. A review of the various works within the corresponding fields is also provided below.

3.2 Ethanol Sessile Drop

The vaporization of an ethanol sessile drop involves hydrothermal waves or convective cells driven by temperature gradient within the drop. Such phenomenon tends to have a strong coupling between the substrate conduction and fluid convection, along with the vapor diffusion around the droplet. As a result, a sessile drop requires both fine spatial and temporal measurements in order to capture the relevant mechanisms underlying this phenomenon. Several studies have been conducted on ethanol sessile drop. An example is the study made by Sefiane et al [71] examining the instabilities within a sessile drop for different fluids. It was observed that the temperature gradient varied along the drop, which was associated with the evaporation process. As a consequence of the temperature gradient, a wave like pattern was observed from the IR images, which varied from cool to warmer regions along the drop radial direction. Such waves, known as convective cells, can vary in size with respect to the evaporation time and the radial distance from the center. In general, the number of convective cells is affected by the surface thermal properties, where fewer cells tend to prevail as the evaporation proceeds. In another study by Garnier et al [72], hydrothermal waves was observed within ethanol, which was

characterized with uniform temperature gradient, driven by temperature boundary along the edge of ethanol. On the contrary, the convective cells within Sefiane et al's [71] study were allocated to random generated temperature gradient, due to non-uniform evaporation along the ethanol droplet. Sobac and David [5], Brutin et al [73], and Brutin et al [74] described the evaporation process of the ethanol drop to take place in several phases: Upon droplet placement on the substrate, the fluid starts to warm up, where fluid heat capacity is the dominant factor within this stage. The fluid would continue to heat up until a steady maximum evaporative heat flux is reached. The second phase is characterized by the appearance of convective cells after which the evaporative heat flux starts to decline. The declination in the observed heat flux marks a transitional phase, which exhibits a decrease in the number of convective cells. Finally, the ethanol droplet would vaporize in the form of a thin film, which is dominated by conductive heat transfer mechanism. In the Brutin et al [74] study on ethanol droplet, a link was establish between the surface superheat, and the non-uniform temperature gradient evolving within a droplet, where thermocapillary effect has been concluded to be the dominant driving force behind the convective cells. In principle, buoyancy effect tends to be negligible within a droplet, if the capillary length is smaller than the critical diameter by 2 folds. Such conditions can exist within a relatively small droplet, where the Marangoni number is much larger than Rayleigh number. In other words, surface tension effect is more pronounced relative to fluid buoyance [73-74]. As a consequence of the existence of a temperature gradient, arising from the spontaneous evaporation process, the variation in the surface tension with temperature induces a recirculation region in form of

vortices, known as Marangoni effect, which can be asymmetric in nature. Such vortices or convective cells are influenced by the thermal properties and the viscosity of the fluid, as elucidated by a simulation study by Karapetsas et al [75]. Two common modes of evaporation are known within literature: Constant diameter and constant contact angle. For the latter mode, a smaller contact angle is associated with thin films, which can bring about an increased surface wettability. Thus, the evaporation process would proceed at a higher rate. As for constant droplet diameter mode, the importance of the evaporative heat flux increases with temperature [5, 74]. Both Sobac and Brutin [5] and Brutin et al [74] have correlated the evaporation heat flux as well as the number of convective cells to the evaporation time, via a scaling law, which tends to be "lineic" in nature. Karapetsas et al [75] have elaborated on the role of a higher evaporative rate upon stabilizing the droplet convective cells, by establishing a more uniform temperature distribution.

3.3 Pool Boiling

3.3.1 Pool Boiling Characteristic

Pool boiling is a phase change phenomenon associated with a submerged heater surface within a fluid. From the heat transfer prospect, Nukiyama [76] identified several boiling regimes from his experiment, which involves a thin wire within a pool of water. As shown in Figure 5, the hydrodynamic structure of a heated fluid undergoes several developments for various supplied heat fluxes. At low heat fluxes, a single phase natural convection is the dominant heat transfer mechanism, which continues to persist with the initial increase in the wall heat flux, causing an

overshoot in the wall superheat beyond the natural convection regime. Further increase in the wall heat causes a sudden drop in the wall superheat, where individual bubbles are generated from active nucleation sites. This Phenomenon marks the onset of nucleate of boiling regime (ONB), also known as partially developed nucleate boiling regime. With further increase in the input heat flux, more nucleation sites become active and the bubble generation frequency increases, which is associated with bubble coalescence and the hydrodynamic development of vapor slug and columns. This regime is known as fully developed nucleate boiling. At the peak heat of the nucleate boiling regime, also known as the critical heat flux (CHF), is a point beyond which the heat removal by the boiling fluid starts to decrease, which can trigger a sudden increase in the wall superheat towards the film boiling regime. Such behavior is related to the vapor patch formation on the heater surface, which is often associated with heater burnout towards film boiling regime, due to the low thermal properties of the vapor phase. If the wall superheat can be controlled independently from the wall heat flux, another regime existing between the nucleating boiling and the film boiling regimes can be examined, known as transition boiling. The Transition boiling regime is associated with partial formation of vapor patches on the heater surface. Another characteristic point is achieved within the transition boiling regime, which is a heat flux minima at which liquid droplets hover over vapor patches, known as Leidenfrost effect. Two notable hystereses are observed along the transition boiling regime: As mentioned before, the boiling curve passes through CHF point and jump into the film boiling for a wall heat control system. On the other hand, the boiling curve passes through the minimum heat flux and jumps to the nucleate boiling

regime, as the wall superheat is reduced from the film boiling regime. Such phenomenon is associated to the agglomeration of the vapor patches, which causes sudden changes in the wall superheat. The second hysteresis within the transition boiling regime is related to a higher heat flux value, due to an increase in the wall superheat beyond CHF toward minimum heat flux. Such behavior is related to the difference in receding angle and advancing angle. Thus, a lower heat flux is observed while moving towards CHF from Leidenfrost point, than the other direction in the boiling curve, as shown in Figure 6 [76, 77].

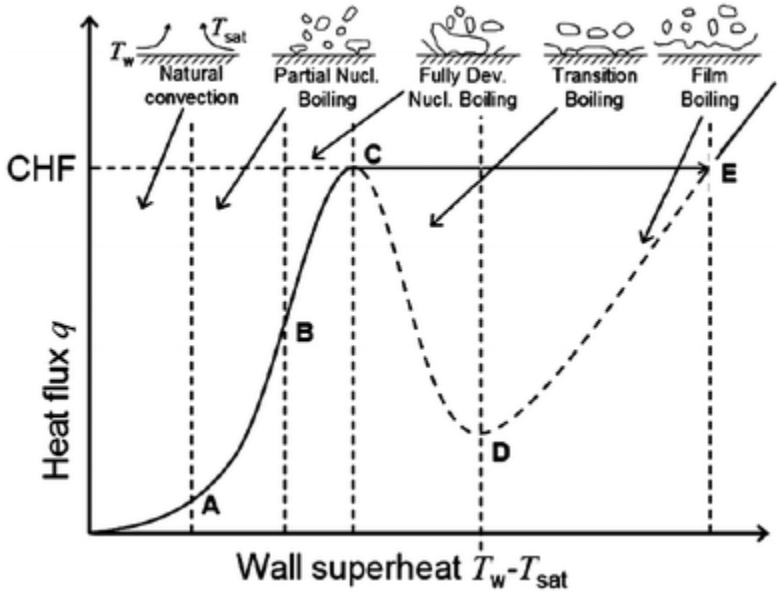

Figure 5: Pool boiling curve and hydrodynamic development [78]

3.3.2 Bubble cycle

The nucleation taking place during the boiling process is usually a heterogeneous type, which has low energy requirement for spontaneous bubble generation, due to the presence of residual gases and surface cavities. The minimum energy required for the bubble generation from a nucleation site can be related to the free energy of

bubble formation (G_v), as well as the surface tension (σ) at the interface, as given by Equation 7 [79].

$$\Delta G = \frac{4}{3}\pi r^3 G_v + 4\pi r^2 \sigma \tag{7}$$

Bubble formation from a particular nucleation site is favorable for a negative gibbs energy. The first nucleation sites to generate bubbles at ONB are the ones at which the bubbles form a higher apparent contact angle within the nucleation site cavity. As the wall superheat increase, more sites become active, as the free energy threshold has been fulfilled. The ebullition cycle of a bubble consists of several phases, which includes the growth period, departure period, and waiting period. The growth period consists of different stages, which are characterized by different driving mechanisms, as shown in Figure 6. The first stage of a bubble growth is inertia controlled, where a bubble grows from a small air embryo within the cavity of a nucleation site. At this stage, the pressure within the growing bubble is larger than the surrounding, which promotes a rapid growth due to the relatively lower surface tension effect. The Rayleigh Equation, given by Equation 8, describes the rate of bubble growth during the initial stage, which is associated by the work done on the surrounding fluid as the bubble expands under the influence of higher vapor pressure [79].

$$r(\mathrm{t}) = \left\{\frac{2}{3}\left[\frac{\mathrm{T}_\infty - \mathrm{T}_{\mathrm{sat}}(\mathrm{P}_\infty)}{\mathrm{T}_{\mathrm{sat}}(\mathrm{P}_\infty)}\right]\frac{\mathrm{H}_{\mathrm{lv}}}{\rho_{\mathrm{l}}}\right\}^{1/2}\mathrm{t} \tag{8}$$

The final stage of bubble growth is thermally controlled, which proceeds at a lower rate relative to the initial growth rate. Such attribute is related to the lower

pressure difference across the vapor-liquid interface with bubble expansion. For a large Jacob number, associated with a higher surrounding temperature change relative to the slow vapor growth rate, the final stage of bubble growth can be approximated by Equation 9, which is derived from the energy balance at the bubble interface [79]. Ja in Equation 9 is the Jakob number and α_l is the thermal diffusivity of liquid.

$$r(t) = 2\sqrt{\frac{3}{\pi}}Ja\sqrt{\alpha_l t} \tag{9}$$

The growth mechanism within the second growth stage can be considered as a combination between the inertia controlled and thermally controlled growth rate, as the bubble emerge from surface of the nucleation site. Once the critical bubble diameter has been reached, the bubble slide along the wall and departs from the surface equivalent to "lift-off diameter", which ensues a new bubble growth cycle with fresh liquid supply rewetting the surface [7]. In effect, the fresh liquid supply undergoes transient heating until the thermal layer reestablished. This time period is referred to as the waiting time period and it's given by Equation 10, which based on the equilibrium superheat and cavity radius. The range of active cavity sizes at a given superheat can be estimated from Hsu [80] semi-empirical model, given by Equation 11. A plot of the active sizes with the wall superheat is also given in Figure 6, which is based on saturated HFE7000 properties at 1 atm for an assumed thermal boundary layer of 0.2 mm. The insert in the cavity-superheat plot is a magnified surface topology for a NiCr heater, which was used in the pool boiling experiment within the current study. The average cavity diameter is around 4 μm.

$$t_{wait} = \frac{9}{4\pi\alpha_l}\sqrt{\frac{(T_w - T_\infty)r_c}{T_w - T_{sat}\left(1 - \frac{2\sigma}{r_c\rho_v H_{lv}}\right)}} \tag{10}$$

$$\begin{Bmatrix} r_{c,min} \\ r_{c,max} \end{Bmatrix} = \frac{\delta_t}{4}\left[1 - \frac{\theta_{sat}}{\theta_w}\begin{Bmatrix} + \\ - \end{Bmatrix}\sqrt{\left(1 - \frac{\theta_{sat}}{\theta_w}\right)^2 - \frac{12.8\sigma T_{sat}(P_l)}{\rho_v H_{lv}\delta_t\theta_w}}\right] \tag{11}$$

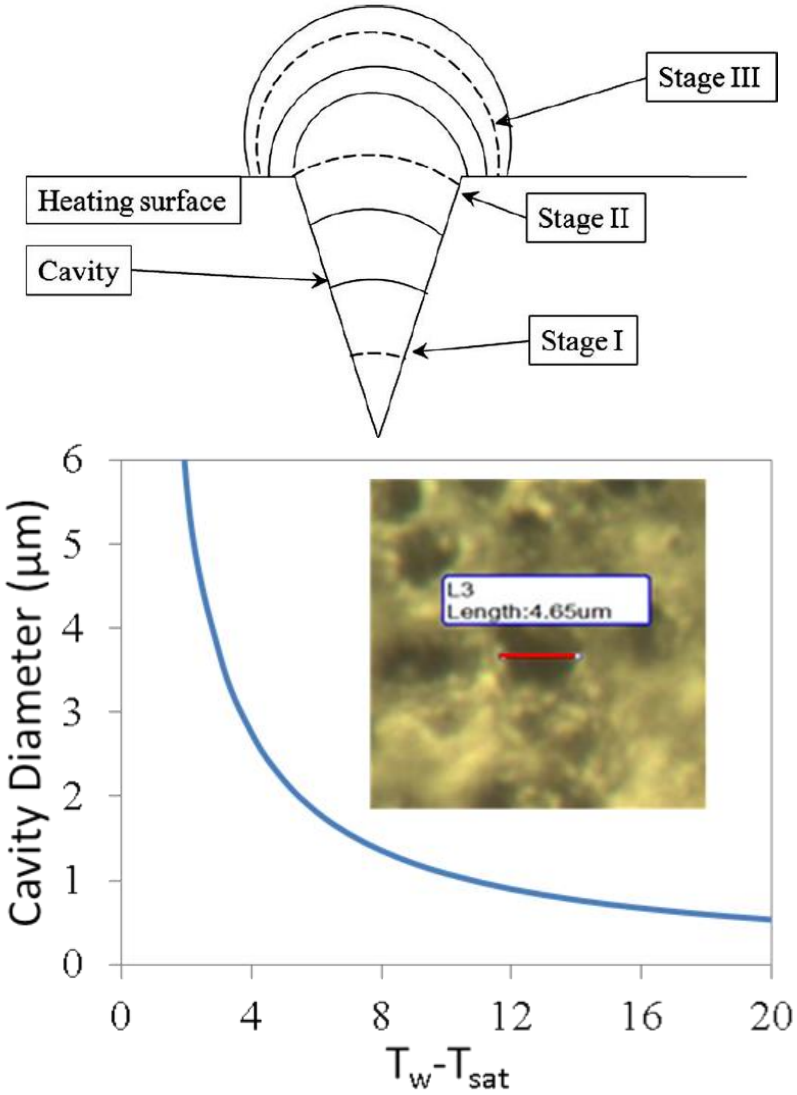

Figure 6: Surface characteristics; Top: stages of bubble growth [79], Bottom: Relation of active cavities with ONB superheat, typical diameter size within NiCr heater is shown as an insert within the cavity-superheat plot.

3.3.3 Parametric Effects:

Various factors affect the hydrodynamic structure of the boiling phenomena, as well as the thermal interaction at the surface microstructure. For instance, the nucleation site density on a particular heater surface is dependent on its roughness, which in turn influences the hydrodynamic evolution of pool boiling. As mentioned earlier, individual bubbles coalesce into more elaborate slug and column structures with the increase in nucleation site density and with the bubble generation frequency. Such influence reaches its pinnacles near CHF, where vapor patches starts to swipe over the surface. In general, the nucleation site density has an inverse relation with respect to the surface cavity sizes; thus, one can expect that a higher nucleation site density exists on a rougher surface. On the other hand, the generated bubbles impede surface rewetting, so the nucleation site density has an indirect influence upon the surface liquid supply reflux. In addition, the ebullition cycle time period can vary from one surface condition to another. The influence of surface roughness is also dependent on the relative properties between the heater surface and the working fluid. Therefore, the nucleation site density can vary from one working fluid to another. In a study by Kotthof et al [81], the effect of surface condition, pertaining to various macrocavity structures, was examined in the study, where a larger macrocavity was observed to be more active. In addition, the macrocavitiy tends to reduce the activity of neighboring sites by reducing the overall superheat of the area. On the other hand, a lower nucleation site density and superheat was observed for a higher microroughness [6, 81-83].

Spatial confinement and orientation can affect the thermo hydrodynamic behavior of a boiling fluid. Howard and Mudawar [84] observed a similar behavior to flow boiling, for a vertically oriented surface heater. Flow separation is common for such orientation, which might be attributed to interphase instability. Further increase in the heater orientation was associated with lower heat flux and early dryout, which can be related to stagnation of the generated bubbles that impedes surface wetting as indicated from Howard and Mudawar [84]. A similar conclusion was drawn from Pioro et al study [85], where the effect of plate heater orientation diminishes near CHF due to higher bubble coalescence. On the other hand, spatial confinement of the plate heater was associated with delays in the bubble departure, which reduced the observed heat flux, as was observed in a study by Zhao et al [86].

The surface tension and the contact angle have a profound influence on bubble cycle and on the overall behavior of a boiling fluid. For instance, in a numerical study by Pezo and Stevanovic [8] the surface wettability by a working fluid affected the nucleation site density, which in turn dependent on the contact angle of the working fluid. Recent CHF models suggested a dryout mechanism based on vapor recoil model. Such model was adopted by Kandlikar [87], where attributes pertaining to the receding angle of the working fluid was incorporated within the CHF model. According to Kandlikar [87], heater surface dryout is associated with an increase in the contact angle, which promotes vapor spreading on the surface.

The influence of various materials thermophysical properties is evident within heater surface-fluid interactions. For instance, the thermal conductivity of the substrate affects the wall superheat, as well as the observed evaporation. In a study by

Stephan and Abdelsalam [88], involving Cryogenic fluids, a high surface wettability was observed in the case the working fluid shared similar thermal properties to the wall heater. In a pool boiling study by Benjamin and Balakrishnan [82], the impact of surface finish and different thermophysical properties, associated with different working fluid and wall material, was examined with respect to the observed nucleation site density. From the work of Benjamin and Balakrishnan [82], the role of the fluid-wall thermal properties upon the nucleation site manifested in the surface-liquid interaction factor within a boiling phenomenon, where a higher nucleation site density was observed upon copper surface relative to aluminum. Other parameters include pressure, which was scrutinized by Sakashita [89] in a pool boiling study, involving CHF enhancement via nanofluids application in water. In Sakashita [89] study, a higher CHF was observed with pressure, which was associated with smaller bubble formation and growth rate at the nucleation sites.

From the previous discussion, one can realize that the various parameters are not independent, but rather have a stochastic influence upon pool boiling. As consequence, it's difficult to examine the various parameters without considering the other factors within a study, which makes modeling approach a rather daunting task.

3.3.4 Burnout Phenomenon

Peak heat flux, associated with a rapid transition from nucleate boiling to film boiling, is attributed to local surface conditions and to the surface-microfluid interaction. Such conditions ensues in a boiling crisis associated with a rapid temperature spikes, which usually results in the heater failure due to the low thermal conductivity of the overlying vapor patches [87, 90-91]. Such phenomenon is related

to several interrelated events occurring at different hydrodynamic lengthscales, as shown in Figure 7, where it can vary from cm at the surrounding liquid, down to nm at the wall. Close to the wall, distinct liquid regimes can be readily identified from Figure 8, associated with the different hydrodynamic length scales occurring within the boiling phenomenon. The macrolayer is associated with the local turbulent two phase hydrodynamics, occurring at the surrounding area to the evolving bubble from the nucleation sites. On the other hand, the microlayer exists underneath a growing bubble within the macrolayer, where a dryspot within the thermal patterns indicates the existence of a bubble on top of a microlayer. The microlayer is affected by several factors that include the surrounding parametric effects, such as pressure, as well as the thermal and wetting properties of the wall at submicron length scale. The interphase within the microregion, and hence its thermal resistance, is not constant, relative to the well-defined bubble curvature within the macrolayer. Such factors dictate the microlayer thickness and it's dryout behavior for the duration of the bubble cycle, where the microlayer can be linked to the lifetime of a bubble [2, 92-94]. With the increase in heat flux, the dryspots merge together, which can bring about a rapid spreading of the vapor patch over the wall surface. This behavior is associated with an irreversible dryout over a large area of the heater surface near CHF, known as thermal runaway, which impedes surface rewetting and often associated with a heater burnout [9].

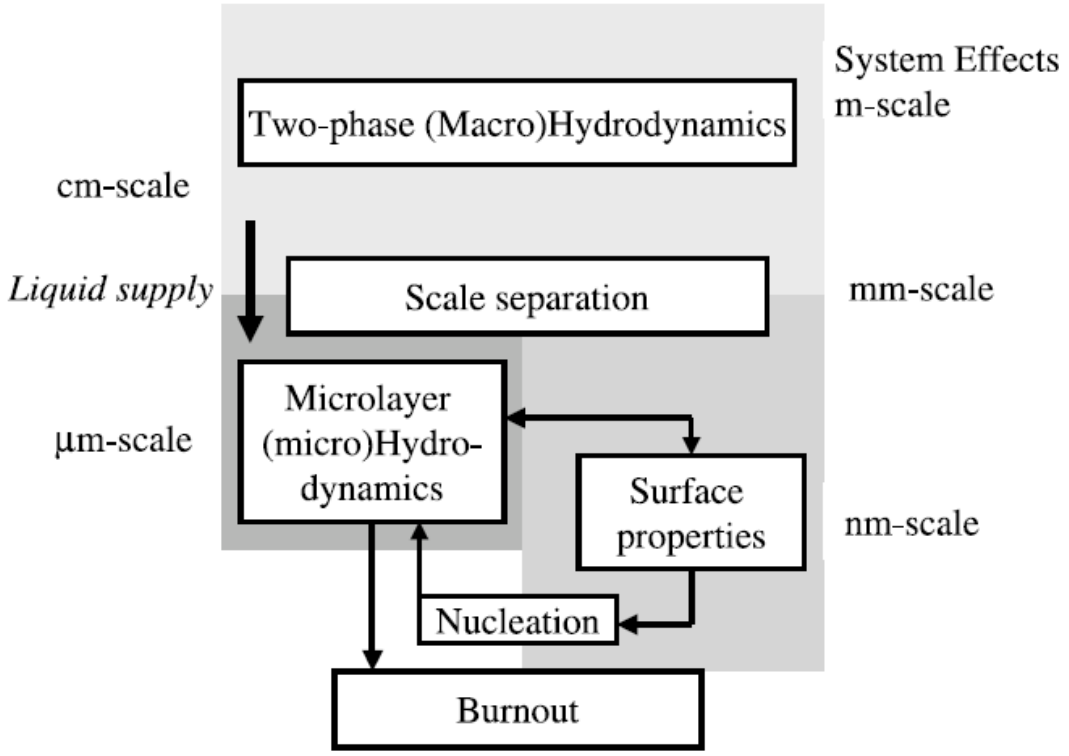

Figure 7: Scale separation [9]

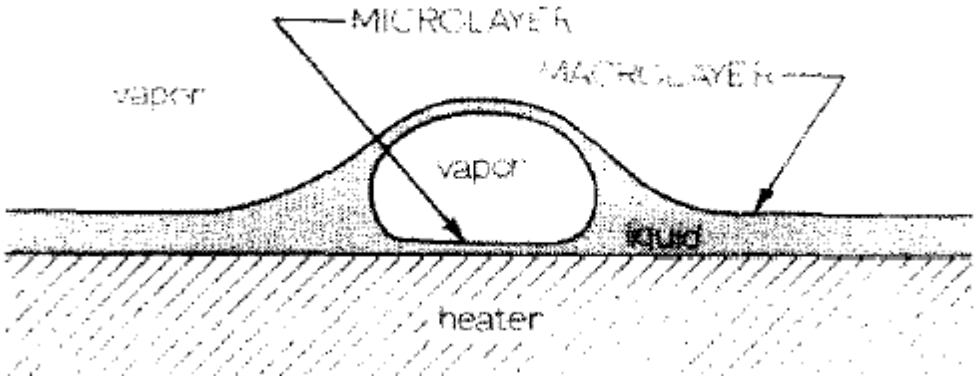

Figure 8: Illustration of the microlayer and macrolayer [92]

Previous models vary in their description of the hydrodynamic development and fluid-wall interaction near CHF condition. For instance, Zuber's [95] hydrodynamic model, later refined by Lienhard and Dhir [96], related the CHF conditions to the instability within the vapor column feeding into vapor mushroom, and it's given by Helmholtz wavelength criteria as shown in Equation 12 [95].

$$\lambda_D = 2\pi \left[\frac{3\sigma}{(\rho_l - \rho_v)g}\right]^{1/2} \quad (12)$$

This criterion, known as the most dangerous wavelength, defines the minimum distance between the rising jets of vapor, corresponding to Taylor instability at the vapor-liquid interphase. Kutateladze [97-98] associated CHF to the destruction of a chaotic two phase system above the surface, which contradicts the ordered columns of vapor jets described by Zuber [95]. The CHF given by the hydrodynamic model for flat plat is shown in Equation 13 [95-96].

$$q''_{CHF} = 0.149 H_{lv} \rho_v \left[\frac{\sigma g(\rho_l - \rho_v)}{\rho_v^2}\right]^{1/4} \quad (13)$$

In the macrolayer model of Haramura and Katto [99], the CHF was related to liquid supply limitation and eventual dryout of the macrolayer with the hovering vapor mass. Zhao et al [100] associated CHF with the dryout of the microlayer existing under the bubble, due to the increase in the surface heat flux. Another CHF model associated with the surface dryout to a momentum imbalance at the contact line of the bubble, due to the rapid evaporation along that region at high heat fluxes. As a result, a vapor recoil force causes the dryspots under the influence of an increased apparent angle of the wetting fluid to spread over the surface, which undercuts the liquid front from wetting the surface [93, 101-102]. The vapor recoil force acting on the liquid vapor interface can be computed as follows: From the conservation of momentum and mass at the interface:

$$\Delta m(\vec{v}_v + \vec{v}_{int}) + \overrightarrow{P_r} \Delta t A = 0 \quad (14)$$

Where $\vec{v}_{int} = \frac{-\rho_v}{\rho_l}\vec{v}_v$, $\Delta m = \Delta V \rho_v$ and $\vec{v}_v = \vec{n}\frac{\Delta V}{A\Delta t}$. Substituting the relevant variables, Equation 14 can be written as,

$$\overrightarrow{P_r} = -\eta^2(\rho_v^{-1} - \rho_L^{-1})\vec{n}, \text{ where } \eta = \frac{\Delta m}{A\Delta t} \quad (15)$$

The vapor recoil is related to the local heat flux by the latent heat of the working fluid, as shown in Equation 16.

$$q"_L = H_{lv}\eta \quad (16)$$

A non-dimensional number defining the relative stability of the interface with respect to the recoil force is the Hickman number (Hi), given by Equation 17 [90]. Thus, a higher Hickman number implies a more stable interphase system [91].

$$Hi = \frac{r_0 q"^{-2}}{\sigma {H_{lv}}^2}(\rho_V^{-1} - \rho_L^{-1}) \quad (17)$$

Kandlikar [87] suggested Equation 18 for CHF, which incorporates the wetting angle parameter.

$$q"_{CHF} = H_{lv}\rho_v^{1/2}\left(\frac{1+cos\theta}{16}\right)\left[\frac{2}{\pi} + \frac{\pi}{4}(1+cos\theta)cos\phi\right]^{1/2}[\sigma g(\rho_l - \rho_v)]^{1/4} (18)$$

The hydrodynamic model omits information pertaining to fluid-wall interaction, which can result in large margins of error within the computed CHF values. Such an uncertainty arises within microgravity applications and non-wetting surfaces, where contact angle parameter becomes a dominant factor. On the other hand, the microlayer dryout is not well defined, which can bring about a large uncertainty within the computed CHF, due to its small lengthscale and inaccessibility to the heater surface [87, 90, 103].

Several studies suggested that the subsystems within the pool boiling phenomenon operate independently, where the observed patterns indicate different trends between the ordered surface thermal patterns and the turbulent hydrodynamic development within the fluid at different surface heat fluxes. Thus, surface phenomenon associated with CHF can be examined autonomously, where mechanisms associated with surface dryout can be revealed based on the surface thermal patterns. In addition, visual limitations to the wall surface, associated with violent boiling phenomenon, can be compensated by wall-fluid thermal interactions [102-103]. Thus, CHF models and correlations can be enhanced if more reliable heat flux data are available, which would serve as a benchmark data for Pool boiling applications.

3.4 Turbulence

Flow turbulence arises from local disturbances, which is associated with eddy currents within the flow. Such aspect is of importance within pool boiling application; especially, near the wall surface where active nucleation sites bring about local turbulence within the thermal boundary layer and the neighboring film of fluid. The velocity magnitude ($\overline{u}$), also known as Reynolds averged, is given by Equations 19.

$$\overline{u} \equiv \sqrt{\left(\overline{u}_x^2 + \overline{u}_y^2 + \overline{u}_z^2\right)} \tag{19}$$

Each vector of the velocity components comprises of the time averaged speed component and the turbulent fluctuation component, as shown in equations 20-22. Thus, by deducting the time averaged velocity component from the various instantanous velocity components, the various turbulent velocity components can be

computed. The Turbulence intensity (u_{rms}) is given by Equation 23, which is the root-mean-square of the turbulent velocity fluctuations.

$$u_x = \overline{u}_x + u'_x \tag{20}$$

$$u_y = \overline{u}_y + u'_y \tag{21}$$

$$u_z = \overline{u}_z + u'_z \tag{22}$$

$$u_{rms} \equiv \sqrt{\frac{1}{N}\sum_{i=1}^{N}(u_x - \overline{u}_x)^2 + \frac{1}{N}\sum_{i=1}^{N}\left(u_y - \overline{u}_y\right)^2 + \frac{1}{N}\sum_{i=1}^{N}(u_z - \overline{u}_z)^2} \tag{23}$$

Several studies examined the impact of the working fluid local turbulence. Such studies include the work by Xu and Chen [104], Končar et al [105-106], and Kim et al [107]. In their work, velocity fields were generated from PIV measurement and CFD simulation, under various wall heat fluxes and flow conditions. In an experimental and numerical study by Končar et al [105-106], the turbulent kinetic energy of a flow within a rectangular channel was observed to increase with the surface heat flux. The effect of nucleate boiling upon the flow manifested as an additional viscous effect, which brought about an enhancement in the evaluated turbulent kinetic energy. Such effect was brought about by the local turbulence induced by the ebullating bubbles. Using local isotropy assumption, the turbulent kinetic energy dissipation can be evaluated using Equation.

$$\epsilon = \langle 4\left(\frac{\partial u'_x}{\partial x}\right)^2 + 4\left(\frac{\partial u'_z}{\partial z}\right)^2 + 3\left(\frac{\partial u'_x}{\partial z}\right)^2 + 3\left(\frac{\partial u'_z}{\partial x}\right)^2 + 4\left(\frac{\partial u'_x}{\partial x}\frac{\partial u'_z}{\partial z}\right) + 6\left(\frac{\partial u'_x}{\partial z}\frac{\partial u'_z}{\partial x}\right)\rangle \tag{24}$$

In another study by Kim et al [107], the effect of natural convection upon thermally stratified layers of water was examined as the temperature of a water pool was increased, along with the subsequent boiling effect near saturation temperature conditions. The thermal stratifications were impenetrable by the local vortices arising

by the asymmetrical heating from a horizontal rod, due to the induced countercurrents within the stratified layers underneath the heater. Once saturation conditions has been reached, the thermal stratifications are distorted by the local turbulence induced by the ebullating bubbles from the active nucleation site, which paves the way for the bulk fluid vortices into the previously inaccessible stratified layers.

4. Ethanol Droplet Experiment

4.1 Introduction

In the ethanol droplet experiment, QDs are used to examine the local temperature distribution, where the local heat flux associated with the evaporation of an ethanol droplet was determined in the current study. Such study acts as a qualifier test for the practicality of fluorescing materials for local heat flux measurement within phase change heater transfer applications.

4.2 Experimental Section

4.2.1 QD Film Fabrication

The QD-gelatin film was fabricated from water based CdSe/ZnS QD solution (QSA from Ocean NanoTech) with a peak spectral emission at 620 nm. The film was prepared by mixing 40 µl of the QD solution with 40 µl of a preheated gelatin-water solution, where the gelatin-water solution had a concentration of 0.015 grams of gelatin powder (Knox original gelatin) per 1 ml of distilled water. The QD-gelatin solution was placed and spread on a temporary transfer surface, where the transfer surface was precoated with a hydrophil^{TM} S for enhanced surface wetting. The transfer surface was placed in the fridge for several hours, where the QD-gelatin solution gelled initially followed by the water evaporation from the gel. A thin layer of QD-gelatin film formed upon water evaporation which was measured to be around 6 µm thick as shown in Figure 10. Such deposition technique resolved some of the issues associated with evaporation contact line, which brought about a non-uniform distribution of QDs as shown in Figure 9.

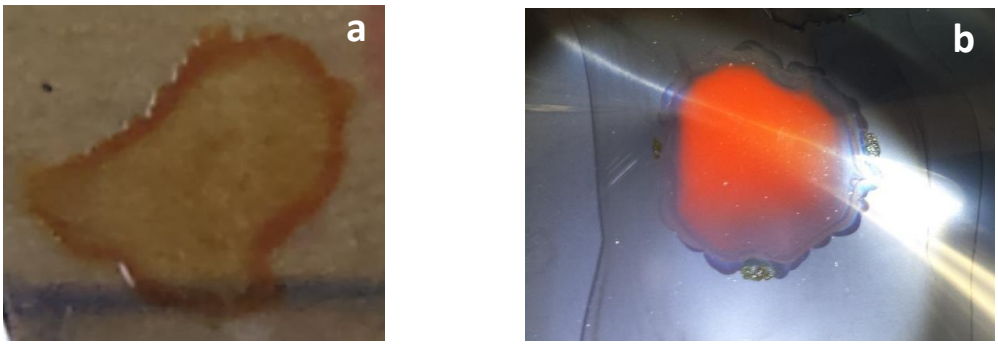

Figure 9: QD deposition, (a) QD evaporative deposition; (b) QD-Gelatin film

4.2.2 Test Setup

Figure 10 shows the Test setup used for the ethanol droplet vaporization test, where the properties of ethanol are given by Table 2. The spectral properties of QD are also given in figure 10. The QD-gelatin film was transferred from the temporary surface to a transparent acrylic plastic surface with a dimension of 4.3 cm by 5 cm by 1 cm, where a transparent epoxy (AeroMarine) was used to attach the two layers together. A polyimide-carbon film heater (100RS1000 film from DuPontTM) was attached on top of the QD-gelatin film using the same transparent epoxy. The Transparent epoxy was degassed prior application so as to minimize the dissolved gases within the epoxy. The film heater provided heat generation via resistive heating, where the measured resistance of the film heater was 1030 ohm/□. A variable AC unit (from Staco energy product CO) was used to supply the necessary current to the film heater, where the supplied power was deduced based on RMS readings via a multimeter (75 III from Fluke). Silver paint (05001-AB from SPI-Paint) was applied to the edge of the film heater, where metal plates were placed on top of the silver paint as connections pads. The silver paint resistance was in the order of 1 ohm, which was much less than the film heater measured resistance. QD emitted light intensity was calibrated for surface

temperature measurement, where the emitted light intensity from the QDs was observed using a monochromic CMOS camera (STC-MBCM200U3V from SENTECH). The CMOS camera has a full spatial resolution of 2048 by 1080 and a maximum depth resolution of 12 bit. The parallel pixel access of CMOS camera promotes a higher frame capture frequency, relative to CCD camera [108]. In addition, a single pixel within the CMOS camera corresponds to an approximate area 41 µm by 41 µm with respect to the measured dimensions of QD-gelatin film. A longpass optical filter (LP590-58 from Midopt) was used to filter out the excitation light spectrum, while near UV LEDs (Oznium) with peak spectral emissions of 405 nm were used as an excitation source for the QDs. A second monochromic CMOS camera (STC-MBCM200U3V from SENTECH) was used to correct for the LED light intensity variation pertaining to the self-heating of the LEDs. Details of the dual LED-QD intensity calibration with temperature will be discussed in the next subsection.

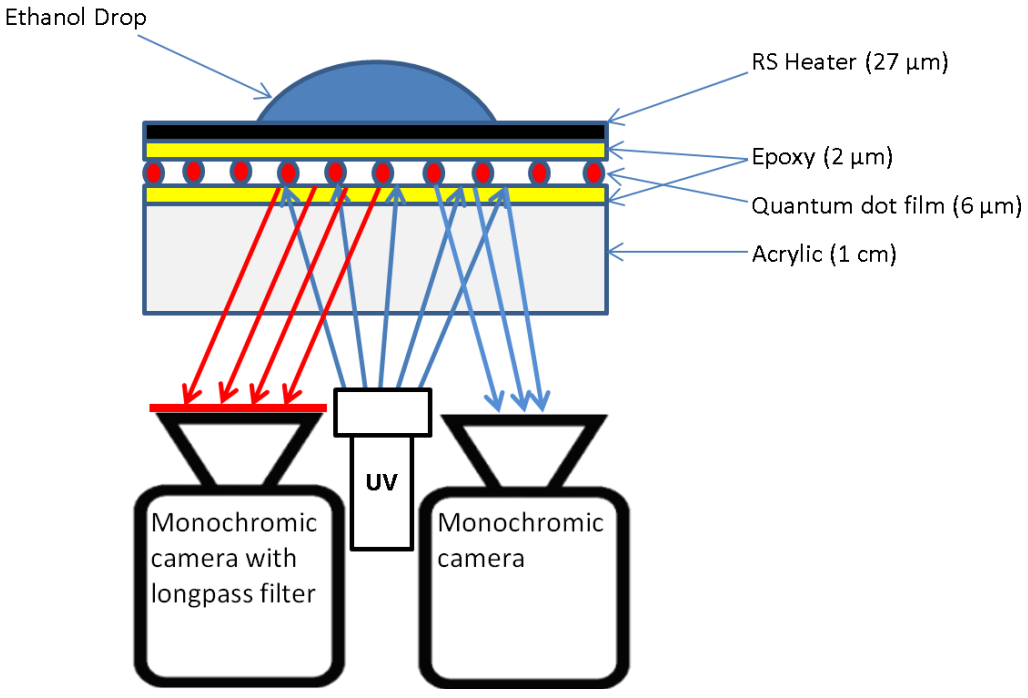

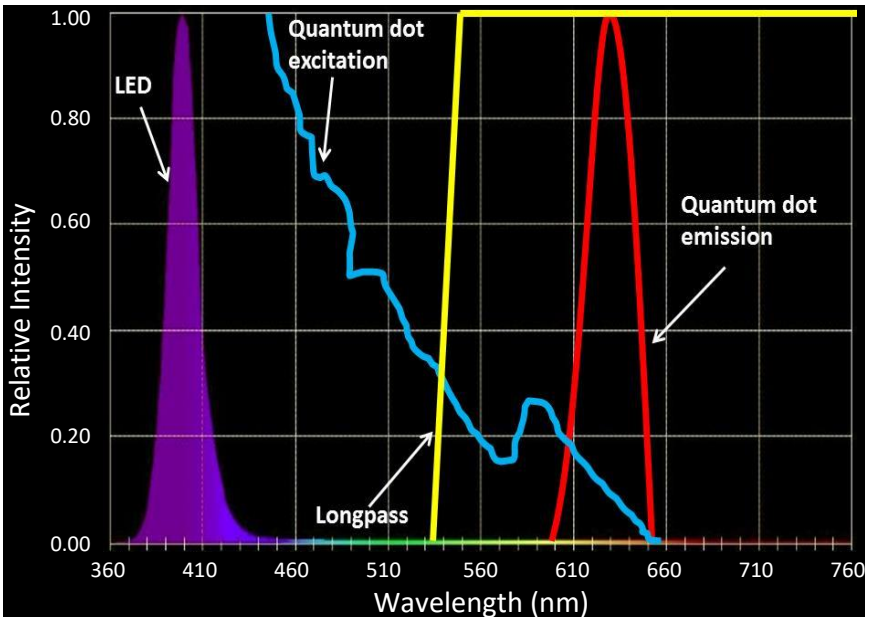

Figure 10: Test section and spectral characterization

Table 2: Ethanol properties

Density (kg/m^3)	786
Specific Heat (J/kg·K)	2460
Latent Heat of Vaporization (kJ/kg)	183

4.2.3 Procedures

The QD light intensity was calibrated with respect to both surface temperature and the LED intensity. In practice, images were simultaneously captured from both monochromic cameras, where both the QDs and the LED light intensity were separately observed by each camera. A continuous stream of images was captured for a duration of 5 seconds at each temperature during which the LED intensity was varied. A copper block was used to provide a uniform surface temperature on the film heater via a PID controlled cartridge heater, embedded within the copper block. The QD-gelatin film was assumed to be at the same temperature as the copper block since the thermal mass and thermal diffusivity of the copper block were much larger than

that of the QD-gelatin film. The calibration spanned a temperature range from 40°C to 140°C at an increment of 3°C. The achieved temperature resolution was around 25 bit per °C on 12 bits depth scale, which corresponds to a temperature sensitivity of 0.83% per °C. Figure 11 illustrates a 2D calibration profile for one of the observed pixels, which was based on a 3rd order polynomial fitting.

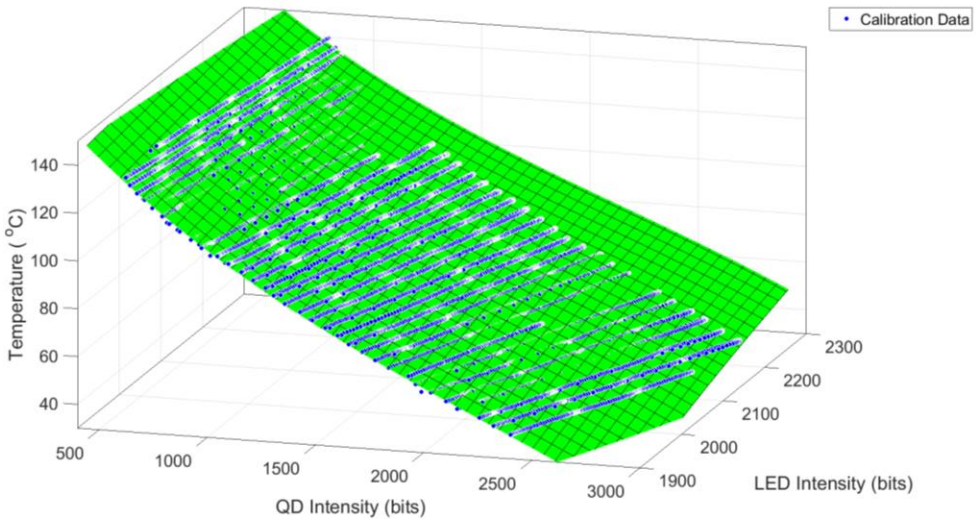

Figure 11: 2D calibration profile

4.2.4 Uncertainty Analysis:

The uncertainty (σ) in the temperature measurement was computed based on the propagating error of both the LED (I_{LED}) and QDs (I_{QD}) intensities, and it is given by Equation 25.

$$\sigma_T = \sqrt{{\sigma_{I_{QD}}}^2 \left(\frac{\partial T}{\partial I_{QD}}\right)^2 + {\sigma_{I_{LED}}}^2 \left(\frac{\partial T}{\partial I_{LED}}\right)^2} \tag{25}$$

The uncertainty in the temperature measurement for various heat generations (q''_{gen}) and QD excitation energies are given by Figure 12 and 13. A lower uncertainty in the temperature measurement is achieved for a higher QD excitation energy, which can be associated with a higher signal to noise ratio as shown in Figure 14. Further

reduction in uncertainty can be achieved by using a CCD camera, which has a lower noise relative to a CMOS camera. Pixel averaging can further reduce the inherent noise of a camera, which can bring about a lower uncertainty at the expense of the spatial resolution. Table 3 shows the uncertainty in the heat flux, which increases with the heat generation. The heat flux uncertainty was acquired from error propagation of various parameters, such as material properties and thicknesses. The sensitivity of the heat flux required in the uncertainty calculation was acquired by slightly perturbing the various parameters, where the heat flux was recalculated and its change relative to different parameters perturbations gave the heat flux sensitivity. Further details of this method can be found in [4].

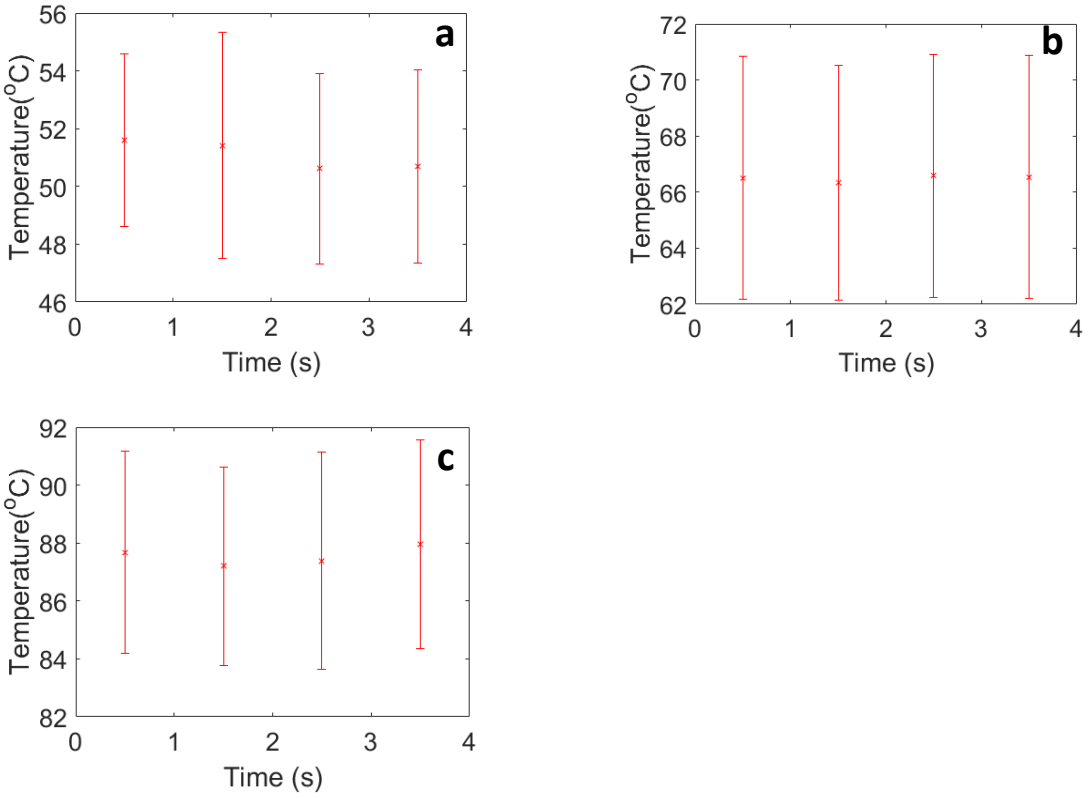

Figure 12: Q D temperature measurement prior droplet at low QD excitation energy; (a) q''_{gen}=931 W/m^2, (b) q''_{gen}=1421 W/m^2, (c) q''_{gen} =2063 W/m^2

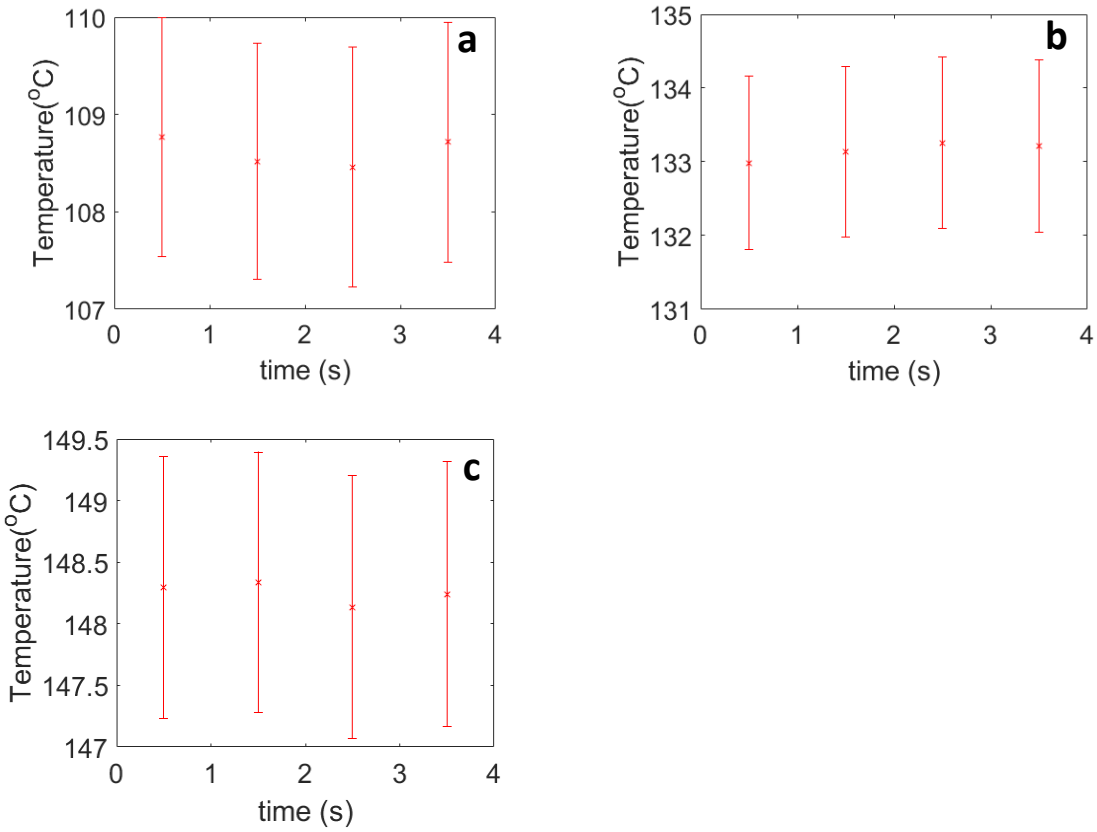

Figure 13: QD temperature measurement prior droplet at high QD excitation energy; (a) q''_{gen}=3125 W/m^2, (b) q''_{gen}=3592 W/m^2, (c) q''_{gen}=4041 W/m^2

Table 3: Heat flux uncertainty (95% confidence interval)

Heat Generation (W/m^2)	3125	3592	4041
Heat flux uncertainty (W/m^2)	232	272	308

4.3 Numerical Analysis

4.3.1 Heat Flux Calculation

Figure 14 shows a schematic of the numerically resolved regime required to deduce the surface heat flux associated with ethanol drop vaporization, via inverse heat conduction problem (IHCP). Details of IHCP calculations can be found in Appendix A, which follows the method enacted in a previous work by Moaveni and Kim [109].

The corresponding thermal resistance circuit representation is shown in Figure 15. The numerical computation comprises of first deducing the amount heat conducted into the acrylic plastic. This is achieved by computing the temperature distribution within the acrylic plastic, which is resolved implicitly via back-difference discretization scheme. The initial temperature distribution(T_N^t) in the heat Equation is acquired by resolving the temperature distribution as a steady state problem. The temperature evolution through acrylic plastic is resolved as transient problem from which the amount of heat conducted into the acrylic plastic is computed. The solution scheme involves using two boundary conditions one of which is the measured temperature at the quantum dot layer. The noise within the temperature measurement is smoothened out using a Gaussian filter which would otherwise amplify in the heat flux calculations. The thermocouple measurement at the other side of the acrylic plastic provides the second boundary condition, which was taken as a constant temperature boundary condition. Once the temperature distribution within the acrylic plastic is known at every time step, the surface heat flux can be inversely reconstructed from the knowledge of previous nodes within acrylic plastic. The temperature distribution through the epoxy and the film heater were solved as a quasi-steady state problem since the heat penetration speed is faster than the frame capture rate. The heat penetration speed is estimated from semi-infinite slab model in Equation 26, where $\propto_t$ is the thermal diffusivity and Δt is the time step. The Corresponding heat penetration speeds for the film heater and the epoxy are 23.4 mm/s and 4.7 mm/s, respectively.

$$u = \frac{1.8\sqrt{\alpha}}{\sqrt{\Delta t}} \tag{26}$$

In addition, the heat Equation is discretized in one dimension, which can be justified by the larger temperature gradient along the depth direction [2]. The heat convection associated with the ethanol drop vaporization ($q''_{convection}$) is acquired by deducting heat conducted to the substrate ($q''_{substrate}$) from the heat generated at the wall (q"gen) as shown in Equation 27. Material properties of the three layers are given by Table 4.

$$q''_{convection} = q''_{gen} - q''_{substrate} \tag{27}$$

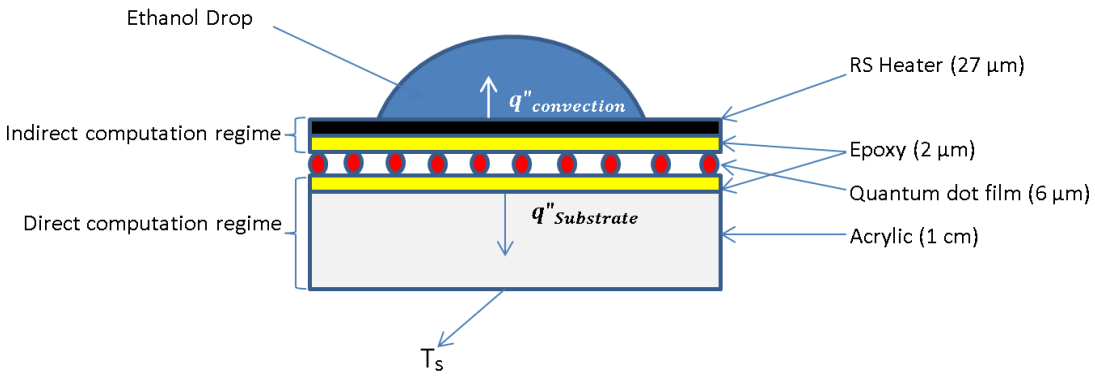

Figure 14: Schematic of the numerically resolved regime

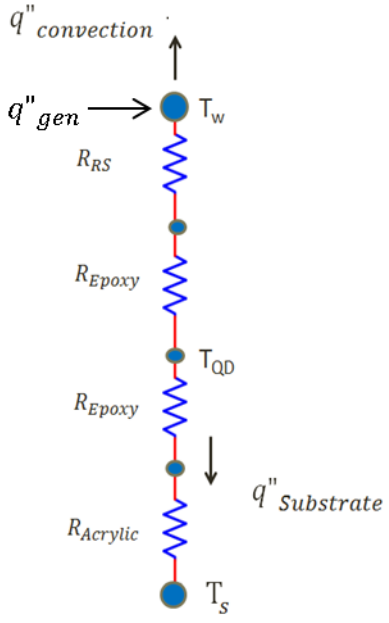

Figure 15: Thermal resistance circuit representation

Table 4: Material properties

Material	Thermal Conductivity (W/m·K)	Specific Heat (J/kg·K)	Density (kg/m^3)
RS film	3	710	2250
Epoxy	0.12	1090	1420
Acrylic	0.19	1470	1180

4.3.2 Numerical Validation

The numerical model was validated in two stages involving IHCP, as well as comparisons to analytical solutions for semi-infinite solid with common boundary conditions. The results for the inverse problem as well as for the three investigated boundary conditions are shown in Figure 16. The initial temperature of the solid materials was set to 20^{o}C, while the analytical solutions for constant wall temperature, constant heat flux, and convection boundaries are given by Equations 28-30, respectively.

$$\mathrm{T(y,t)} = (\mathrm{T_i} - \mathrm{T_w})\mathrm{erf}\left(\frac{\mathrm{y}}{2\sqrt{\alpha \mathrm{t}}}\right) + \mathrm{T_w} \tag{28}$$

$$T(y,t) = \frac{2q"_o \left(\frac{\alpha t}{\pi}\right)^{\frac{1}{2}}}{k} exp\left(\frac{-y^2}{4\alpha t}\right) - \frac{q"_o y}{k} erfc\left(\frac{y}{2\sqrt{\alpha t}}\right) + T_i \tag{29}$$

$$T(y,t) = (T_\infty - T_i)\left(erfc\left(\frac{y}{2\sqrt{\alpha t}}\right) - \left[exp\left(\frac{hy}{k} + \frac{h^2 \alpha t}{k^2}\right)\right]\left[erfc\left(\frac{y}{2\sqrt{\alpha t}} + \frac{h\sqrt{\alpha t}}{k}\right)\right]\right) + T_i \tag{30}$$

The imposed convection boundary with an oscillatory behavior was numerically reconstructed via IHCP method. A high heat convection boundary was applied at the wall surface, so as to numerically simulate a constant temperature boundary condition. The heater wall was treated as an adiabatic surface, so as to numerically simulate a constant heat flux boundary condition. As for the constant

convection boundary condition, the heat generation term was set to zero within the numerical model. Compared to the analytical solutions, the numerical results had a strong regression for the corresponding boundary cases, which supports the robustness of the adopted modeling technique.

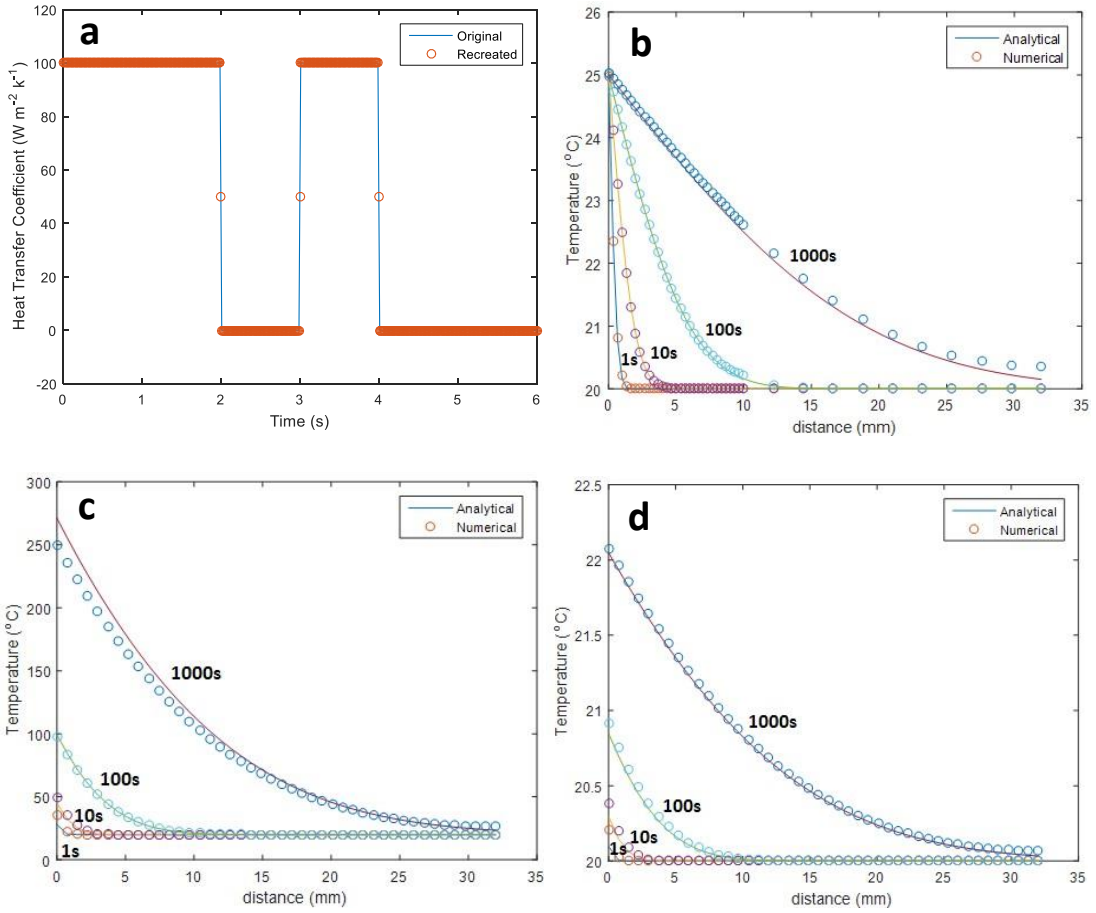

Figure 16: Schematics and the analytical-numerical results; (a) oscillatory convection boundary, (b) constant Temperature boundary, (c) constant heat generation flux, (d) convection boundary

4.4 Results and Discussion:

4.4.1 Ethanol Droplet Vaporization:

The ethanol drop vaporization test was conducted at various heat generation settings where the surface temperature measurements via QDs-gelatin film were used to compute the surface heat flux. A lab quality pipettor (V20 from VWR) was used to draw and place ethanol drops on top of the film heater. A thermocouple measurement was taken at the bottom of the acrylic plastic surface, which was used as a boundary condition within the numerical calculations. All of the experiments were conducted at steady state conditions, where the film heater was left to heat up for a sufficient amount of time.

Figure 17 shows both the surface temperature and heat flux distribution associated with the ethanol drop vaporization, where the film heater was set at 3125 W/m^2. Initially, the surface heat flux distribution rose up to a maximum, which took around half of a second from the drop placement. The peak in the surface heat flux distribution corresponds to the beginning of the vaporization process. The droplet expanded to a maximum diameter, where an uneven temperature profile existed between the droplet center and its outer rim as shown in Figure 17 at around 1.5 seconds of the droplet placement. This temperature profile took the form of alternating spirals, which is similar to the observation made by several studies of sessile droplets under IR thermography [5, 73-75]. Such behavior was attributed to non-uniform temperature gradients arising from the evaporation process, which brings about a variation in the surface tension. As mentioned in the literature section, a recirculation region in form of vortices is induced, which can be asymmetric in

nature and it is known as Marangoni effect. The thermal properties and viscosity of the fluid has a large impact upon convective cells, as emphasized within Karapetsas et al [75] study.

As the vaporization progressed, the spiral patterns vanished from the surface, while the drop size started to shrink due to the evaporation taking place at the drop contact line. The registered heat flux was highest around that region. At around 7.5 seconds, the temperature was generally uniform in distribution, which implies a transition in the heat transfer mechanism to thin film evaporation as was described by several studies in the literature [5, 73-74]. The process proceeded until the ethanol drop has completely vaporized, where the surface heat transfer mechanism switched to natural convection.

Compared to the studies from literature, there was a limitation in the concurrent study with respect to the discernable fluid structures, which cannot be accessed without a direct view as was noted by Sefiane et al [71]. Yet, the acquired data from the concurrent study shows a good concise with the IR observations in the literature with respect to the thermal distribution behavior. Figure 18 summarizes the vaporization process with respect to both temperature and heat flux evolution at the drop center, for a film heater generation flux of 3125 W/m^2. The maximum heat flux corresponds to the first inflection point within the temperature plot beyond which the heat flux starts to drop. Once the convection cell ceased to exist, the heat flux flattens out and the temperature profile changes in gradient with respect to time, which signals the change in heat transfer mechanism to thin film vaporization. Finally, the heat flux drops sharply to natural convection values and the surface temperature rises back exponentially to the initial state, once the ethanol drop has completely vaporized as shown in Figure 18.

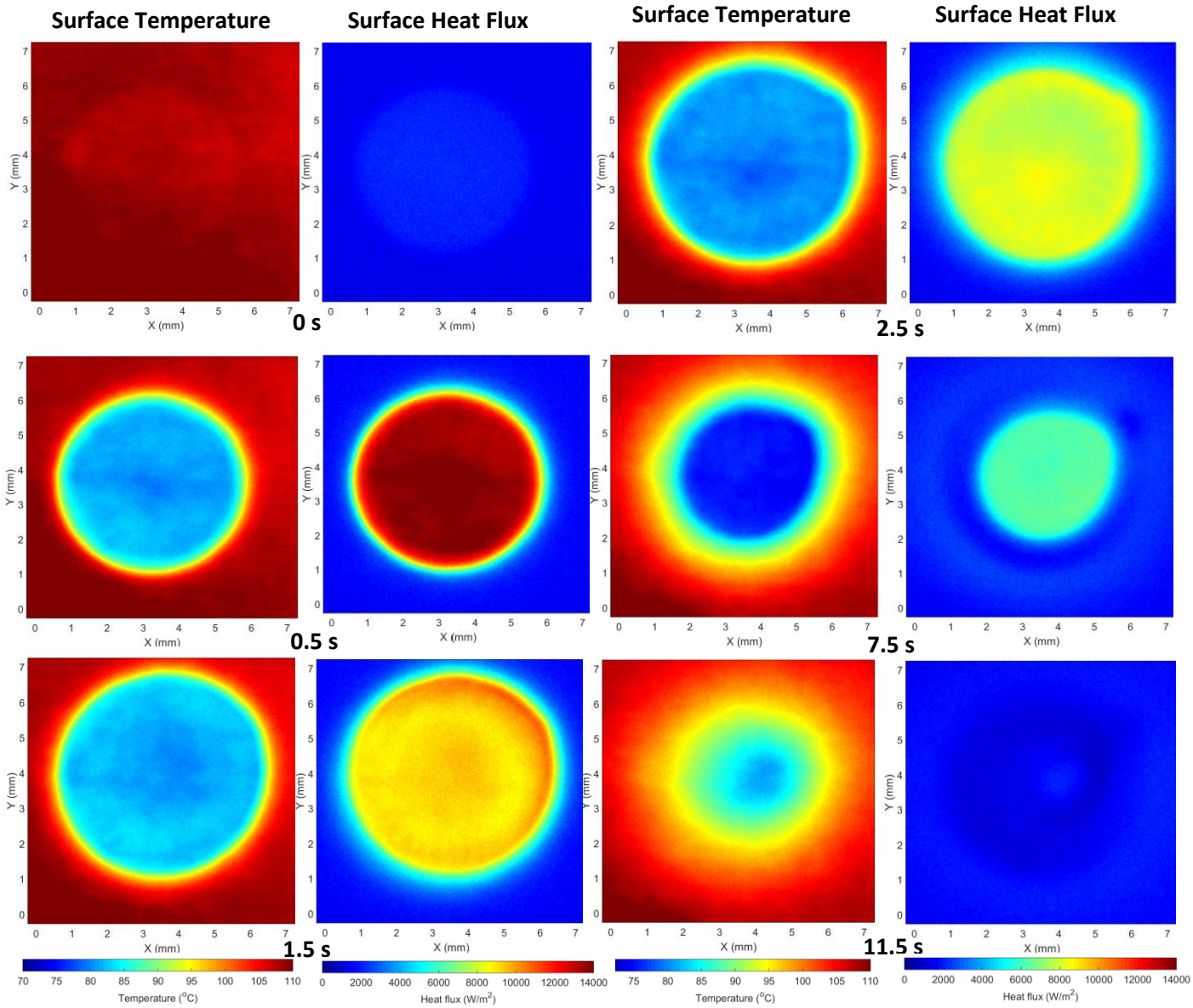

Figure 17: Temperature and heat flux surface profile of ethanol droplet with time, for a substrate heat generation flux of 3125 W/m^2

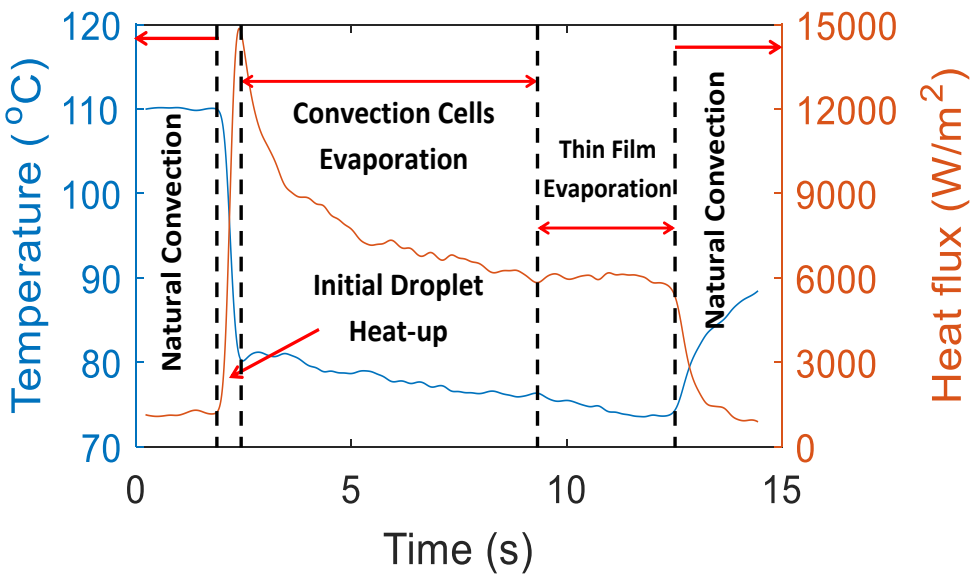

Figure 18: Temperature and heat flux evolution at ethanol droplet center, for a substrate heat generation flux of 3125 W/m^2

4.4.2 Effect of Heat Generation:

Figure 19 shows the evaporative flux coefficient as a function of the dimensionless time with respect to the total evaporative time. The evaporative heat transfer coefficient (h_{evap}) is acquired by subtracting the natural convection heat flux ($q"_{natural}$) from the surface heat flux ($q"_{surface}$) and then dividing it by the difference between the wall temperature (T_w) and the ambient temperature (T_∞) as defined by Equation 31.

$$h_{evap} = \frac{q"_{total} - q"_{natural}}{T_w - T_\infty} \quad (31)$$

A higher evaporative heat transfer coefficient was observed at a lower heat generation levels, where the profile flattens out faster at a higher heat generation levels as shown in Fig 19. This might indicate a lower population of convection cells at a higher heat generation, where thin film vaporization might be the dominant mechanism of heat transfer. Also shown in the inset pictures of Figure 19 are visualization of the drop at

different times. A higher evaporative flux was associated with taller drops relative to the thinner film of the ethanol drop, which might imply an enhanced surface heat transfer via convecting vortices. Otherwise, a lower evaporative heat flux would have resulted via surface heat conduction due to the drop thickness. Such conjectures are supported by the observations within Sefiane et al [71] study, where the "visible waves" declined with the reduction in the drop height. In addition, Sobac and David [5] linked the evaporative flux in their study with the "thermal-convective instabilities". Table 5 shows the integrated energy associated with the ethanol drop vaporization for various heat generation fluxes. The corresponding total mass of evaporated ethanol is also shown in Table 5, which was acquired by dividing the integrated energy by the latent heat of vaporization. The computed mass of the vaporized ethanol droplet was reproducible with respect to the various heat generation levels, where the observed deviation from the average computed mass was around 0.3 mg.

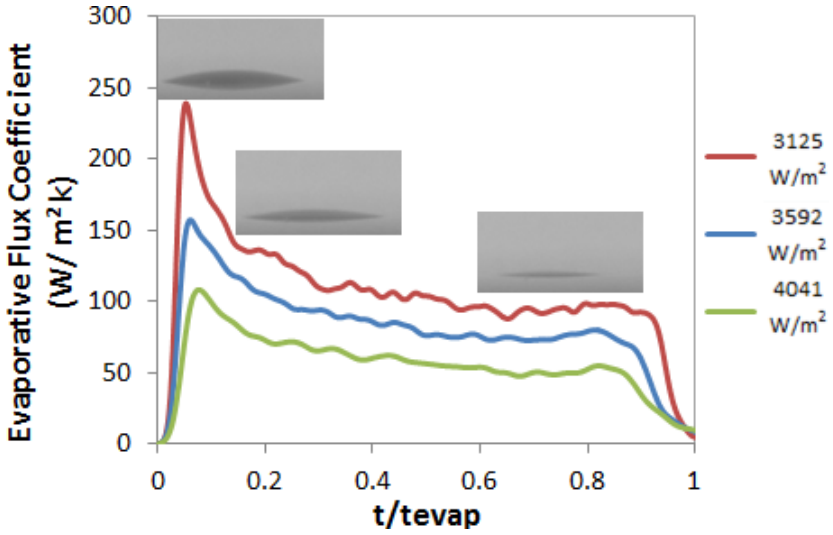

Figure 19: Evaporative flux coefficient as function of dimensionless time, for different substrate heat generation flux

Table 5: Integrated energy and computed droplet mass for various substrate heat generation flux

Heat generation flux (W/m^2)	Integrated energy (J)	Computed drop mass (mg)
931	1.4	1.7
1421	1.2	1.5
2063	1.7	2.0
3125	1.6	1.9
3592	1.3	1.6
4041	1.2	1.4

5. Pool Boiling: Experimental Facility and Data processing

5.1 Introduction

This chapter provides details of the experimental facility used in the pool boiling study at various heat flux conditions, along with a description of the thin TSP film formulation, used for the local intensity measurement purposes. Data reduction and uncertainty analysis are provided at the end of this chapter. Ruthenium based TSP was used within pool boiling application instead of quantum dot, due to its lower cost, where 50 mg of QD (CDSe/ZnS) costs $449 and 1 gram of Ruthenium compound costs $101. In addition, TSP has higher temperature sensitivity than QD, which is around 4 times that of QD.

5.2 Temperature Sensitive Paint

The temperature sensitive paint (TSP) comprises of fluorescing luminophore and the binder. A Ruthenium complex compound (Ruthenium tris(1,10-phenanthroline) dichloride) from Sigma Aldrich) was chosen as the fluorescing luminophore due to its optical attributes. For instance, it has a relatively high temperature sensitivity, in the order of 2% per ^{o}C, and a short decay time (<1μs) that promotes a fast response time to temperature changes with respect to the emitted intensity, according to Mills [110]. In addition, the spectral properties of Ru complex compound tend to exhibit a large stokes shift, which can also be used as a temperature indicator. Similar to other fluorescing materials such as the quantum dot, affordable light with short wavelength emission range, such as UV LED, can be used as an excitation source for the luminophores. Polyacrylic acid was used as a binder for the luminophores due to its impermeability to oxygen, where some of the luminophores including the Ruthenium

complex compound are known to be sensitive to oxygen concentration. The TSP was delivered to the target surface in a solution form, where both the Luminophore and the binder were dissolved in isopropanol, a high wetting solvent. Ozawa et al [67] recommended that the Ruthenium compound to be dissolved in ethanol with a molarity of 0.16 mol/l, while Huang [65] suggested that the ratio of the dissolved Ruthenium compound to the Polyacrylic acid, within ethanol, to be 1:2. Several tests were conducted in order to characterize the dependency of the TSP on prominent factor that might influence its emitted intensities. The following subsections documents the results of those potential factors.

5.2.1 Temperature Dependency

The spectral characteristics of the LED emission and TSP emission wavelength, along with cutoff spectrum of the long-pass filter are shown in Figure 20 along with a typical calibration curve for one pixel in a CMOS camera (Phantom Miro eX4). The intensity shown is the time averaged value over 1 s taken at a frame rate of ~100 Hz. The intensity at a given LED illumination decreases with temperature. The temperature resolution was quite high even where the sensitivity is lowest (~16 bits/°C at 97°C), indicating accurate steady state measurements can be obtained by time averaging. A higher order polynomial was used since it could fit the data with less uncertainty than a logarithmic fit. Variations in the LED intensities were accounted for in the calibration by measuring the TSP intensity at different LED intensities at each temperature level.

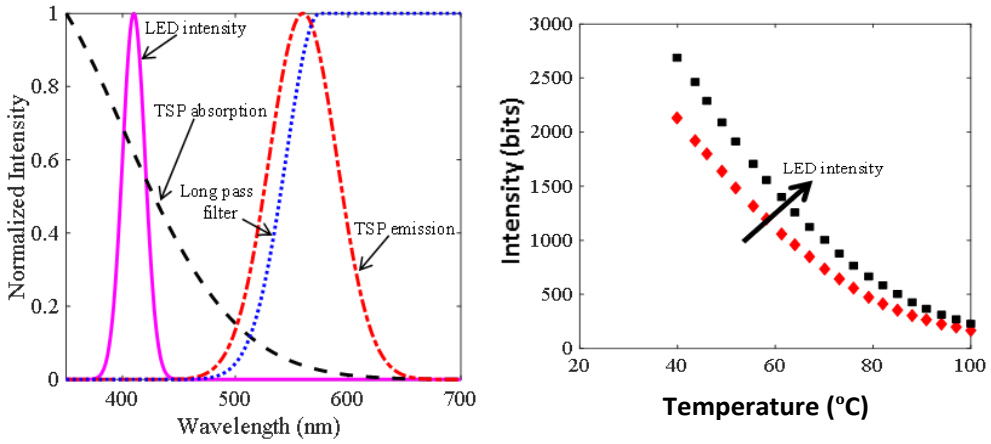

Figure 20: Spectral and emission intensity characterization. Left: Spectral characteristics of the emission and excitation sources. Right: TSP intensity characteristics with temperature and various LED intensity.

The camera noise (RMS of the intensity) was significant and resulted in much higher uncertainty for unsteady measurements. The noise had a high dependency upon the camera's inherent noise, as shown in Figure 21. The noise increases with emission intensity but becomes a smaller fraction of the intensity, so the uncertainty in temperature decreases with intensity. Based on the camera noise and the calibration, the uncertainty in temperature (95% confidence interval) at a given pixel for a mean intensity of 4000 bits was: Sentech (STC-MBCM200U3V): ±2°C; Point Grey (FL3-U3-13S2M-CS): ±0.5°C; Phantom: ±0.7°C. The Phantom camera was chosen for the TSP measurements due to its ability to acquire data at higher speeds and spatial resolution with relatively little noise. Spatial and temporal averaging can mitigate the observed noise, where the latter can bring about a higher spatial resolution in the presence of high speed photography,

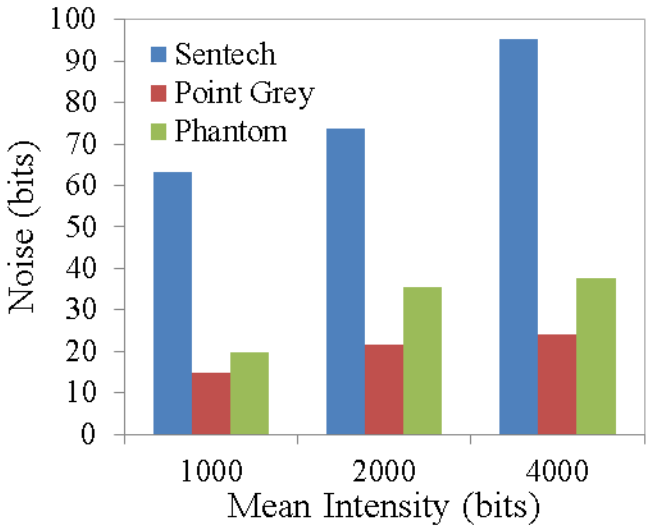

Figure 21: Noise for three 12-bit CMOS cameras at a representative pixel

5.2.2 Pressure Dependency

Figure 22 shows the TSP intensity variation with surrounding pressure, which covers pressure ranges from vacuum to atmospheric pressures. The surface temperature was maintained at 31.8°C for the duration of the test. The TSP exposure to a LED light source was limited to within the measurement time frame, so as to minimize the effect of photobleaching and effectively segregate out the effect of pressure upon the temperature reading. As shown in Figure 22, the TSP intensity has a low sensitivity with pressure, which further supports the assertion of polyacrylic acid as an impermeable binder as observed by Lee et al [60].

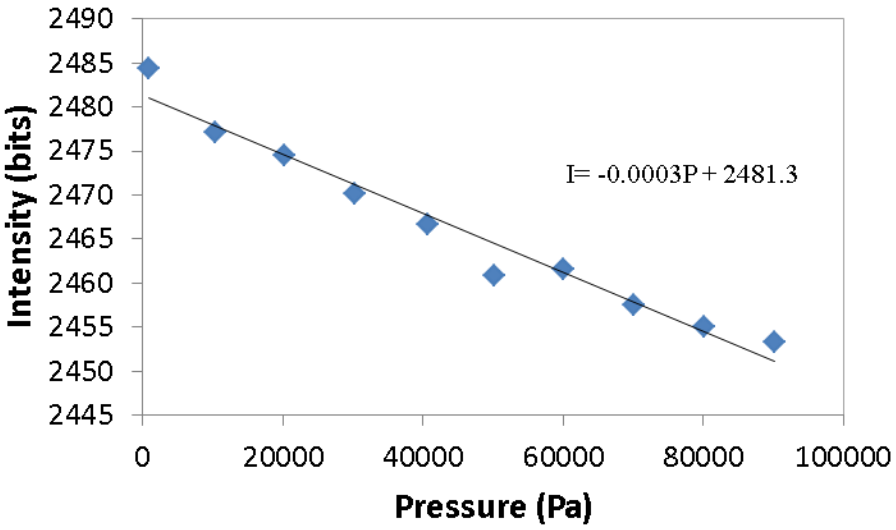

Figure 22: TSP Intensity versus surrounding pressure

5.2.3 Aging Dependency

TSPs can be damaged by exposure to UV and result in lower emission in a phenomena referred to as photobleaching, which is the permanent loss of the luminophore light emissions. As shown in Figure 23, there are signs of degradation within the TSP emission intensity, which was caused from prolonged exposure to LED light. To characterize the aging effect in our measurements, the decrease in emission with time was measured from a TSP film under representative UV illumination. Photobleaching resulted in a 2-3% reduction in TSP intensity over two hours, indicating that exposure to UV should be minimized during both calibration and testing.

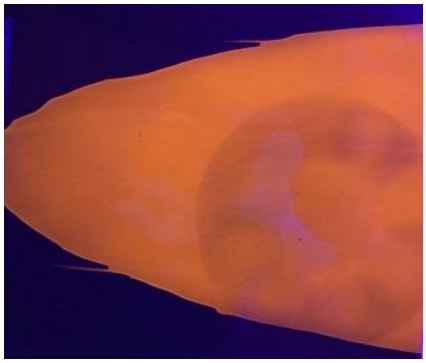

Figure 23: Illustration of photobleaching effect

(Courtesy of Caleb Hammer)

The Previous results can imply a stable test strategy in calibrating the temperature with respect to the TSP intensity, where the TSP should be exposed to an excitation source only during the measurement time. In addition, the effect of the LED variation can be corrected by observing it simultaneously with the TSP intensity. Another way to tackle the variation in the excitation source is by mixing the TSP with temperature insensitive luminophores, which can correct for the intensity variation of the excitation light source, as suggested by Kurits [62] and Ozawa et al [67].

5.3 Test section

Figure 24 shows a schematic of the Test section component. The construction of the test section is as follows: First, 200 nm of Germanium metal were deposited on an adhesive layer (25µm 8146 from 3M) in form of circular shapes, which had a maximum diameter of 400 µm and were 3 mm apart, as shown on Figure 25. The Germanium patterns were achieved via liftoff technique, where a polymer sheet was laser cut into the desired shapes. These coatings would act as an opaque layer, so as to prevent the excitation of the TSP layer closer to the working fluid. . Properties of the acrylic adhesive were measured and are given in Table 6. Details of the test apparatus

and the experimental procedures used to determine the acrylic adhesive thermal properties are given in Appendix B. Afterwards, dots of isopropanol based TSP, around 2 µm, were placed on top of the Germanium patterns, using a fine brush set, which would act as a temperature indicator on the sapphire surface (Rayotek sight window). The coated adhesive was attached to the sapphire surface with the TSP dots facing it. Afterwards, a thin layer of TSP was spread on top of a double sided tape (5µm 82600 from 3M) via a size 3 formed mayer rod, from RD specialties, where the achieved TSP thickness was around 2 µm. The TSP coated double side tape was attached to the 25µm adhesive, where the TSP layer was encapsulated between the two adhesives. In the preparation of the TSP solution, associated with the layer closer to working fluid, Isopropanol solvent was also used to deliver the TSP to the adhesive layer. A TCR metal sheet, comprising of 18µm of copper layer and 100nm of Nichrome layer, was placed on top of the 5µm adhesive, where the copper layer was partially etched with ferric chloride solution. The nichrome surface was exposed on the etched areas of the copper surface. The remaining copper area, designated as an electrical connection pad, was protected from ferric chloride via a tape mask. The exposed Nichrome film was used as a heater during the boiling experiment, which had an electrical resistance was 25 ohm/□. A depiction of the nichrome heater is also shown in Figure 25. A DC power supply (Hewlett Packard 6675A) was used to power the film heater, where voltage measurements were taken independently, via multimeter (Hewlett Packard 34401A), along a separate copper wire connections. A CMOS camera (Phantom Miro eX4) was used to monitor the TSP intensity at a frame rate of 225 Hz, which has a pixel resolution of 800 x 600 and an intensity depth

resolution of 12 bits. The high frame rate is essential in resolving the fast temporal wall-fluid interaction; especially, at CHF conditions involving rapid wetting film motion. An optical longpass filter (LP590-58 from Midopt) was used to separate the UV LED light (semi-LED from LED supply) from the TSP emission. A lens (EX S) with a focal length of 105mm and an f-stop of f/2.8 was used in conjunction with 36mm extension and 2x objective lens, so as to achieve a spatial resolution of 23 μm per pixel of the CMOS camera sensor. A photomultiplier (R3788 tube from Hamamatsu) was used to observe the variation within the LED, and thus, it was incorporated into the TSP intensity calibration with temperature. A short pass filter (Alluxa 430 OD6 SP) placed in front of the PMT filtered out the TSP emission. The absolute intensity from the LED was observed to be in the order of 28 klux, detected using a light meter (CEM DT-1309). The test section was enveloped within a black enclosure, so as to minimize external light effects.

Table 6: Acrylic adhesive properties

Thermal Conductivity (W/m·K)	0.21
Specific Heat (J/kg·K)	1800
Density (kg/m^3)	1180

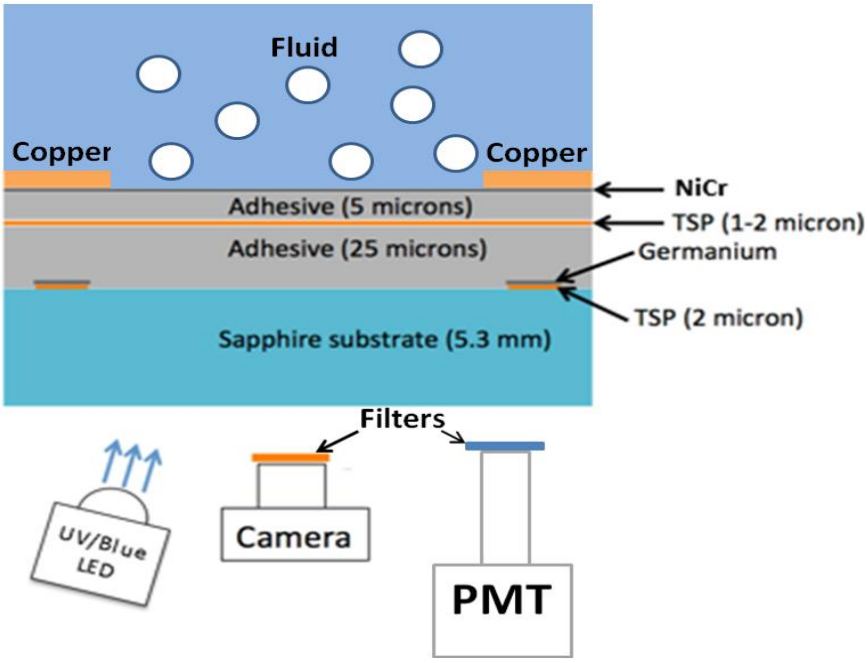

Figure 24: Test section schematics

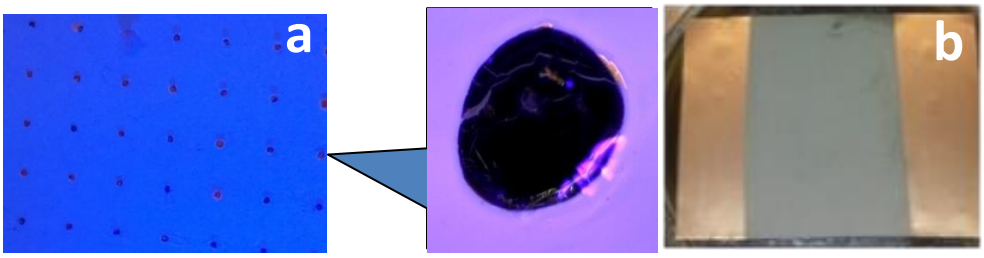

Figure 25: Depiction of test section layer; (a) Germanium dot, (b) Nichrome heater

5.4 Pool Boiling Facility:

Figure 26 shows a schematic of the pool boiling setup. The test facility consists of three major Sections, which includes the boiling chamber, a degassing circulation unit, and the test section. Detailed drawing of the boiling chamber can be found in the Appendix C. The main test chamber consisted of an aluminum vessel 11.7 cm high and 15 cm in diameter. The test section was located at the bottom of the pool. Initially, the boiling chamber was vacuumed prior the introduction of HFE 7500 (C9H5F15O, Tsat=128°C at 1 atm), which was utilized for calibration purposes,

spanning a temperature range from 40°C to 100°C in increments of 3°C. The chamber wall was patched with several film heaters, which was used to vary the working fluid temperature. The HFE 7500 was circulated within the boiling chamber during calibration in order to ensure uniform mixing of the working fluid. Thermocouples were used to ensure that the temperature difference between the bulk of the fluid and the TSP layer was minimal. Images were captured at ~100 Hz for 10 seconds at each temperature during which the LED intensity was varied. Upon calibration completion, the HFE 7500 fluid was drained out with the aid of Nitrogen gas flow. The boiling chamber was vacuumed again after which the working fluid for the boiling experiment, HFE7000 ($C_3F_7OCH_3$, T_{sat}=34°C at 1 atm), was supplied into the boiling chamber. The HFE fluid was circulated, via a gear pump, through a degassing membrane (Superphobic Membrane contactors), which was used to filter out non-condensable gases. A bellow situated on top of the boiling chamber was used to maintain the pressure within the boiling chamber at 1 atm with the aid of a chiller, as the supplied heat flux to the working fluid increases. Data were taken using the Phantom camera at a frame rate of 225 Hz. HFE7000 properties are provided in Table 7.

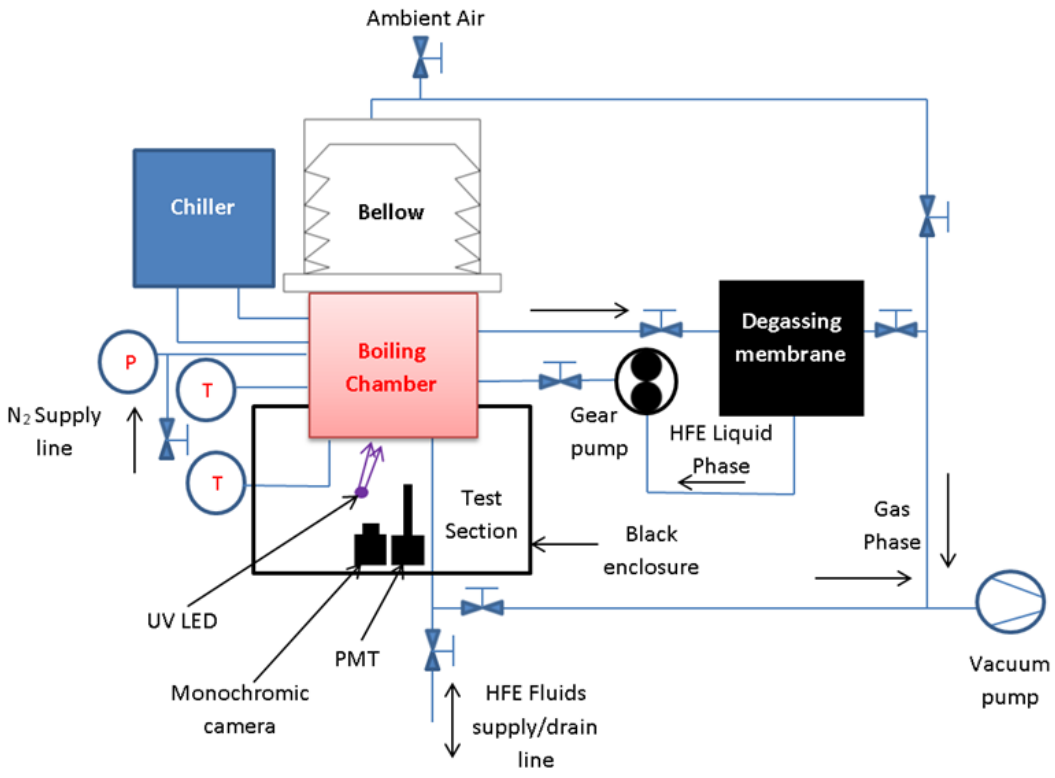

Figure 26: Pool boiling experimental facility

Table 7: HFE7000 properties @ 25ºC

Density (kg/m$^{3)}$	1400
Thermal conductivity (W/m·K)	0.075
Kinematic Viscosity (m^2/s)	3.2E-07
Specific Heat (J/kg·K)	1300
Surface Tension (N/m)	0.0124
Latent Heat of Vaporization (kJ/kg)	142

5.5 Data Reduction:

5.5.1 Heat Flux Calculation

The local surface heat flux was computed as a 1-D inverse heat conduction problem (IHCP), since the in-plane temperature gradients within the adhesive was much smaller than the normal gradient. The substrate was represented using the thermal circuit shown in Figure 27. The temperature variation within the TSP layer was neglected since it was so thin. The heat generated in the NiCr layer (q''_{NiCr}) was obtained from the voltage and current through the heater and the heater area. Part of this heat was lost through substrate conduction ($q''_{substrate}$), which could be computed from the measured values of $T_{TSP,top}$ and $T_{TSP,bottom}$ using an unsteady heat conduction code. The temperature at the adhesive/sapphire interface was obtained by interpolation between the temperatures measured using the dots, spaced 3 mm x 3 mm apart. This temperature was quite uniform relative to the wall-fluid temperature difference due to the high thermal conductivity of the sapphire. The transient temperature profile within the 25 μm adhesive at each pixel was computed, which was used to compute the heat conducted into the substrate. This heat loss was subtracted from the heat generated within the NiCr film in order to obtain the wall heat flux, which corresponds to the heat liberated into the fluid. The heat flux into the fluid (q''_w) is $q''_w = q''_{NiCr} - q''_{substrate}$. The wall temperature ($T_w$) was computed from $T_{TSP,top}$ and correcting for the temperature drop across the 5 μm adhesive$\left(T_w = T_{TSP} + \frac{q''_w * L_{adhesive}}{k_{adhesive}}\right)$. A description of the calculations can be found in a previous work by Moaveni and Kim [109].

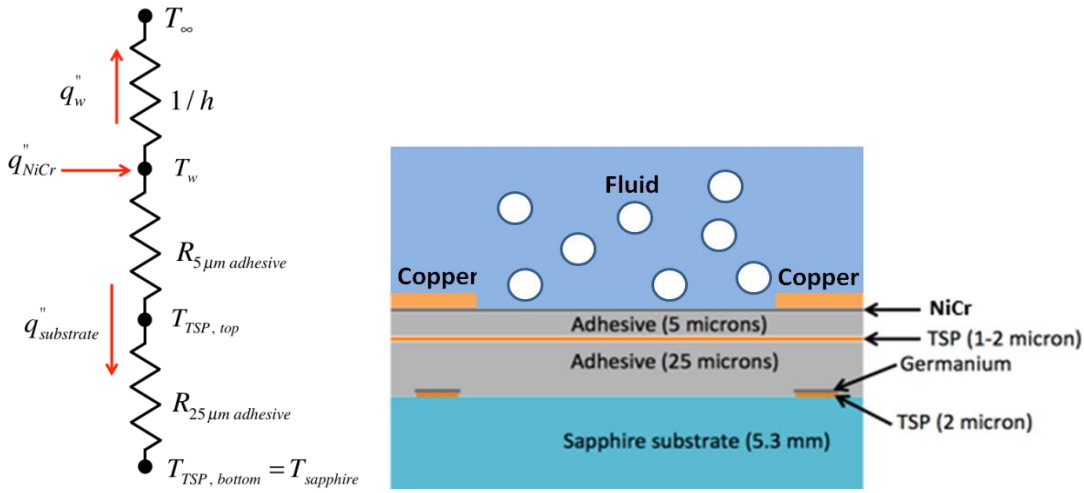

Figure 27: Schematic and thermal circuit representation of numerical model

Figure 28 illustrates a TSP intensity measurement and the corresponding wall temperature and surface heat flux, which was acquired from the 1-D transient heat conduction analysis for the pool boiling configuration for a heat flux of 1.5 W/cm^2.

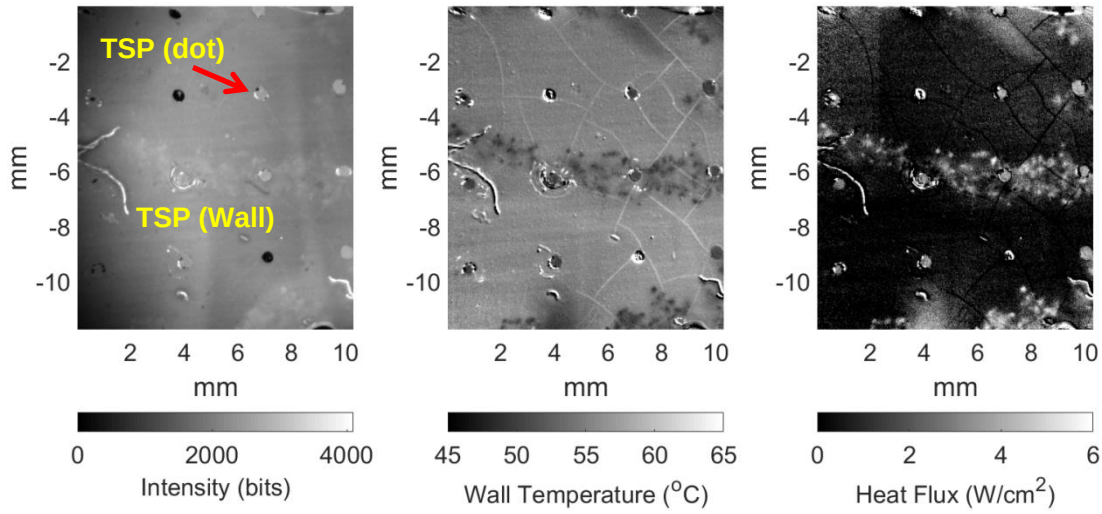

Figure 28: TSP intensity (left), the reduced wall temperature (middle), and wall heat flux (right)

The circular spots spaced on a 3 mm x 3 mm grid indicate where the temperatures of the adhesive/sapphire substrate were measured. Small cracks within the TSP are seen, but these had negligible effect upon the measurements.

5.5.2 Feature Extraction:

The contact line distribution and other relevant features were obtained from the surface heat flux distribution as follows: Starting with the heat flux data, a threshold function was defined such as to segregate the wet region from the dry area. Hence, it's assumed that the majority of the heat transfer occurs through the wet area, as illustrated in Figure 29. The vapor patch area covers the dry area, which represents areas with a surface heat flux below the chosen threshold. The contact line mapping, shown in Figure, is based on a logic function, which traces the boundary of the wet-dry area. The cells representing those boundaries are defined as wet cells whose adjacent cells are all dry. The dot features were suppressed within the contact line mapping.

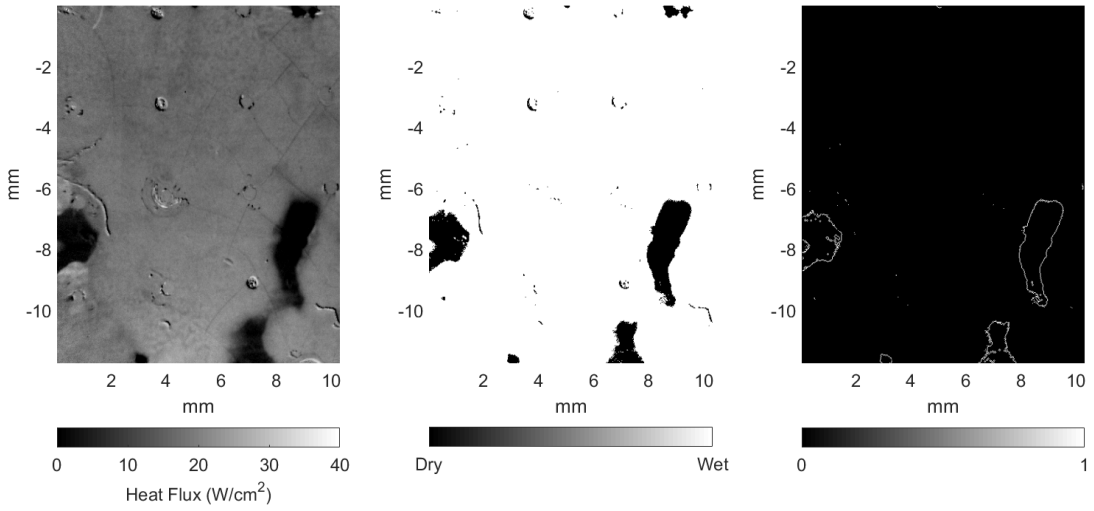

Figure 29: Experimental feature extraction based on surface heat flux threshold

The advancing and receding contact line are deduced by comparing the cells in the current frame with the same cells in the previous frames, as shown in Figure 30. Thus, the advancing contact line covers the cells that are wet in the current frame but dry in the previous frame and vice versa for the receding contact line. The

advancing and receding areas are defined in the same manner as the advancing and receding contact lines.

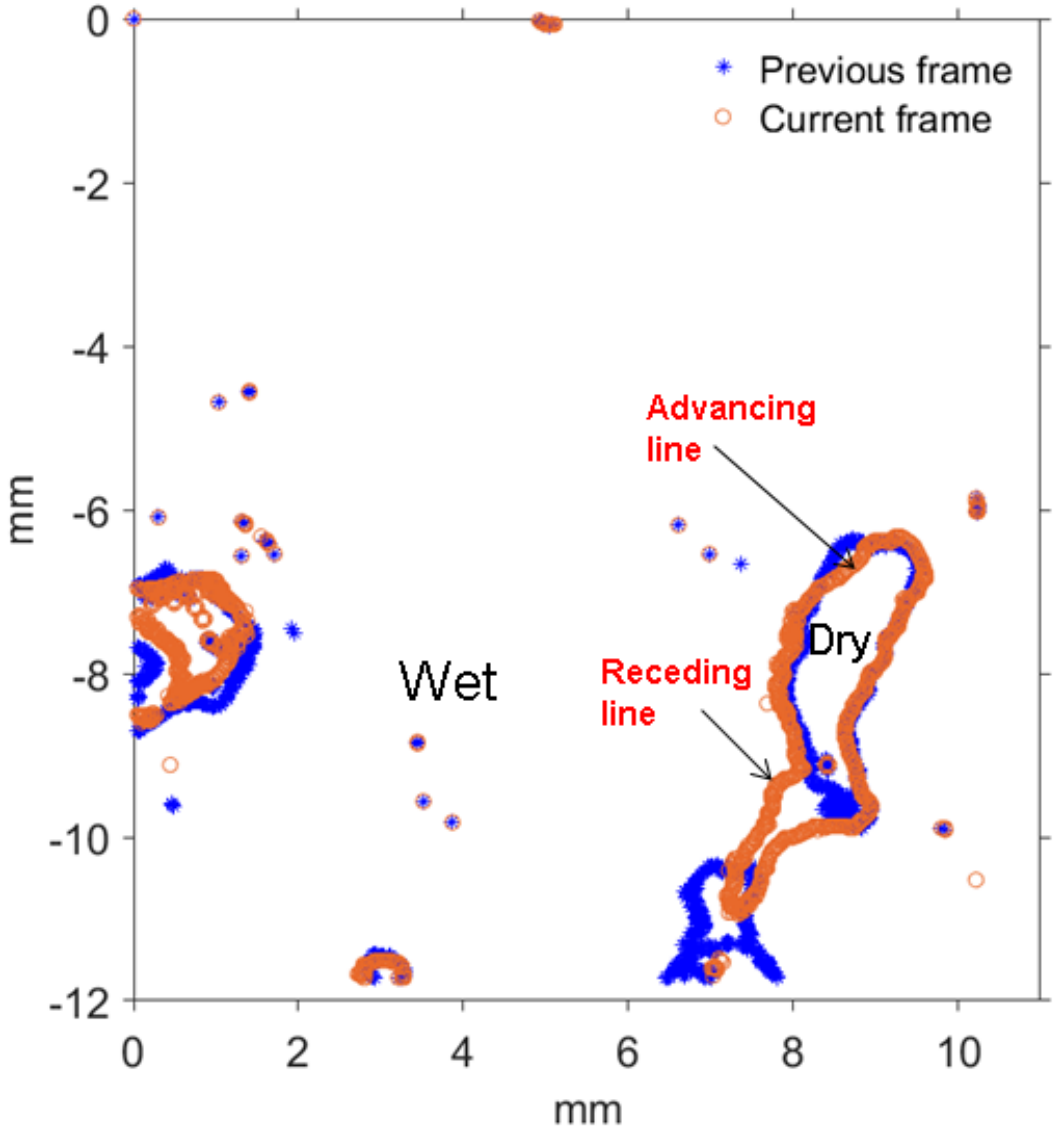

Figure 30: Illustration of the advancing and receding contact line

The advancing contact line speed is evaluated with respect to the area covered by the liquid area and the contact line length surrounding the advancing area, as shown in Figure 31 and it's given by Equation 32. This method follows Jung et al [83] area-based computational technique for contact line speed measurement.

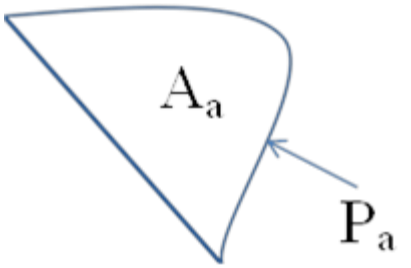

$$V = \frac{A_a}{\frac{1}{2}\, P_a\, \Delta t} \tag{32}$$

Figure 31: Contact line speed

Other parameters prominent to the analysis of the dryout behavior are the dryout frequency and the average duration of surface dryout. As shown in Equation 33, the dryout frequency was computed by evaluating the dryout occurrence within a given area for certain period of time.

$$f_{dry} = \frac{\sum_{i=1}^{N} T_i}{frames\, \frac{1}{fps} N} \tag{33}$$

where T_i is the number of times a pixel i would transition from wet to dry, at a given time period, fps is the frame capture speed by the camera, and N is the total number of pixels within an area. The average duration of surface dryout was evaluated by computing the average time duration of a surface dryout, prior the surface rewetting phase, as shown in Equation 34.

$$t_{dry} = \frac{\sum_{i=1}^{N} \frac{D_i \ \frac{1}{fps}}{T_i}}{N} \tag{34}$$

where D_i is the number of times a pixel i is dry, at a given time period.

5.6 Uncertainty Analysis:

Measurement uncertainty is related to the noise within the utilized instrumentation, which encompass the readings from both the LED and the CMOS camera. A summary of the various instrumentation uncertainties is given in Table 8. The readings from the photomultiplier involve converting light to measurable voltage readings, which involves cascade of photoelectron emissions within the photomultiplier tube. The current output from the photomultiplier is converted to a voltage signal, via a 10 kΩ resistor, which is fed into a microcontroller board (Ardiuno Uno) with a 16 bit analog-digital converter extension shield (Mayhew labs). The noise within the analog-digital converter component is examined using a voltage signal from a battery cell. The observed noise of the analog-digital converter was within 22 bits, which is much less than it's reading scale as shown in Table 8. As shown in Table 8, the noise within the photomultiplier is also relatively low compared to the analog-digital converter reading scale. In addition, the photomultiplier indicated the UV LED intensity was very stable. . Measurement uncertainty was dominated by the camera noise.

Table 8: Instrumentation uncertainties

Instrumentation	Model Name	Range	Error
A/D converter	Arduino w/shield	0-65536 bits	5-22 bits
Photomultiplier	R3788 -C6271	0-12V	1-2mV
CMOS Camera	Phantom Miro EX4	0-4096 bits	30 bits (at I=4000 bits)
Thermocouple	K-type	-200-1350 °C	±0.2 °C
Pressure transducer	Omega PX 212	0-2 bar	±400 Pa

The maximum temperature resolution within the experiment was ~50 bits/^{o}C. The errors associated with all of the instrumentation and the calibration accuracy

were propagated and used to compute the temperature uncertainty. The steady state uncertainty within the temperature readings was evaluated around 0.2 to 0.3 ^{o}C, while the transient uncertainty within the temperature readings was evaluated around 0.6 ^{o}C. The sensitivity of the wall heat flux to various parameters was determined by perturbing the parameters one by one and computing their effect. The final uncertainty in the wall heat flux is shown in Table 9 at various heat loads. Temperature measurement accuracy and calibration profiles can be found in Appendices D-F.

Table 9: Heat flux uncertainty (95% confidence interval)

Calculated Wall heat flux (W/cm^2)	1.5	9.0	13.6	17.2	20.3
Steady state uncertainty (W/cm^2)	1.2	1.2	1.2	1.2	1.2
Transient uncertainty (W/cm^2)	1.7	2.2	2.3	1.8	2.1

6. Pool Boiling: Experimental Results

6.1 Introduction

This chapter examines the reduced data from TSP intensity measurements, where the wall temperature variation and the heat flux measurements from the pool boiling of HFE7000 (C3F7OCH3, Tsat=34°C at 1 atm) are analyzed in the current chapter. Comparison of the data with CHF correlations and energy balances were used to validate the data. The characteristics of vapor patch formation and its development will be examined, which include the evolution of contact line and surface wet fraction with the wall heat flux. Such study would shed light on the mechanism of surface dryout near CHF condition, in the context of the previous observations from CHF studies in the literature.

6.2 Area Averaged Pool Boiling Measurements

The time and space averaged boiling curve is shown on Figure 32. The correct wall superheat to be used in the pool boiling curve was not the average heater temperature, but is dependent on the heater construction. With adhesive covering the sapphire, the sapphire temperature rises until the heat conducted through the adhesive matches the heat removed by the liquid. For a given heat flux, the magnitude of the rise in sapphire temperature depends on the adhesive thickness, *but the time averaged temperature at the NiCr-liquid interface remains constant*. When a portion of the heater is covered by a vapor patch, however, the NiCr-vapor interface behaves as an adiabatic boundary condition, since the heat transfer into the vapor is very small. As a consequence, the wall temperature increases and can reach the underlying sapphire

substrate temperature. The average wall temperature computed by averaging the temperature over the entire heater-liquid/vapor interface would then depend on the thickness of the adhesive. In the limit of zero adhesive thickness, the wall temperature in the vapor covered regions would be close to the temperature of the liquid covered regions, due to the high thermal conductivity of the sapphire substrate. Therefore, the wall temperature *was averaged over the liquid covered areas only*. The heat flux data in Figure 32 was acquired by multiplying the heat flux contribution from the liquid area ($q"_{liq}$) by the corresponding fraction (Wf) of the heater surface covered by liquid ($q" = q"_l x Wf$).

The wall heat flux increases rapidly once nucleation occurs at ~50°C due to the rapid spread of the nucleation sites on the surface until ~14.7W/cm2, followed by a decrease in the slope of the boiling curve as CHF is approached. The measured CHF is consistent with Leinhard and Dhir's [39] modification of the Zuber [95] correlation (Equation (13)), and with the Kandlikar [87] correlation (Equation (18)). An overall energy balance between the electrical power supplied to the heater and the computed wall heat flux is shown in Table 10. The agreement was within 20% for heat fluxes once boiling is fully established ($q"_w > 9$ W/cm2). The good agreement between the data and the correlations, along with the energy balance for the fully established boiling regime, provide validations of the current technique for the pool boiling configuration.

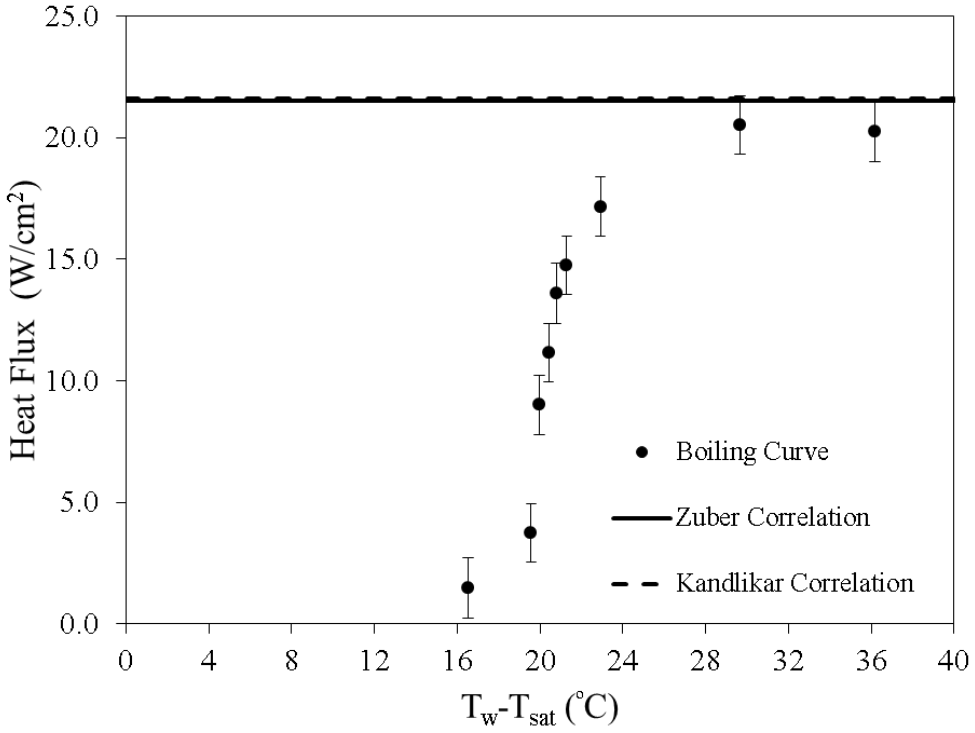

Figure 32: Pool boiling curve and comparison with CHF correlations

Table 10: Test apparatus energy balance

Calculated wall heat flux (W/cm^2)	1.5	9.0	13.6	17.2	20.3
Electrical heat supplied (W/cm^2)	3.5	10.8	14.8	17.6	21.8
% Error	57.9	17.0	8.6	2.3	6.9

6.3 Temperature Measurements:

Temperatures at the wall-fluid interface (T_w) and the sapphire-adhesive interface ($T_{sapphire}$) for two locations are shown in Figure 33. At 9.0 W/cm^2, T_w changes rapidly in response to nucleation and bubble departure while $T_{sapphire}$ is relatively steady due to the thermal mass of the sapphire and its high thermal conductivity. At the heat flux (20.3 W/cm^2) large vapor patches can form and hover over the wall, so the local temperature of the sapphire surface can vary. Its effect upon the heat flux calculations depends on the difference between the interpolated temperature and the actual local

temperature on the sapphire surface. For a constant wall temperature, if the interpolated temperature is higher than the actual sapphire temperature, it would result in an underestimation of the calculated heat flux to the substrate. On the other hand, if the interpolated temperature is lower than the actual sapphire temperature, the local heat flux would be overestimated. In a recent study by Solotych et al [26], a 2-D numerical simulation was conducted in order to determine the minimum distance between the dots, such that the interpolation between the dots can capture the local temperature profile on the sapphire substrate. A 3 mm spacing was observed to be the optimum distance between the dots, which is the same distance utilized within the test section construction. In addition, the magnitude of the changes in T_w are several times larger than the temperature changes in $T_{sapphire}$, which results in a relatively low uncertainty in the heat flux measurement. Future pool boiling studies near CHF conditions could use transparent substrates with a higher thermal diffusivity (e.g., synthetic diamond), to further decrease substrate temperature variations.

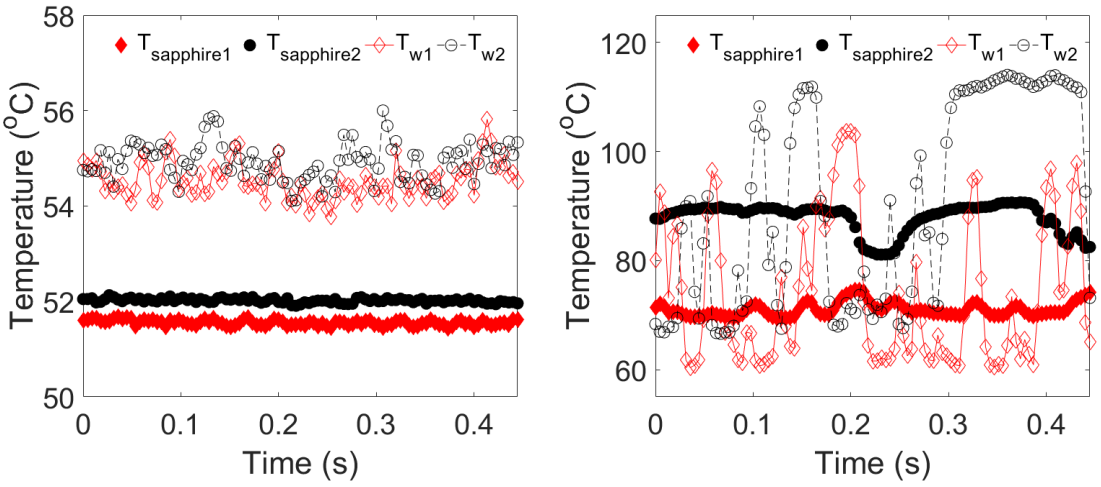

Figure 33: Wall temperature versus sapphire temperature, Left: nucleate boiling ($q"_w$=9.0 W/cm^2); Right: post-CHF condition ($q"_w$=20.3 W/cm^2)

6.4 Local Measurements:

Surface heat flux and the corresponding wall temperature distribution are shown on Figure 34. At the lowest heat flux (1.5 W/cm^2), the many small bright spots of higher heat flux are signatures of individual bubbles growing and departing from the surface. Bubbles cover nearly the entire surface by 9.0 W/cm^2. The first signs of bubble coalescence resulting in larger dry spots (darker, lower heat flux regions) occur at 14.8 W/cm^2 which corresponds to the change in slope in the boiling curve and to a wall temperature spike on the heater surface. The surface becomes increasingly covered by dry patches as CHF is reached at ~20.5 W/cm^2.

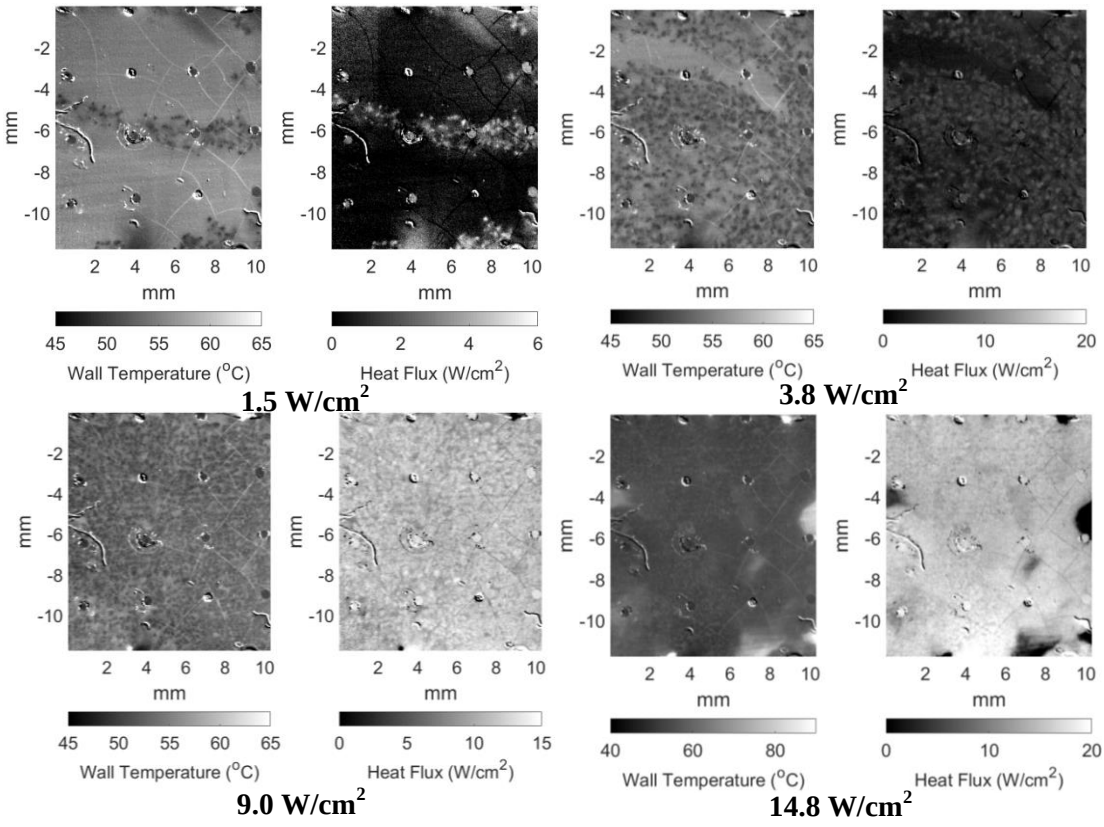

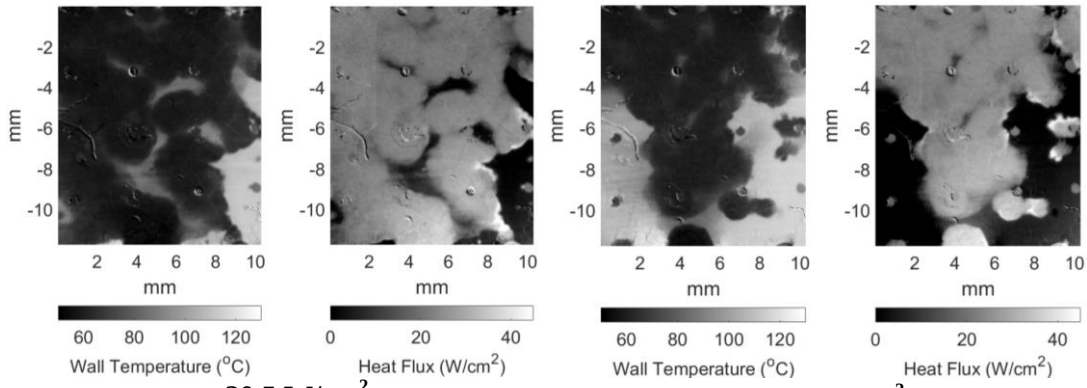

20.5 W/cm^2 **20.3 W/cm^2**

Figure 34: Wall temperature and surface heat flux distribution at various heat loads

6.5 Quantitative Analysis of Local Heat Transfer:

Figure 35 shows the percentage contribution from the various prominent heat transfer mechanism from the heater surface at various wall heat fluxes. As shown in the Figure 35, the main heat transfer contributor at wall-fluid interface is the surface quenching, via single phase transient heat conduction, where the contribution via the advancing and receding contact line sum to less than 5% of the total heat transfer allocation. This feature is further elaborated in Figures 36 and 37 pertaining to the surface heat transfer as liquid advances and recedes on the heater surface, beyond CHF. As liquid (light regions) recedes from the surface at locations indicated by the green arrows, a layer of liquid is left behind and the heat flux decreases as liquid superheats and evaporates, as indicated by the progressively darker shade. No evidence of high heat transfer at the three-phase contact line is seen. In contrast, the heat flux abruptly increases as liquid advances over and quenches the surface (location indicated by the red arrows) as indicated by the bright line of high heat flux. These observations are quite similar to what have been observed using IR thermography by Jung et al. [83].

A spike in the local heat flux corresponds to liquid advancing onto a dry surface, as shown in Figure 36. As liquids recedes, the wall heat flux decreases. This behavior has been observed by numerous researchers (e.g., Jung et al. [83], Kim et al. [111-112], Unal et al. [113]) and indicates transient heat conduction as the main mechanism of heat transfer near CHF. The TSP technique is much simpler to implement, however, since there is no emission of visible light from the sapphire and adhesive–detailed measurements of the spectral properties required for IR are not needed for TSP measurements, and absorption/reflection of light can be accounted for by in-situ calibration.

Another relevant observation in Figure 37 pertains to the formation of vapor patch formation in the vicinity of residual patch from previous mushroom bubble. Several studies, including Chu et al [114-115] and Choi [116], highlighted the role of partial coalescence between newly emerging bubbles and the departing mushroom bubbles, which was associated with incomplete surface wetting upon bubble departure. Such behavior brought about an increased nucleation site and activity, along with the local rise in the surface superheat. In the following sections, the characteristics of surface dryout will be analyzed in depth, which can bring about a better understanding of surface dryout phenomenon near CHF conditions.

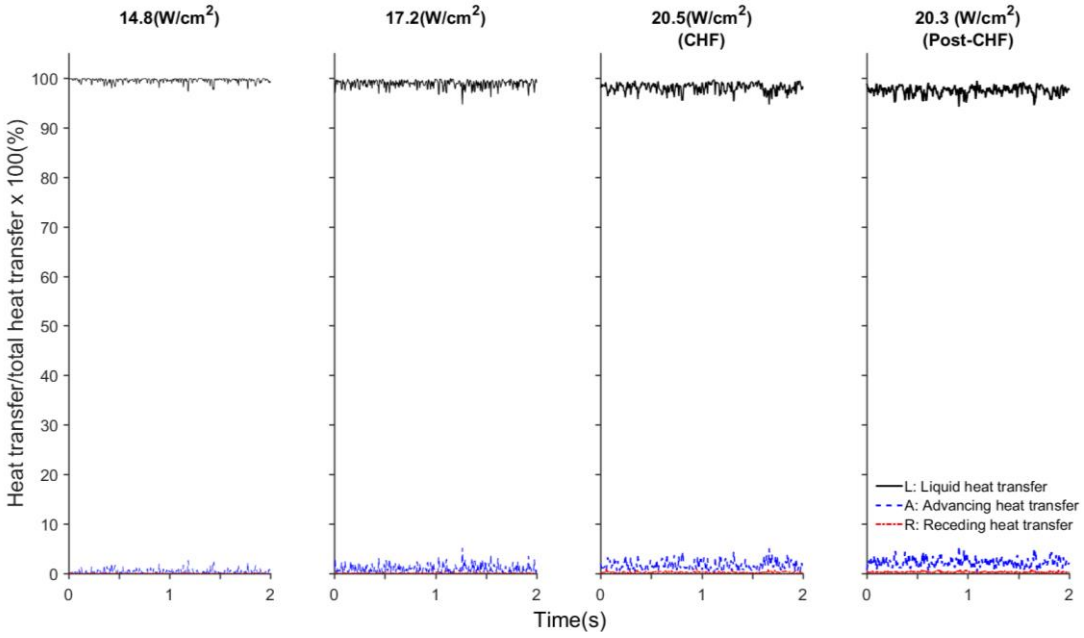

Figure 35: Various contribution to the surface heat flux

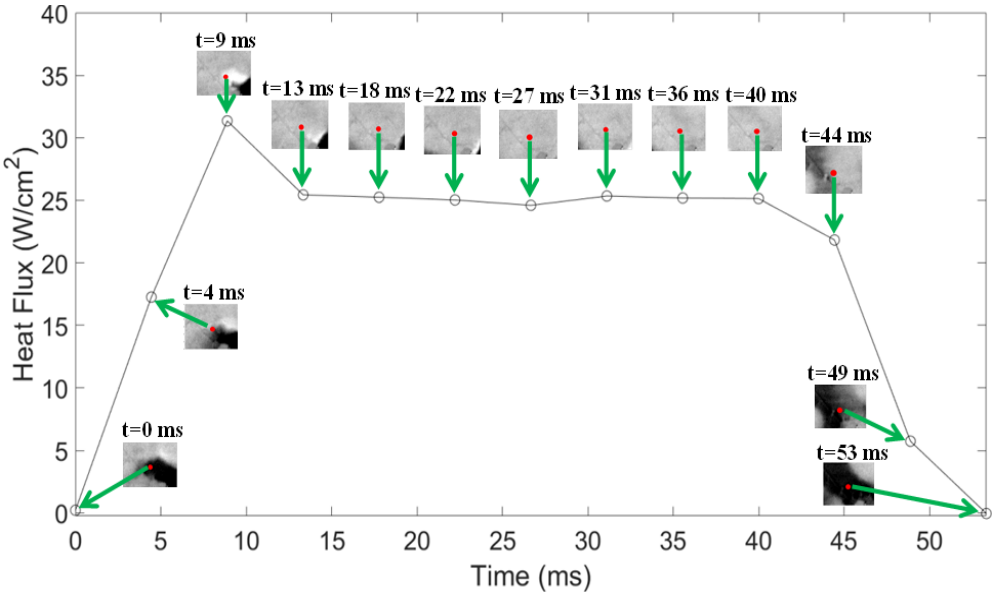

Figure 36: Heat flux evolution during advancing and receding of liquid on the surface (q''_w=20.3 W/cm^2)

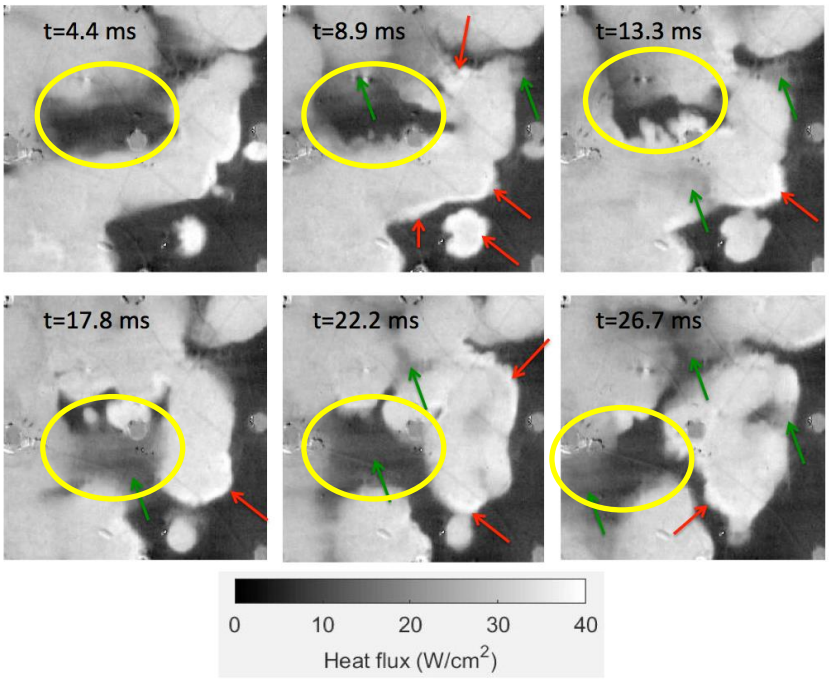

Figure 37: Heat flux distribution vs. time at a wall heat flux of 20.3 W/cm^2, as liquid advances (red arrows) and recedes (green arrows) on the surface. The field of view is approximately 6 mm x 6 mm.

6.6 Dryout features and characteristics

6.6.1 Contact Line Correlation with Wall Temperature and Surface Heat Flux:

The correlation between the various prominent factors affecting the surface heat transfer and the overall surface behavior was evaluated using a Pearson product-moment correlation coefficient [117]. Such a probabilistic approach was used to measure the dependency of the various variables, namely: the contact line density (CLD), wet fraction (WF), wall temperature (T_w), as well as the surface heat flux (q″). The Pearson product-moment correlation coefficient is defined by Equation 35, where a value of 1 or -1 indicates a direct or inverse linear relation among the examined variables. On the other hand, a Pearson correlation of zeros indicates an

independency among the examined variables. In Equation 35, X_i and Y_i represents the two examined variables, n is the sample size, and σ_X and σ_Y are the standard deviation of the corresponding variables.

$$\rho_{X,Y} = \frac{cov(X,Y)}{\sigma_X \sigma_Y} = \frac{\sum_{i=1}^{n} x_i y_i - n\bar{x}\bar{y}}{(N-1)\sigma_X \sigma_Y} = \begin{cases} -1 \leq \rho_{X,Y} \leq 1 \\ \rho_{X,Y} = 0 \end{cases} \quad (35)$$

Figure 38 shows plots of the sample data used in the correlation analysis, within the Pearson product-moment Equation, while Table 11 shows the result from the correlation analysis. Both the wall temperature and surface heat flux had a relatively stronger correlation with the surface wet fraction, compared to the contact line density. Such result is similar Jung et al. [83] conclusion from his correlation study of the FC-72 boiling data, which further support the role of the single phase transient heat conduction as the main mechanism of heat transfer.

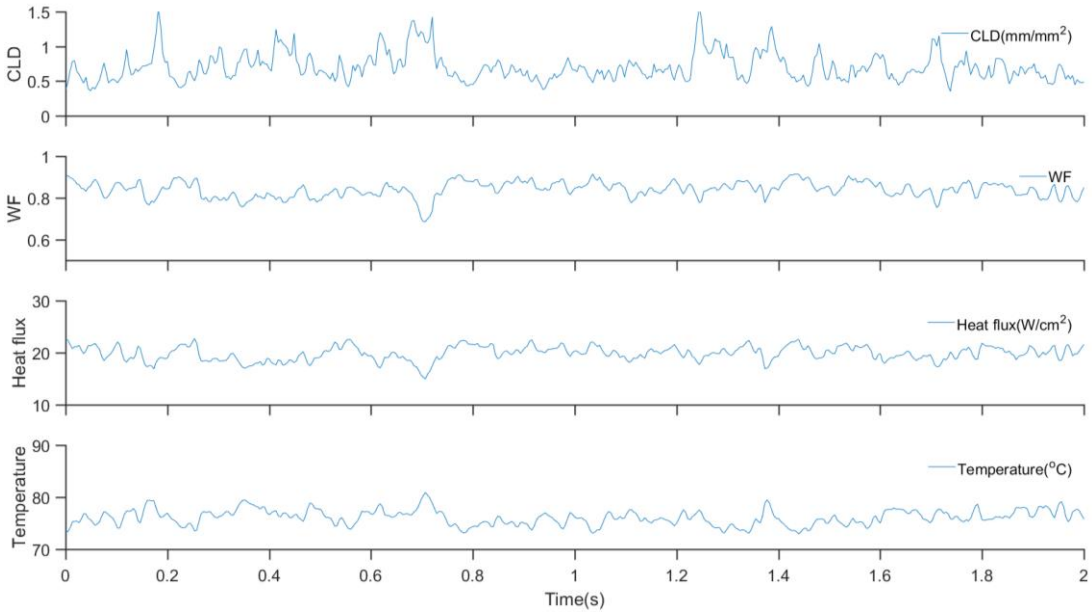

Figure 38: Evolution of contact line density (CLD), wet fraction (WF), heat flux, wall temperature with time ($q"_w$=20.3 W/cm^2)

Table 11: Pearson Coefficient (q''_w=20.3 W/cm^2)

	T_w versus q”	T_w versus WF	T_w versus CLD	q" versus WF	q” versus CLD	WF versus CLD
Correlation coefficient	-0.84	-0.84	+0.38	+0.82	-0.64	-0.48

6.6.2 Dryout Characterization

Figure 39 shows an illustration of the dryout function, which corresponds to temperature spikes upon vapor patch formation on the surface. Figure 40 shows dryout functions at various surface heat fluxes. As shown in Figure 40, both the frequency and the duration of the surface dryout increase with surface heat flux. Such behavior is more dominant towards CHF, while a more steady increase is observed at the lower heat fluxes. In Figure 41, the average frequency of vapor patch formation was plotted against the average duration of the surface dryout. Similar to the trend observed in Figure 40, a lower frequency of vapor patch formation is associated with a steadier vapor patch formation, while a sudden increase in the average duration of dryout is observed at a relatively higher heat flux. This can be explained in terms of force balance stability on a vapor bubble, based on the Hickman number, where a higher surface heat flux is associated with a rapid destabilization grow, hence a lower Hickman number. This might be an indication for a secondary mechanism of vapor patch formation, which facilitates a more rapid patch formation at higher heat fluxes. Hence, the prolonged appearance of vapor patches on the heater surface.

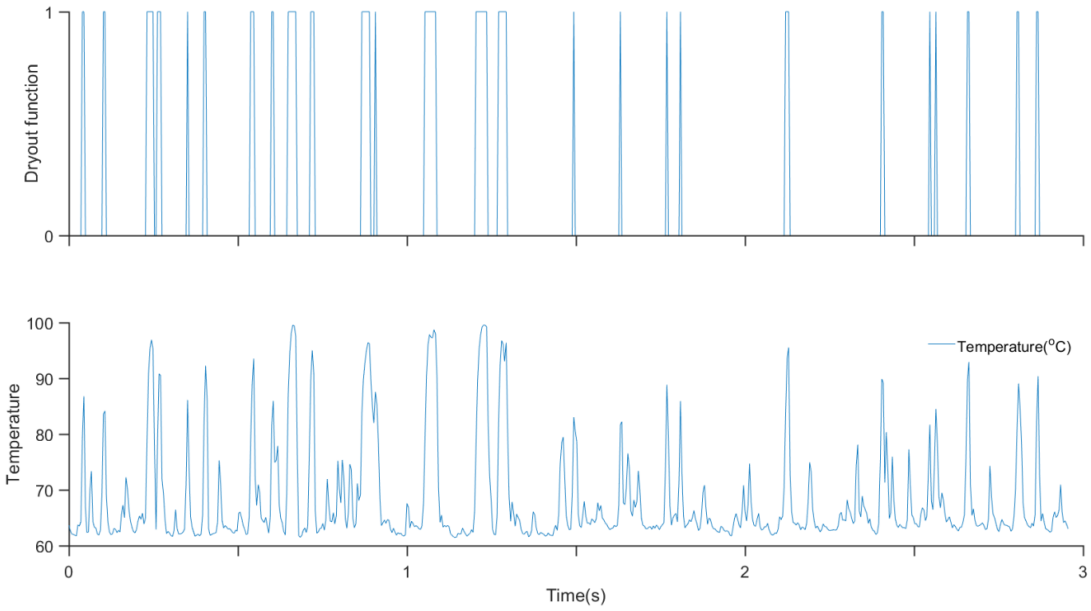

Figure 39: Evolution of wall temperature dryout function with time at center of the heater (q''_w=20.3 W/cm^2); 1: dry, 0: wet

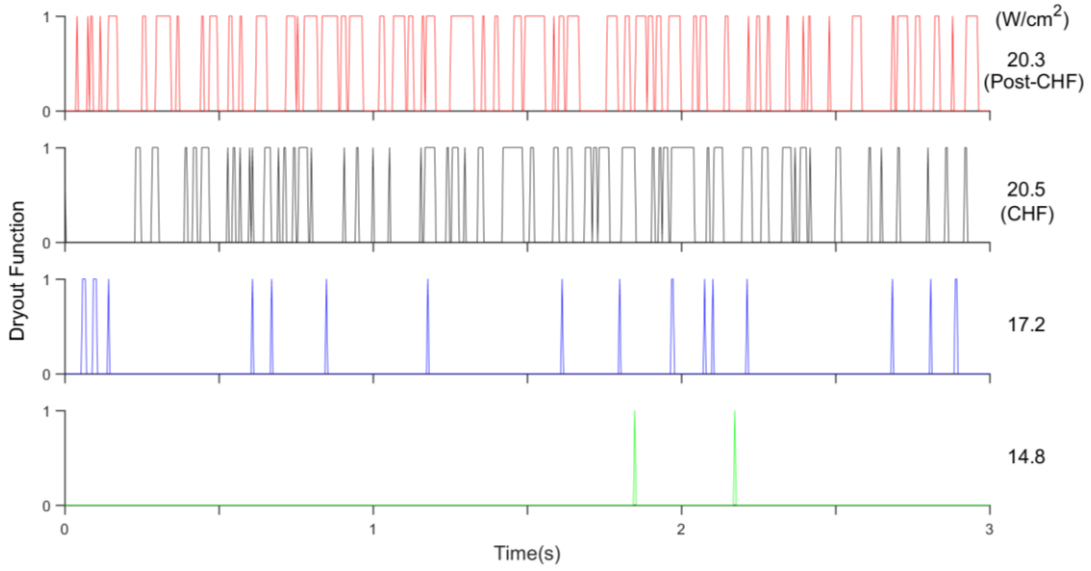

Figure 40: Evolution of dryout function with time at the center of the heater, for various surface heat fluxes

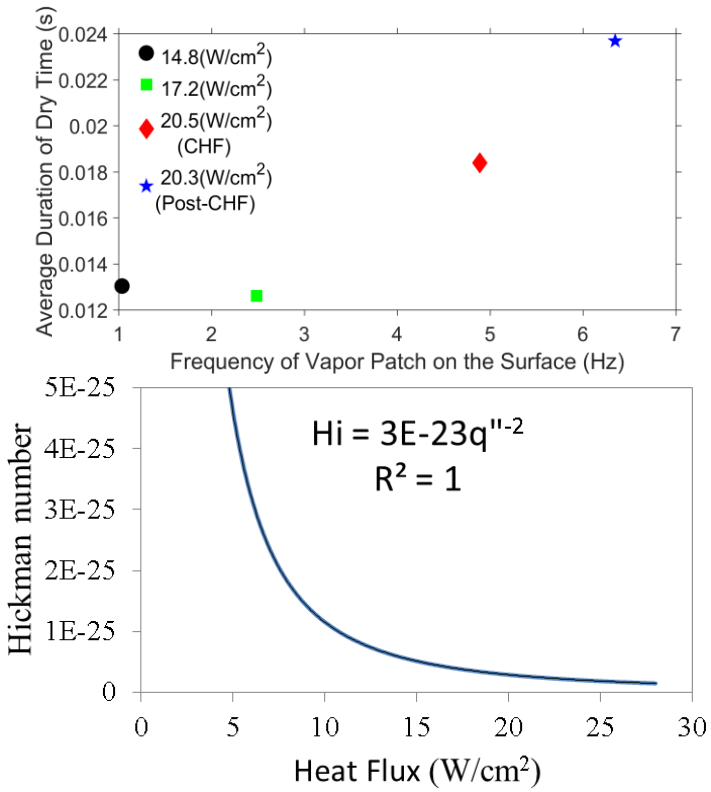

Figure 41: Average duration of dryout versus vapor patch appearance frequency on the surface (top) and the Hickman number (bottom), for various surface heat fluxes

Figure 42 plots both the contact line density and the wet fraction with time for various surface heat fluxes. The contact line density follows a similar trend to the to the vapor patch formation, where a sudden increase is observed towards CHF conditions. On the other hand, the observed drop in the surface wet fraction is less severe, which accounts for %10 of the total observed area. These results are similar to the ones obtained by Theofanous et al [103] near CHF conditions, which might imply that the CHF conditions are associated with the surface wetting property rather than the liquid supply to the surface. In addition, it can be seen from figure 42 that the contact line density increases beyond CHF, which indicates that the CHF is correlated

with contact line density. Such result is consistent with Jung et al [83] IR study, where CHF was not related to contact line heat transfer limitations.

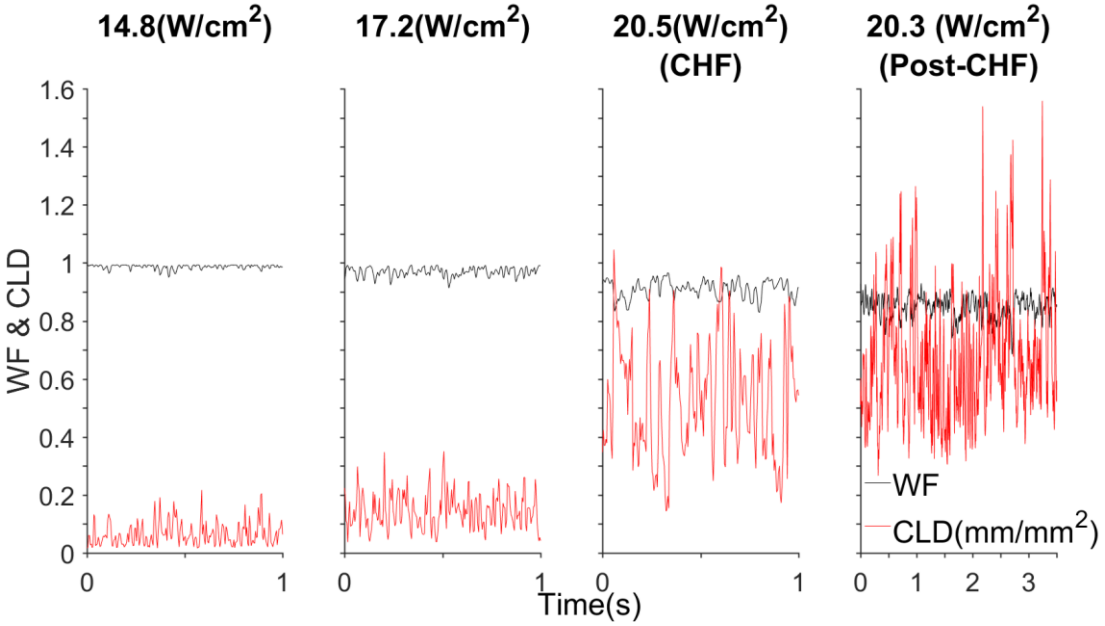

Figure 42: Evolution of WF and CLD with time for various surface heat fluxes

Figures 43 shows the advancing and receding area speeds at different vapor patch size, while Figure 44 show the statistics for the different vapor patch speeds occurrence. Several observations can be made from the Figures. First, both the receding and advancing area speeds are within the same magnitude for the various patch sizes. Second, the smaller vapor patches are more likely to occur, based on the occurrence statistics of the advancing/receding area speeds. The latter result is in consensus with Teodori et al [118-119] observations, where smaller vapor bubble generation was associated with fluids that induce larger bulk flow convection. Fluids such HFE7000 tend to have a lower surface tension relative to its density, which brings about a lower lateral bubble coalescence, according Teodori et al [118-119]. Such characteristics play an important role within the working fluid performance at

heat removal. For instance, Teodori et al [118-119] observed deterioration in the heat transfer performance for water relative to HFE7000, as a result of bubble lateral coalescence, due to the artificial surface cavities. On the contrary, the HFE7000 performance was enhanced by those artificial cavities, as it acted to stabilize the bubble ebullition at various heat fluxes. This conclusion was derived from Teodori et al [118-119] PIV measurements at different depths, where a higher surface tension of the water relative to its density favors bubble lateral coalescence. On the other hand, the relatively higher latent heat of water brought about an overall increase in heat transfer coefficient. Thus, in analyzing the working fluid performance, one should inspect the various heat transfer contribution that includes natural convection, latent heat, as well as the induced bulk flow convection. Figure 45 shows the variation of the advancing and receding area speeds with surface heat flux. In general, the advancing and receding area speed was observed to increase with heat flux, which is in agreement with Teodori et al [118-119] PIV observations.

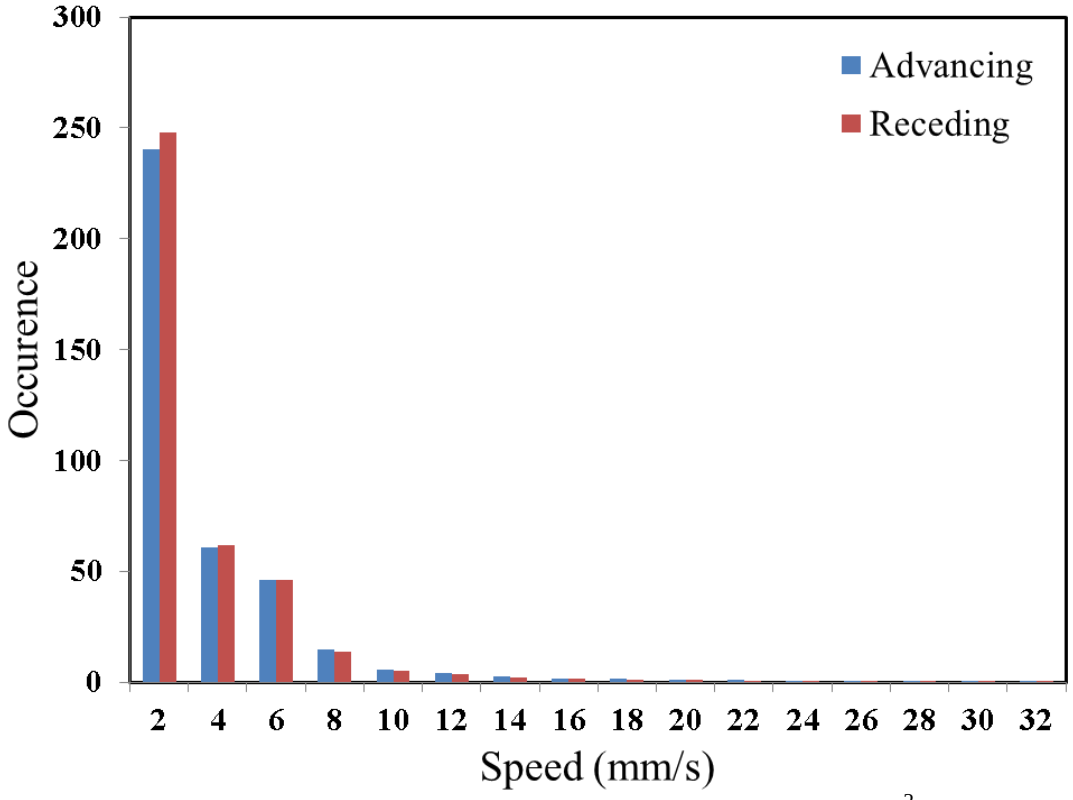

Figure 43: Contact line speed occurrence ($q"_w$=20.3 W/cm^2)

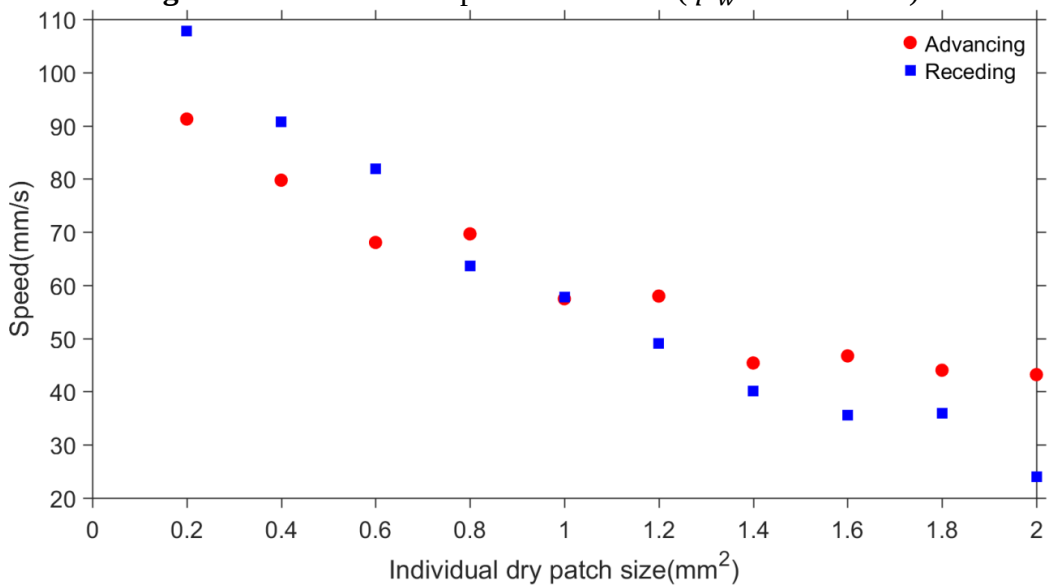

Figure 44: Contact line speed with respect to different dry patch size ($q"_w$=20.3 W/cm^2)

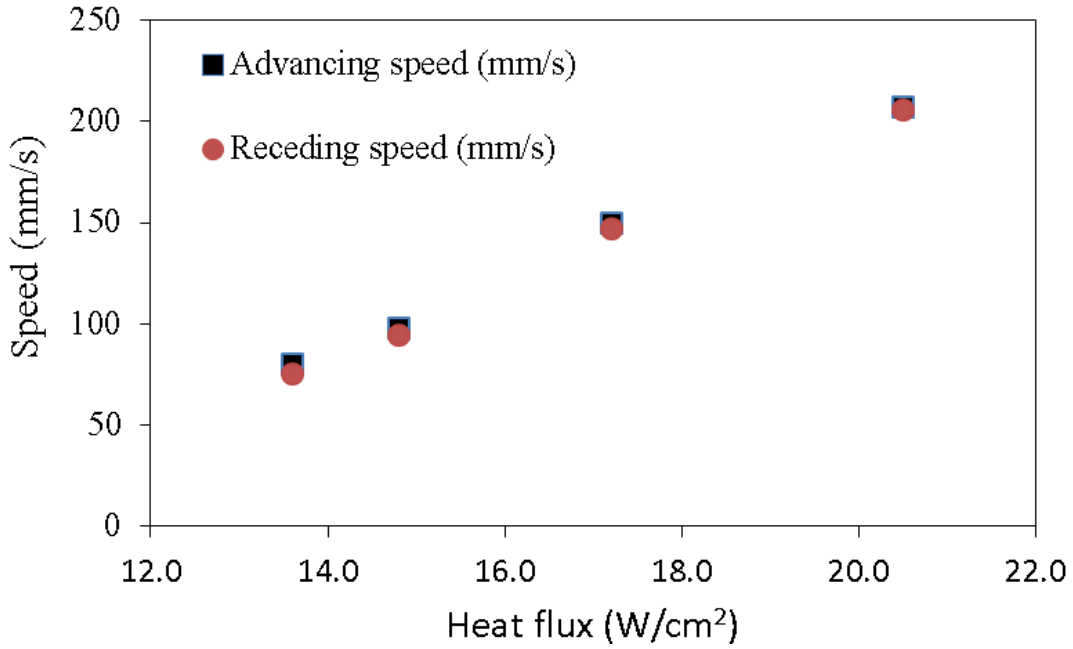

Figure 45: Contact line speed with respect to different surface heat fluxes

Figures 46 and 47 show the advancing and receding contact line length and the percentage covered from the heater surface. Similar to the contact line density trend in Figure 42, both the advancing and receding contact line length increases with heat flux. The same can be said with regards the percentage area occupied by the advancing and receding area. It can also be seen that the low percentage of advancing and receding heat transfer can be related to the low area percentage, as shown in Figure 47.

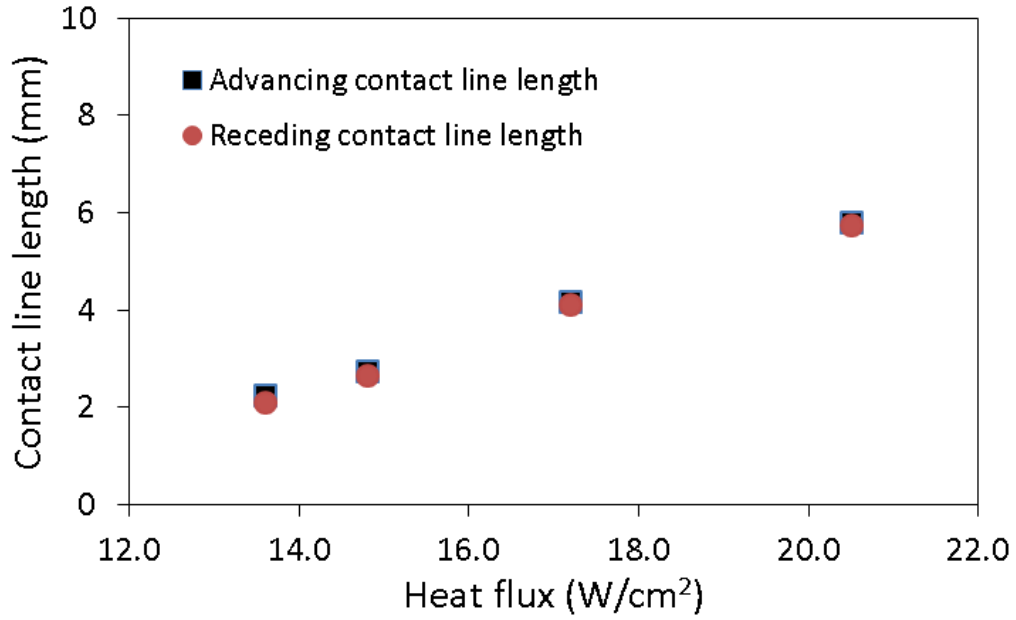

Figure 46: Contact line length with respect to different surface heat fluxes

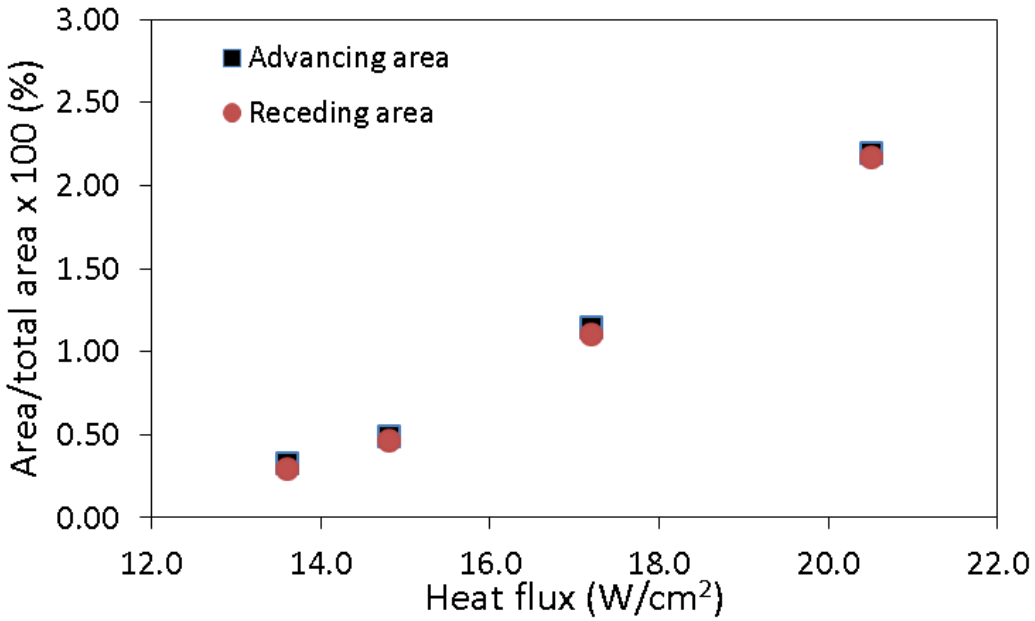

Figure 47: Advancing/receding area with respect to different surface heat fluxes

Figure 48 shows the vapor patch distribution at various surface heat fluxes. It can be readily seen that there is a shift towards larger vapor patch sizes at higher heat flux, which is similar to the frequency behavior observed in Figure 41. Recall the

incomplete wetting phenomenon shown in Figure 36 in which it is suspected to have increased the rate of large vapor mushroom formation. It coincides with the prolonged dryout phase at high heat fluxes, where the surface experience an increased rate of vapor mushroom formation, as shown in Figure 41. According to Chu et al [114-115], the CHF mechanism is based on the residual patch formation, where partial coalescence of the new formed bubbles with the departing mushroom bubble interfere with surface rewetting process. As a consequence, the surface is not completely rewetted upon bubble departure, and the residual dry patch brings about an increase in the mushroom bubble formation. This is achieved via local surface superheat increase with every cycle of the mushroom bubble formation, which brings about an increased nucleation site activity. Such interactions can lead to a thermal runaway, a phenomenon often associated with the heater burnout, as observed by Chu et al [114-115]. The increase in the mushroom bubble formation rate, via residual dry patches, might explain the increase in the dryout frequency, as well as the shift in the vapor patch distribution towards larger patch sizes at higher heat fluxes.

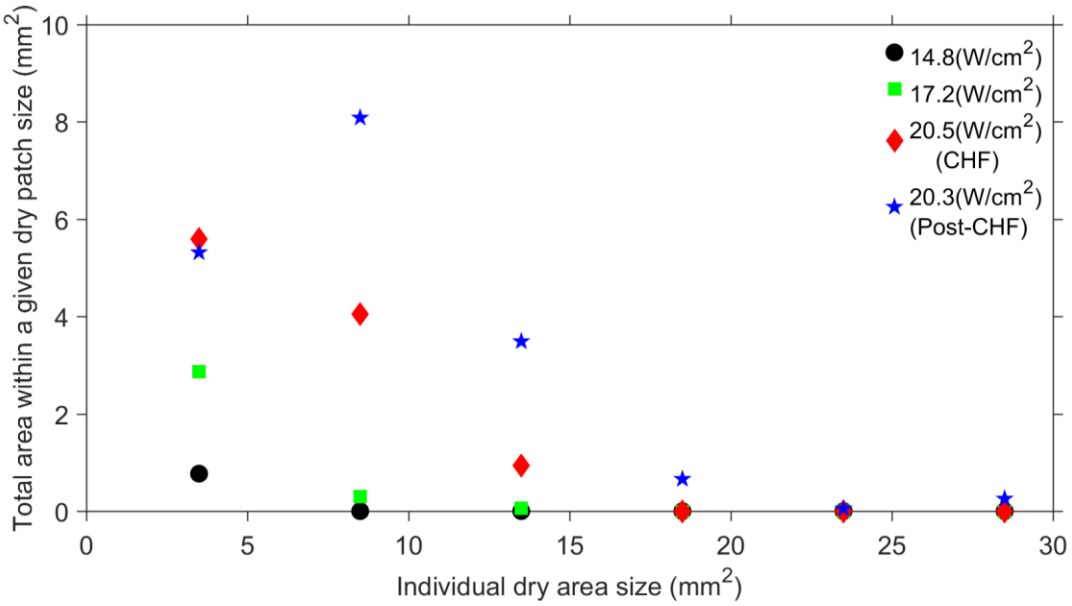

Figure 48: Dry patch distribution

7. Numerical Simulation of Pool Boiling

7.1 Introduction:

In a collaborative work with Dr. Miad Yazdani, the role of fluid motion within pool boiling application was examined within a CFD simulation study. The pool boiling curve acquired from the CFD study was compared with the experimental data, which was based on the wet area of the boiling surface. In addition, the velocity magnitude and the turbulence intensity were evaluated from the CFD data. The goal behind the CFD study was to correlate the fluid turbulence behavior near the wall with the observed surface heat flux. Thus, a complementary perspective can be built with respect to the surface dryout mechanism near CHF conditions.

7.2 Data Processing:

Both the wall temperature and the surface heat flux were computed over the wet area of the boiling surface. Determination of the wet regime within the simulated boiling surface is similar to the threshold function used in the experimental data processing. In practice, the liquid fraction data from the CFD study was used in order to determine the dry-wet zone, as shown in Figure 49.

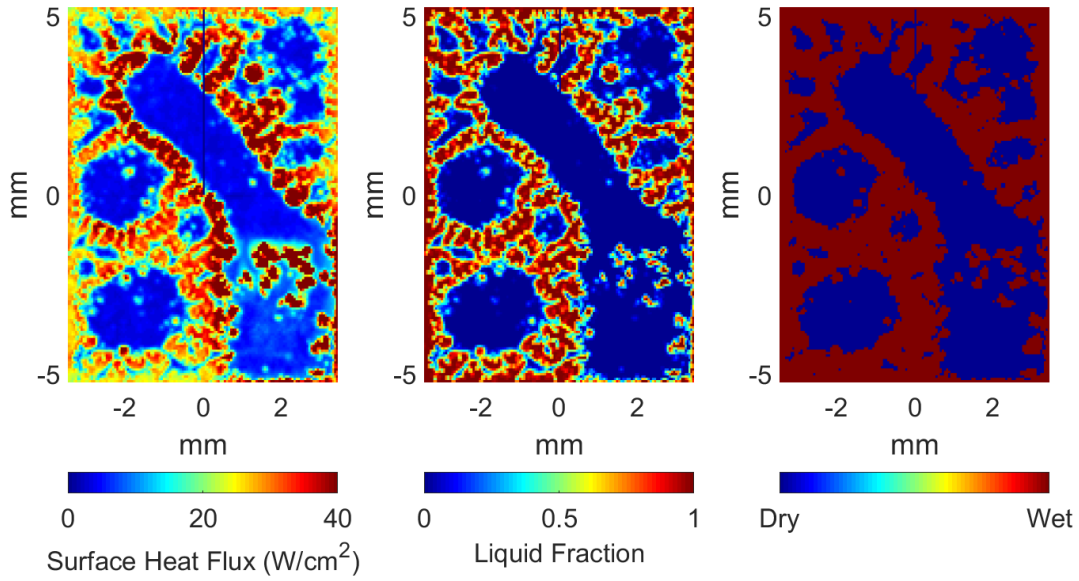

Figure 49: Simulation feature extraction based on liquid fraction. Data courtesy of Dr. Miad Yazdani.

7.3 Liquid Fraction and Vector Field Characteristics:

Figure 50 shows the liquid fraction distribution at different times, along with the fluid vector fields at two different surface heat fluxes. At 5.6 W/cm^2, isolated bubbles dominate the boiling surface, where complete surface rewetting is observed upon bubble release from the surface. At high heat fluxes, larger bubble formation is evident via coalescence, where the surface does not rewet completely upon the departure of the "mushroom like" bubble from the heated surface. Such behavior was observed in the pool boiling experiment, where newly formed vapor patches partially coalesce with neighboring patches of departing mushroom bubbles. Such phenomenon was attributed by Chu et al [114-115] to the eventual dry out of the heated surface.

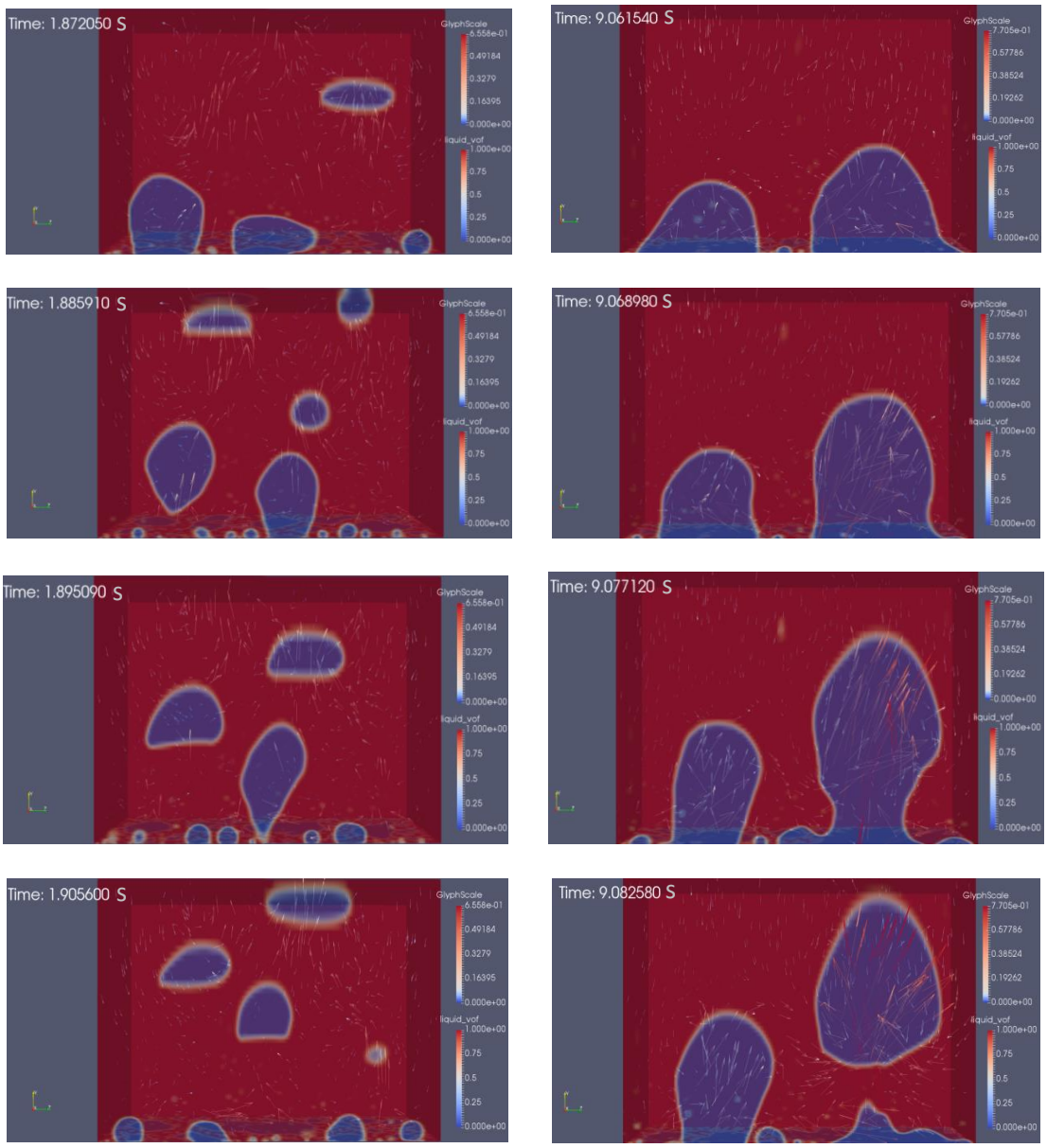

q"=5.6 W/cm^2 q"=20 W/cm^2

Figure 50: Liquid fraction and vector field visualization with time at different heat fluxes. Data courtesy of Dr. Miad Yazdani.

7.4 Turbulence and mean velocity profiles:

Figure 51 shows the velocity magnitude profile at different vertical distances from the heated wall surface, which was acquired by plane averaging the velocity magnitude at different cells. Only the liquid regime was used in the computation, which was specified using the liquid fraction data from the CFD study. As shown in Figure 51, the highest velocity magnitude was observed near the wall surface, where it rapidly decline towards the free surface away from the heater. Figures 52 and 53 show the turbulent intensity and the dissipation rate profile, as a function of the vertical distance from the heater, respectively. Both plots exhibit distinct features at different distances from the wall: Close to the wall, both the fluid turbulence intensity and the dissipation rate exhibit a maximum, which can be related to bubble detachment, as shown in figure 50. In a numerical work by filelal et al [120], the bubble detachment was associated with a velocity drift and a torque, where a high velocity gradient exists near the wall. The high velocity gradient corresponds to a sharp drop in the velocity magnitude close to the wall, as shown Figure 51. Thus, the local capillary flow induced from the bubble departure, also known as poiseuille flow, brings about the formation of local turbulence, due to the bubble ebullition. Further away from the wall, the bubble velocity approach terminal speed, where the local turbulence settles down and the turbulence dissipation rate approaches zeros. This can be related to the counter current observed in the vector fields on Figure 50, which stabilizes the bubble ascending towards the free surface. Both fluid velocity magnitude and turbulence increases with surface heat flux, which might be related to the reduced fluid viscosity with fluid temperature near the wall.

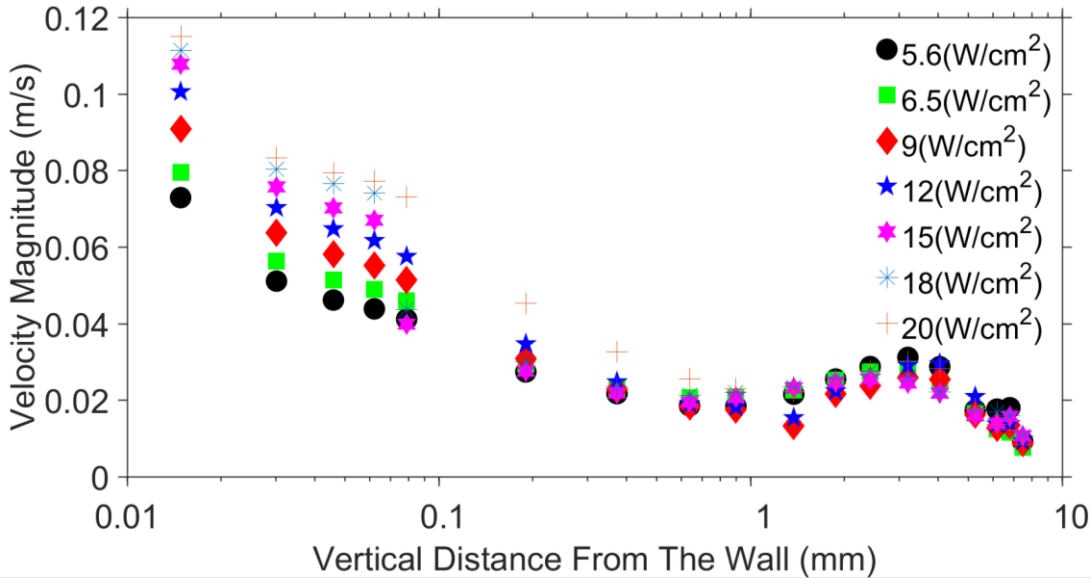

Figure 51: Fluid velocity magnitude profile. Data courtesy of Dr. Miad Yazdani.

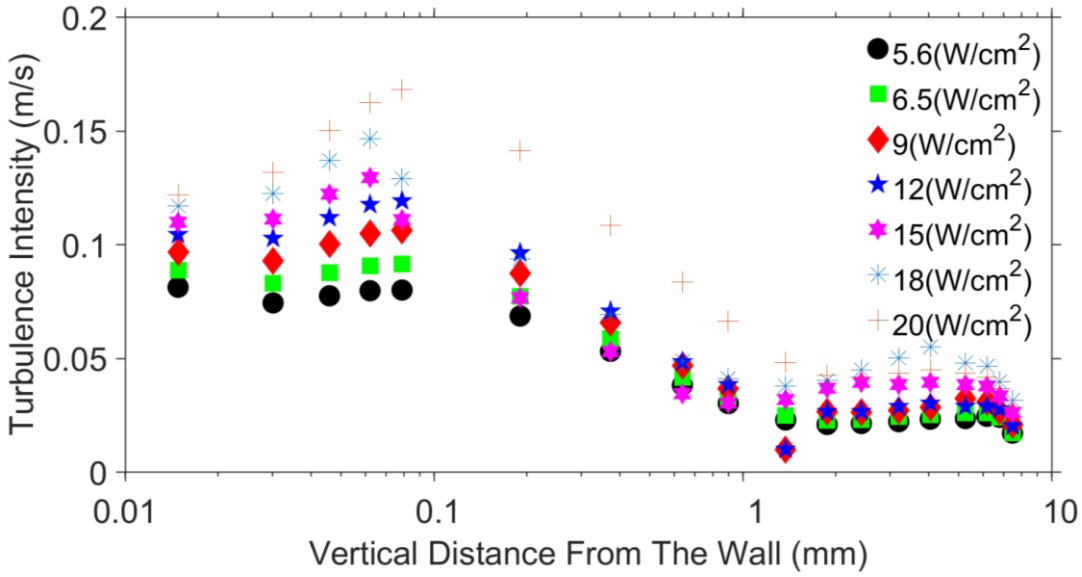

Figure 52: Fluid turbulence intensity profile. Data courtesy of Dr. Miad Yazdani.

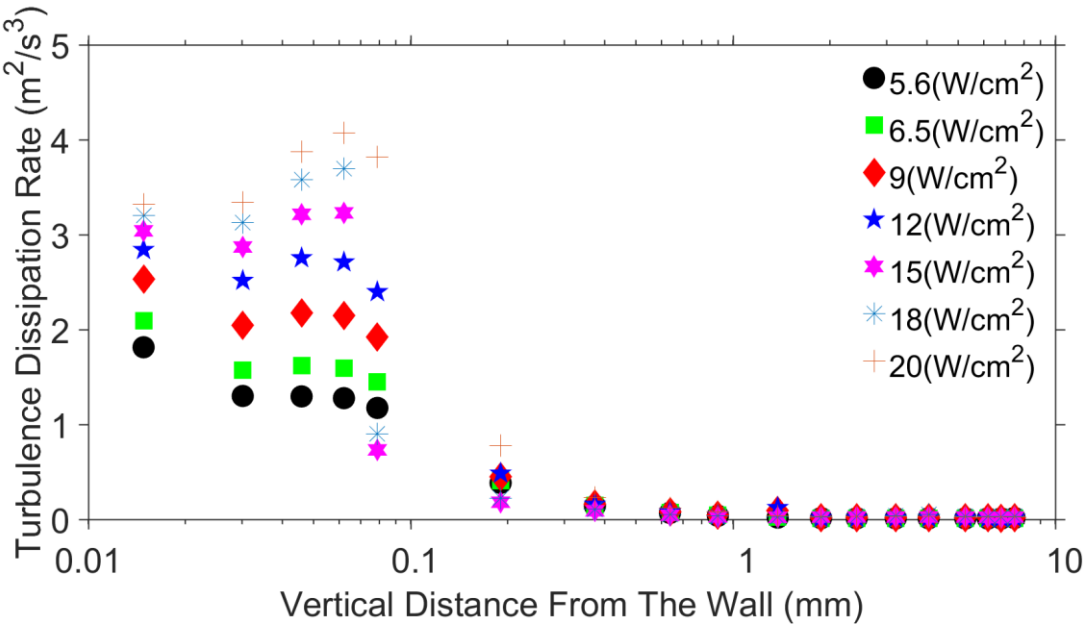

Figure 53: Fluid turbulence dissipation rate profile. Data courtesy of Dr. Miad Yazdani.

7.5 Turbulence Characterization with Surface Heat Flux:

Figure 54 shows the boiling curves acquired from both the experimental (Exp't) and simulation (Sim) studies, which was obtained from spatial and temporal averaging over the liquid area of the heated surface. As shown in Figure 54, a good match between the simulation data and the experimental data can be seen at the high heat flux ranges, which represents the fully developed nucleate boiling regime of the boiling curve. Within the fully developed nucleate boiling, the heat transfer by the fluid is very efficient such that the heat loss to substrate is minimal. On the other hand, the deviation of the experimental data from the simulation results at low heat fluxes can be justified by the experimental energy balance data, as shown in Table 10, where the observed heat losses of the supplied power contributed for the observed discrepancy on the boiling curves. Those heat losses are attributed to the NPT screw,

which is bonded to the sapphire substrate. Within the simulation model, the heat loss to the NPT screw was not accounted for, hence, an overestimation of the experimental heat flux was observed in the boiling curve, as shown in figure 54.

Also shown in Figure 54 is the turbulence intensity at various surface heat fluxes, which was computed from the CFD velocity field data. The turbulence intensity data used in Figure 54 was acquired by averaging over a horizontal plane, at a distance of 15 μm from the heated surface. Only the liquid regime of the fluid model was used in the turbulence intensity calculations, where the liquid fraction data was used to profile the liquid regime within the fluid model. As shown in Figure 54, the fluid turbulence intensity shows similar treads to the boiling curve: First, the turbulence intensity increases with the wall superheat, which is an indication of an increased fluid mixing near the wall at higher heat fluxes. The change in the turbulence intensity curve with the wall superheat is less severe than the experimental boiling curve trend, which might be related to unaccounted heat losses within the CFD model. With the increase in superheat, there is an indication that the slope of the turbulence intensity curve tends to reduce at higher super heat regime, which is similar to the experimental boiling curve at CHF condition. Such result corresponds to a reduction in the fluid velocity near CHF condition, which might imply a reduced wettability of the fluid near CHF.

Figure 55 shows the turbulent dissipation rate as a function of superheat, along with the boiling curves from both the experimental and simulation data. Similar to the turbulence intensity and the wall heat flux, the turbulence dissipation rate increases with the wall superheat, indicating an increase in the velocity great gradient

near the wall. The slope of the turbulence dissipation rate plot with the wall superheat decreases more severely at a higher superheat compared with both the fluid's turbulence intensity and velocity magnitude. On the other hand, the turbulence dissipation follows the trend of the experimental pool boiling curve, which might indicate a correlation between the velocity gradient and the heat flux near the wall surface. A direct implication of this result might be a reduction in the poiseuille's flow, which was described by Felillal et al [120] around the bubble in the form of capillary motion. Such result might explain the incomplete wetting of the dry surfaces upon mushroom bubble departure near CHF, where the bubble coalescence at higher heat flux restricts the capillary motion of the fluid around the bubble.

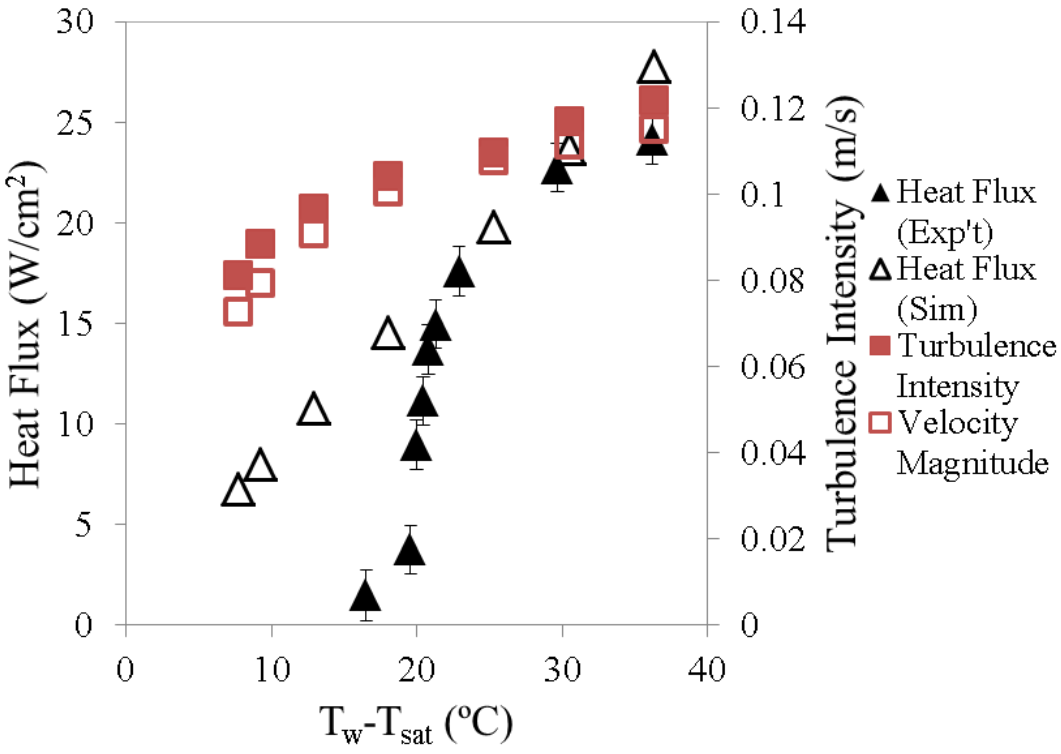

Figure 54: Turbulence intensity, velocity magnitude and surface heat flux versus wall superheat. Simulation data courtesy of Dr. Miad Yazdani.

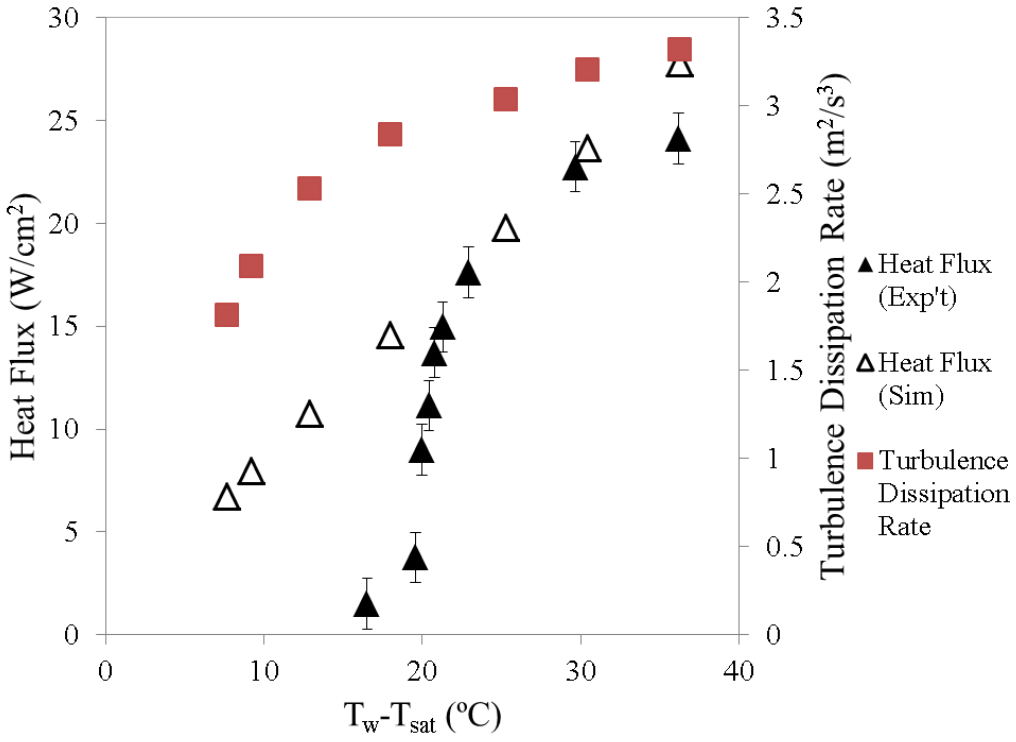

Figure 55: Turbulence dissipation and surface heat flux versus wall superheat. Simulation data courtesy of Dr. Miad Yazdani.

8. Summary and Future work

This dissertation revolved on the utilization of fluorescing material optical properties within phase change heat transfer application, which can be considered as a potential alternative to Infrared thermography due to its several advantages, including:

- Its ability to resolve smaller scale
- Cheap and readily applicable
- Overcomes substrate material limitations associated with its cost and transparency to the infrared wavelength.
- Limited by the camera performance

Other applications of the TSP include hypersonic wind tunnel measurements, cryogenics, and MEMS applications, such microjets and microturbines. The maximum temperature measurable by TSP is dependent on the luminophore compound used in the TSP formulation. In the current dissertation work, the maximum temperature detected by the Ruthenium complex compound (Ruthenium tris(1,10-phenanthroline) dichloride)) was around 120ºC. Other compounds such as $Yb_2Ti_2O_7$ with Er^{3+} and Mo^{3+} dopant was observed to have a maximum temperature of 336ºC; however, such compounds tend to have a lower temperature sensitivity relative to the Ruthenium based compound [121]. To the knowledge of the author, the highest reported heat flux using Ruthenium based compound was within high enthalpy shock tunnel applications in Germany Aerospace Center, which was around 125 W/cm^2 at the incident shockwave regime. In the vicinity of reflected shockwaves, heat fluxes as high as 700 W/cm^2 was reported within the shock tunnel applications [64].

Two different types of luminophores were used within the framework of the current dissertation, namely quantum dots and Ruthenium based TSP. Both materials work on the principal of thermal quenching, where the increase in the local temperature brings about a reduction in the emitted intensity of the fluorescing material. Such attribute was used to measure the local temperature profile of the target surface via calibration of the emitted fluorescence intensity.

In the ethanol drop evaporation experiment, the fluorescence of quantum dot was utilized for the local temperature measurement purposes, where a thin gelatin film was used as a carrier for the quantum dot. This preliminary study acted as qualifier test for the future usage of fluorescing material within phase change heat transfer application. The measurement technique involved depositing the quantum dot on the back of a heater, via a thin gelatin film. The experiment proved to be successful in the sense of capturing the relevant features of ethanol drop vaporization, observed by previous IR studies.

Ruthenium based TSP was used within pool boiling application instead of quantum dot, due to its lower cost higher sensitivity than QD. The Ruthenium based luminophore was applied as a temperature sensitive paint, where a heat flux measurement technique was developed within the framework of pool boiling experiment. TSP measurement technique was successfully validated for pool boiling heat transfer measurements via CHF correlations. On the other hand, camera noise was a big factor within the measurement uncertainty via TSP optical property. Transient heat conduction was observed to be the dominant heat transfer mechanism near CHF condition, a view supported by other IR studies. Analysis of vapor patch

distribution showed attributes associated with surface dryout near CHF condition, where there was a shift towards larger vapor patch sizes as the surface heat flux increased. Such vapor patches coincide with incomplete wetting of the larger vapor patch, which was associated with secondary mechanism of mushroom bubble formation. As consequence, there was a rapid increase in the dryout duration and local superheat at higher heat fluxes.

Pool boiling was modeled within a CFD study using HFE7000 properties, where the fluid turbulence near the heated wall was examined with respect to different surface heat flux. Both the fluid turbulence intensity and velocity magnitude increased with the wall superheat, which is similar to the wall heat flux within the pool boiling curve. The slope of the turbulence dissipation rate with the wall superheat was observed to decrease near CHF condition, which might imply a restriction upon the wetting fluid supply to the dry areas at higher heat fluxes.

Main contribution in the current dissertation is:

- Extension of the fluorescing material optical property usage from single phase to multiphase applications, where the measurement technique was verified within different phase change heat transfer application including:
  - The evaporation of ethanol drop via quantum dots
  - Pool boiling application, via Ruthenium based TSP
- Development of a temperature measurement technique for heat flux evaluation purposes, via 1D heat conduction problem, devised within pool boiling framework

- Explore the thermofluid aspect of surface dry out near CHF, via experimental measurement and a collaborative CFD work

Future pool boiling experiments can involve substrates with a higher thermal diffusivity property (eg. diamond), which would have the ability to smear out the excess heat at higher heat flux conditions. Thus, a more uniform temperature measurement can be acquired at the substrate surface, which would enhance the local heat flux measurement. In addition, alternative attachment techniques should be investigated in order to maintain the measurement integrity during the phase change heat transfer experiment. Such approach can help to mitigate the issues encountered within submerged jet boiling applications, where the optical measurement repeatability, and hence the temperature measurement, were affect by jet impingements at high temperatures. Future pool boiling study can have visual access to the boiling phenomena via:

- High speed camera from the fluid side
- Direct measurement via spectral means rather than emission intensity

Appendix A: Inverse Heat Conduction Problem Method

The surface heat flux evolving from the droplet vaporization was computed numerically from the acquired temperature measurements using an inverse heat conduction problem (IHCP) method. Such technique relies on determining unknowns within a system, where other independent variables at different nodes were used to reconstruct parameters or variables of interest [104]. Figure 56 shows a configuration model consisting of two computational regimes.

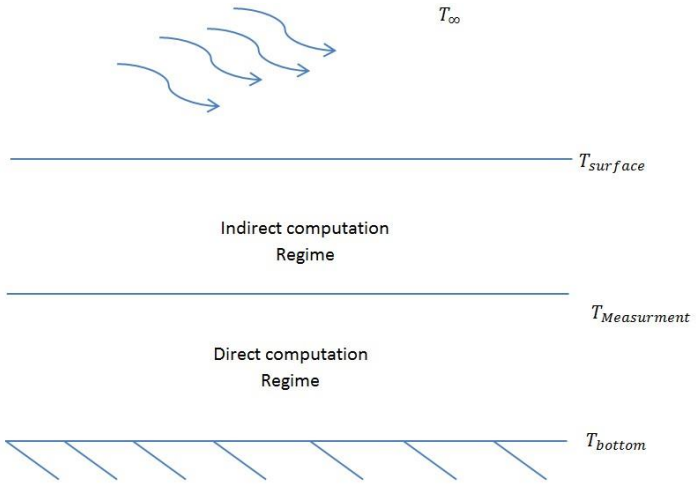

Figure 56: Configuration Model

Numerical solution involves solving the temperature distribution implicitly where the future temperature distribution is acquired from the current known temperature distributions. It also follows that implicit scheme is unconditional stable, where the spatial length scale (Δx) and the time step (Δt) are not restrained by any condition. Future temperature determination involves solving the nodal Equations simultaneously via matrix inversion methods. The energy balance for the internal nodes within the direct computational regime can be acquired by applying back

difference discretization scheme to the differential heat Equation. The heat Equation and its corresponding discretization are given by Equations 36 and 37, respectively.

$$k\frac{d^2T}{dx^2} + \dot{q'''} = \rho c_p \frac{dT}{dt} \tag{36}$$

$$k\frac{T_{N+1}^{t+1} - T_N^{t+1}}{\Delta x} + k\frac{T_{N-1}^{t+1} - T_N^{t+1}}{\Delta x} + \dot{q'''}\Delta x = \rho c_p \Delta x \frac{T_N^{t+1} - T_N^t}{\Delta t} \tag{37}$$

Recognizing the Fourier number (F_o) in Equation 38, Equation 37 can be rewritten in the dimensionless form and it's given by Equation 39.

$$F_o = \frac{k\Delta t}{\rho c_p \Delta x^2} \tag{38}$$

$$F_o T_{N-1}^{t+1} - (2F_o + 1)T_N^{t+1} + F_o T_{N+1}^{t+1} = T_N^t - \frac{\dot{q'''}\Delta t}{\rho c_p} \tag{39}$$

Within the indirect computational regime, the energy balance for the internal nodes can be acquired in terms of previous nodes. For a given interface temperature ($T_{Measurement}$) in Figure 56, the first node within indirect computational regime is found from the surface energy balance in Equation 40 where a quasi-steady state condition is assumed.

$$k_2 \frac{T_M^{t+1} - T_N^{t+1}}{\Delta x} + \dot{q''} = 0 \tag{40}$$

$\dot{q''}$ in Equation 40 is the heat flux from the first regime given by Equation 41. Equation 39 can be rearranged into Equation 42.

$$\dot{q''} = k_1 \frac{T_{N-1}^{t+1} - T_N^{t+1}}{\Delta x} \tag{41}$$

$$T_M^{t+1} = \left(1 + \frac{k_1}{k_2}\right) T_N^{t+1} - \frac{k_1}{k_2} T_{N-1}^{t+1} \tag{42}$$

The other nodes within the indirect computation regime can be found using Equation 43.

$$T_{M+1}^{t+1} = \frac{1}{F_o}\left(T_M^t - \frac{q''' \Delta t}{\rho c_p} - F_o T_{M-1}^{t+1} + (2F_o + 1) T_M^{t+1}\right) \tag{43}$$

The surface heat flux can be found from the surface energy balance given by Equation 44.

$$\dot{q}'' = -k_2 \frac{T_{M-1}^{t+1} - T_M^{t+1}}{\Delta x} \tag{44}$$

Appendix B: Thermal Property Characterization

The relevant thermal properties of the 25 μm optically clear acrylic adhesive were characterized in two different studies, due to their importance in the wall temperature evaluation and surface heat flux calculations. The density of the acrylic adhesive is a well-defined property, and thus, was omitted from the material characterization studies.

A.1 Thermal Conductivity

Figure 57 shows a schematic of the heat conduction instrument (H112A from PA hilton), which was used in the determination of the thermal conductivity of the optically clear acrylic adhesive (8146-2 from 3M). The linear heat conduction instrument comprises of two brass elements with a cross-sections of 25mm. The top brass section (hot section) was electrically heated via a power supply, while the bottom brass section (cold section) was cooled via a water chiller (from Thermo Scientific). The adhesive sample was 50 microns thick, which was laminated on the hot section interface. Thermal grease was applied upon the cold section interface in order to reduce the contact resistance, which was later pressed against the other surface of the acrylic adhesive sample. Temperature measurements across both brass sections were acquired via K-type thermocouples at 6 locations that are equally spaced. Data acquisition hardware (from national instrument) was used for real-time data-acquisition purposes, where LABVIEW software was used as an interface system control.

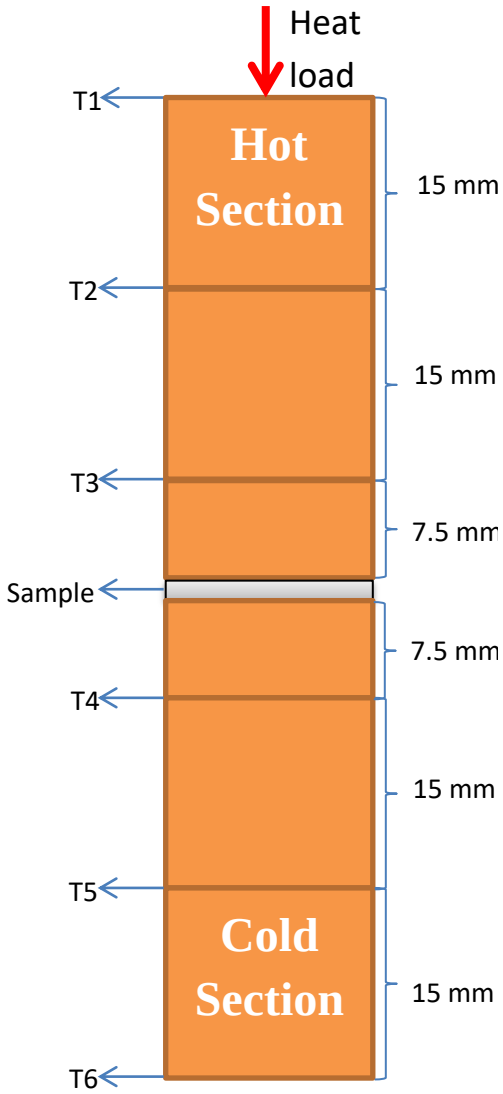

Figure 57: Linear heat conduction instrument

Determination of the acrylic adhesive thermal conductivity involves finding the heat flux flowing through the sample, using the temperature gradient across the brass sections. In practice, the thermocouple measurements were used to determine the heat transfer rate across both brass sections, via application of the Fourier law of heat conduction, given by Equation 45.

$$\dot{q} = kA\frac{dT}{dx} \sim kA\frac{\Delta T}{\mathrm{L}} \tag{45}$$

With the knowledge of heat transfer rate along with the thermocouple temperature measurements, the temperature difference across the sample can be extrapolated from which the sample's thermal conductivity can be calculated. Figure 58 shows a plot of the temperature distribution acquired from both the thermocouple measurements and via extrapolation, where both distributions show a good agreement. Values of the measured and the extrapolated temperature distributions are provided in Table 12. The acquired thermal conductivity, shown as an insert within Figure 58, is a good match to the value provided in the literature, which is around 0.19W/m-K. The thermocouples temperature measurement uncertainty was 0.2ºC.

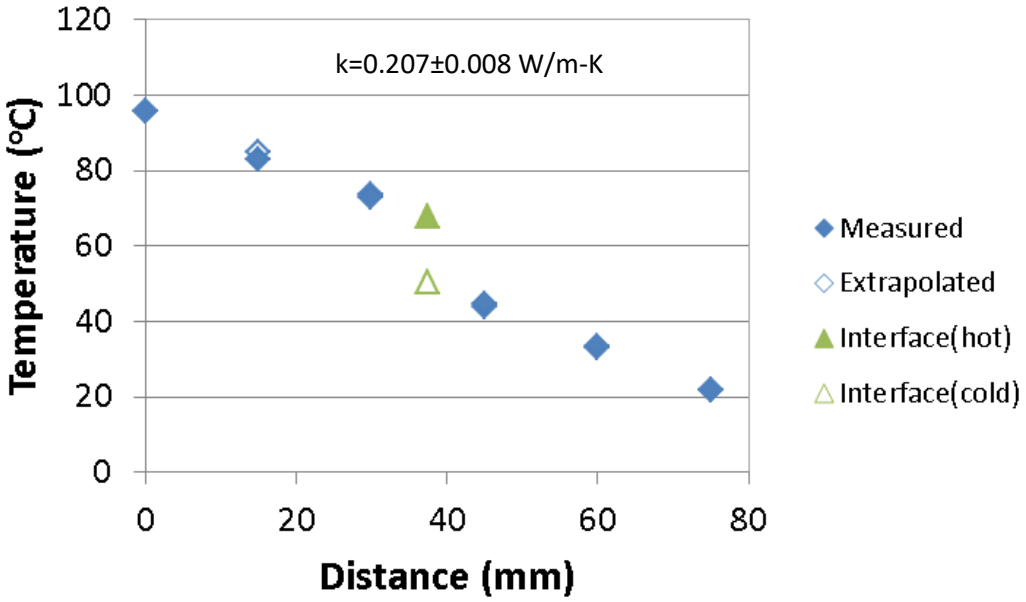

Figure 58: Temperature distribution across the brass sections

Table 12: Measured and extrapolated temperature distributions

Distance (mm)	Measured (°C)	Extrapolated (°C)
0	95.9	95.9
15	83.1	84.7
30	73.0	73.6
37.5		**67.9**
37.55		**50.2**
45	44.7	44.0
60	33.5	32.8
75	21.7	21.7

*Red: hot brass section interface; blue: cold brass section interface

A.2 Specific Heat Capacity

Transient temperature measurement was conducted via TSP fluorescing materials, so as to quantify the heat capacity property of the optically adhesive. The intensity of the fluorescing materials were captured via a monochromic camera at a framerate of 240 Hz (FL3-U3-13S2M-CS from point grey), so as to accommate for the fast temperature transition in response to the applied heat load. The TSP measurements were taken at two depths that are separated by 500 µm of acrylic adhesive (a composite of several layers of 8146-1 and 8146-2 acrylic adhesives from 3M), where a nichrome heater (TCR metal sheet from Ticer technologies) was attached at the top of the upper TSP layer, via a 5 µm acrylic adhesive (82600 electronic double sided tape from 3M). Prior to the transient temperature measurement, the TSP intensity was calibrated against a temperature range spanning 15ºC upto 70ºC, where a 5^{th} order polynomial fitting was used to generate a temperature conversion model for the TSP intensity. Further details of the apparatus and test procedures, used in the transient temperature measurments, can be found in previous sections.

Figure 59 shows the schematics of the simulation model used in the numerical simulation, which consists of a heat flux boundary condition, applied as a step change on top of the 5 µm double sided tape underneath the heater. Since the voltage across the heater was not a true step function, the voltage across the heater was also measured and the heat flux computed assuming a constant heater resistance.

The other boundary condition consists of the measured temperature data (TSP2) at a distanace of 505 µm from the heater. The purpose behind the numerical simulation is to pinpoint the acrylic adhesive heat capacity property that would yield a temperature distribution similar to the measured data at a distance of 5 µm from the heater (TSP1). The numerical simulation was solved as a 1D transient problem, where the data measurements used in the numerical analysis was spatially averaged for noise reduction, and hence, a lower measurement uncertainty was achieved. The thermal conductivity property, utilized in the numerical analysis, was acquired from the previous linear heat conduction analysis, while the density property was obtained from the literature, as it is a well quantified attribute. The properties of the PET carrier, of the 5 µm double sided tape, was omitted from the numerical analysis, as it is only 1 µm thick.

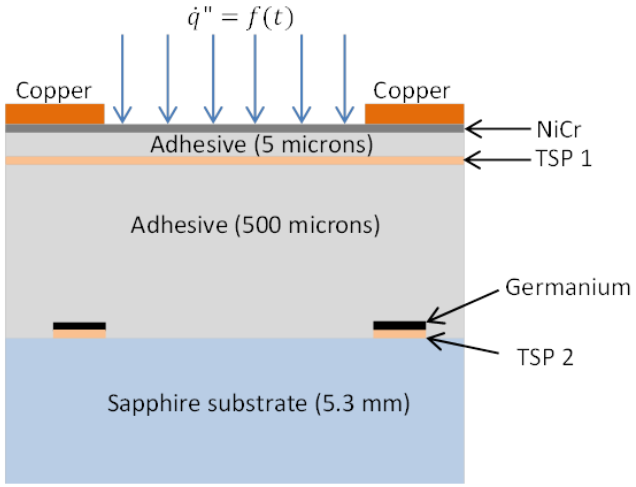

Figure 59: Schematic of simulation model

Figure 60 shows both the numerical and the measured temperature data (TSP1) at a depth of 5 µm, underneath the heater, along with the measured temperature boundary condition at a depth of 505 µm (TSP2) from the heater. The specific heat capacity was varied until model results indicated good agreement with the temperature measured at TSP 1 (Figure 60). Best agreement was found for a specific heat of 1800 J/kg-K. The uncertainty in specific heat affects only the unsteady data. An example of its impact is shown on Figure 61, where two values of specific heat were used to compute the wall heat flux during pool boiling near CHF. Somewhat larger spikes in heat flux are seen for the larger specific heat, but the effect is small. The impact on the pool boiling curve was negligible.

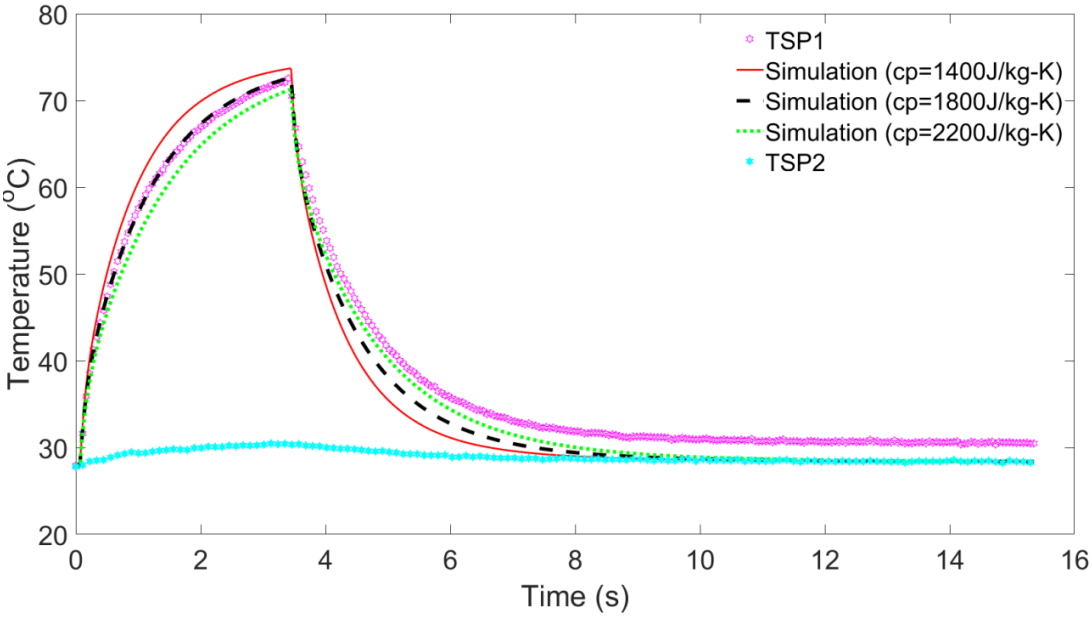

Figure 60: Numerical and measurement results

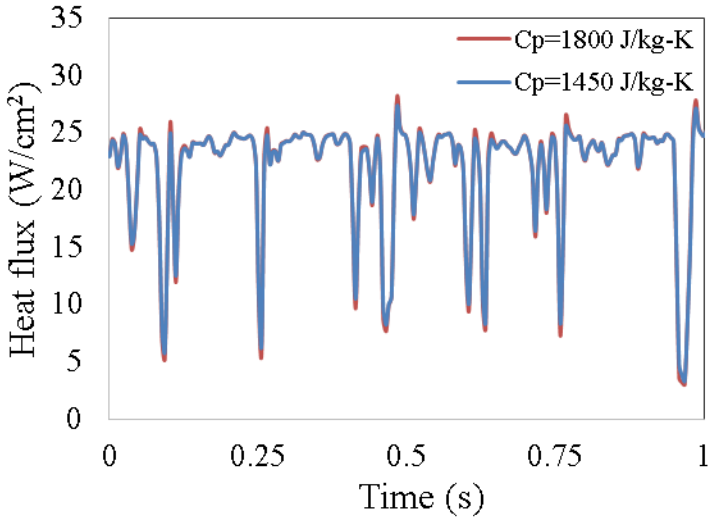

Figure 61: Evolution of wall heat flux with time for different heat capacity values

Appendix C: Pool boiling chamber drawing

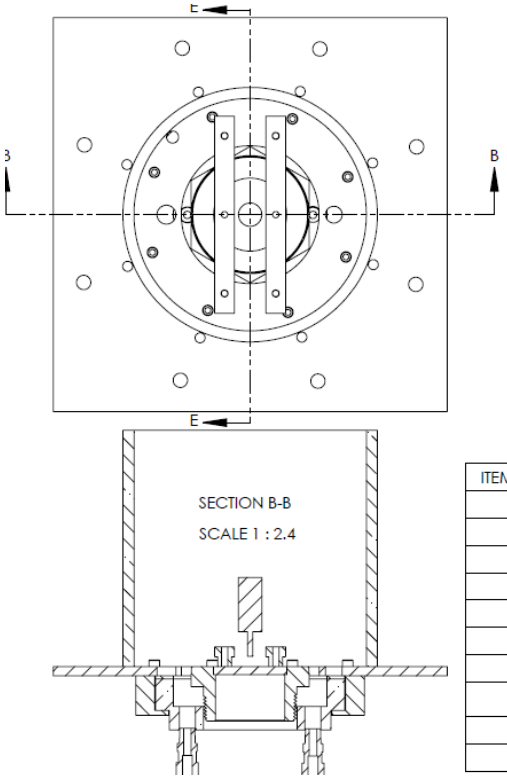

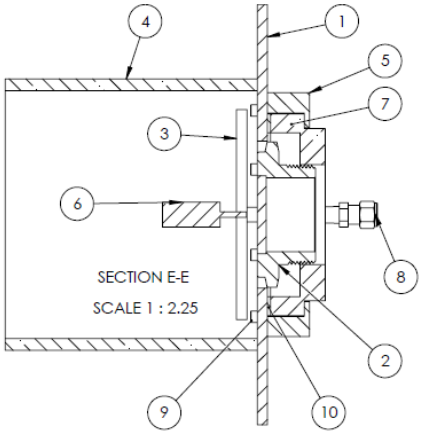

ITEM NO.	PART NUMBER	DESCRIPTION	QTY.
1	Base plate	Aluminu	1
2	NPT part	Steel	1
3	Electrodes	Plastic	1
4	Chamber	Aluminum	1
5	Nut holder	Aluminum	1
6	Jet nozzle	Copper	1
7	NPT Nut	Aluminum	1
8	MALE CONNECTOR-0.250Tx0.125 NPT	Steel	2
9	cap screw	Steel	8
10	Gasket	Rubber	1

Figure 62: Pool boiling chamber drawing

Appendix D: TSP measurement characteristic

The Figures below show the temperature measurement accuracy, which is taken as the difference between the calibration model and the temperature measurement during the calibration procedure prior the experiment. The calibration curves for the temperature measurement underneath the wall, as well as the sapphire surface, are also provided in the following Figures.

A.1 Temperature Measurement Accuracy

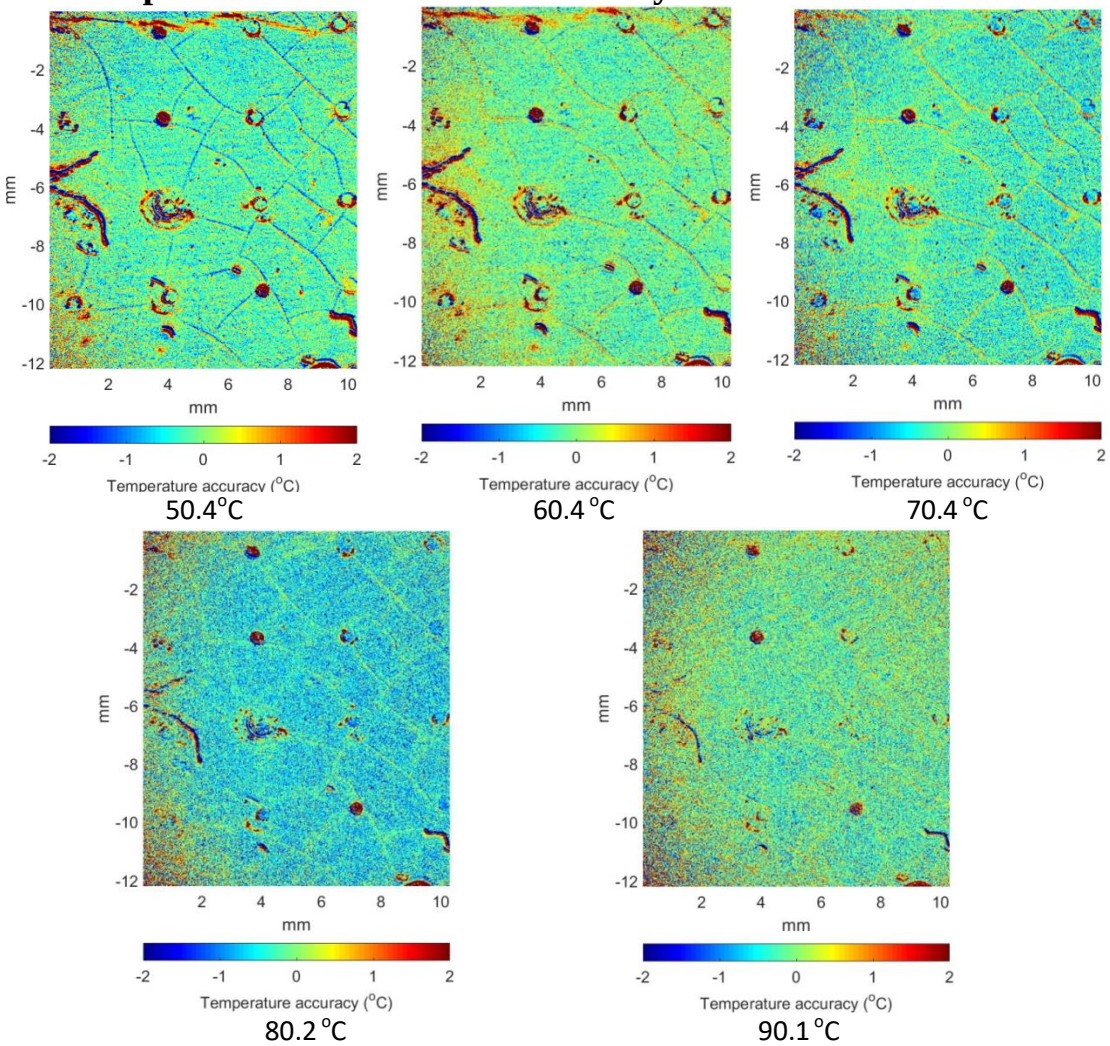

Figure 63: Measurement accuracy

A.2 TSP calibration curves

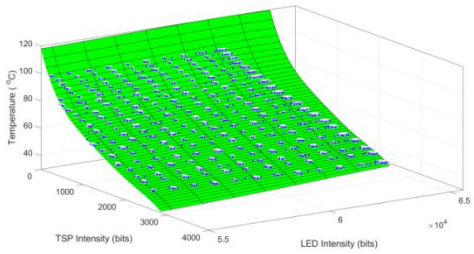

X=9.1 mm, y=-3.8 mm

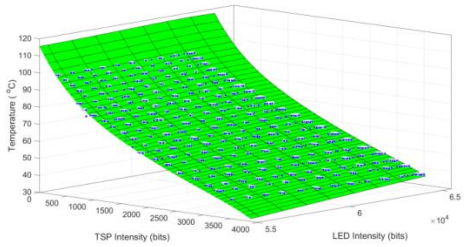

X=4.5 mm, y=-7.1

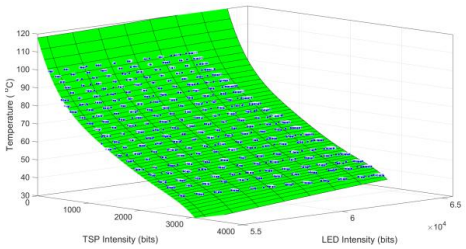

X=9.1 mm, y=-7.1 mm

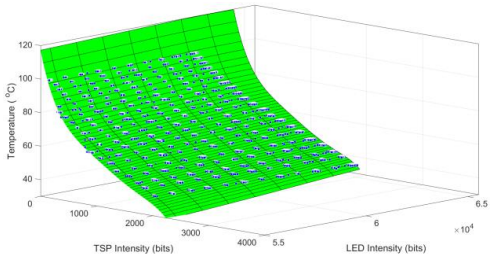

X=14.2 mm, y=-7.1 mm

Figure 64: TSP calibration

A.3 TSP dots calibration curves

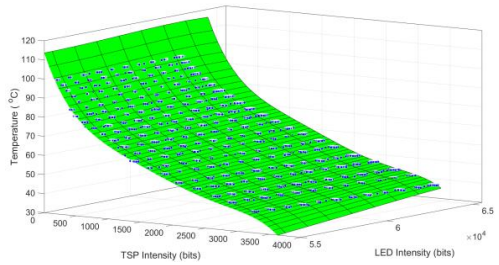

X=9.8 mm, y=-5.3 mm

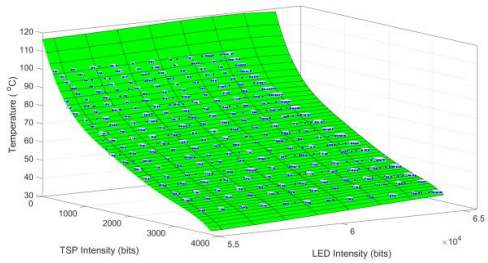

X=13.0 mm, y=-8.2 mm

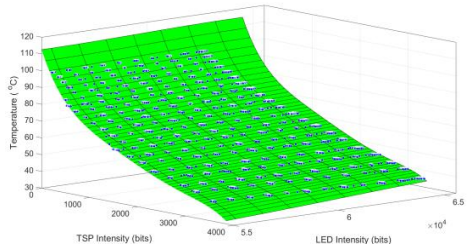

X=10.0 mm, y=-8.3 mm

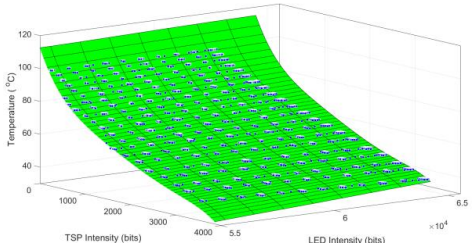

X=7.1 mm, y=-8.5 mm

Figure 65: TSP dots calibration

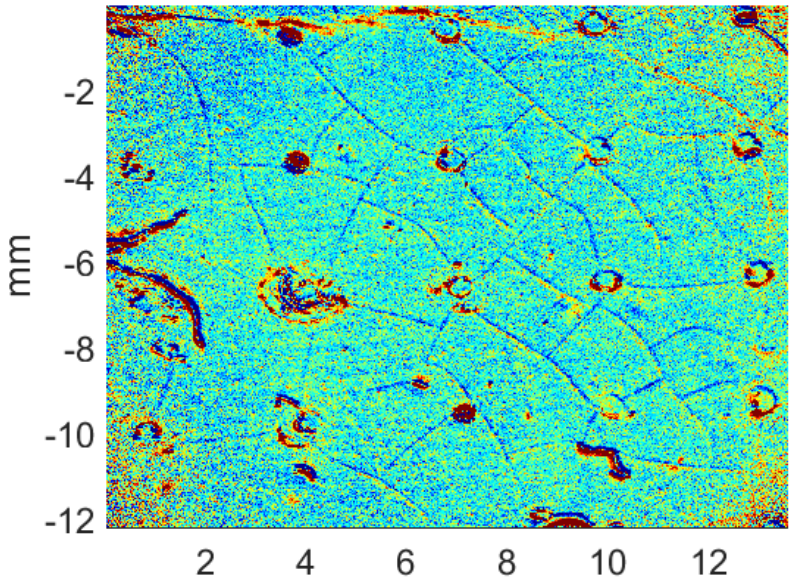

Figure 66: Reference Figure

References

[1] Luke, A. and Cheng, D., 2006, “High speed video recording of bubble formation with pool boiling,” International Journal of Thermal Science, **45**, pp. 310-320, doi:10.1016/j.ijthermalsci.2005.06.011.

[2] Bang, I. C., Chang, S. H., and Baek, W., 2005, ”Visualization of a principle mechanism of critical heat flux in pool boiling,” International Journal of Heat and Mass Transfer, **48**, pp. 5371-5385, doi:10.1016/j.ijheatmasstransfer.2005.07.006.

[3] Zhao, Y., Masuoka, T., and Tsuruta, T., 2002, “Theoretical studies on transient pool boiling based on microlayer model,” International Journal of Heat and Mass Transfer, **45**, pp. 4325-4331.

[4] Das, A. K., Das, P., K., and Saha, P., 2006, “Heat transfer during pool boiling based on evaporation from micro and macrolayer,” International Journal of Heat and Mass Transfer, **49**, pp. 3487-3499, doi:10.1016/j.ijheatmasstransfer.2006.02.050.

[5] Sobac, A. and Brutin, D., 2010,” HEAT TRANSFER AND FLOW INSTABILITIES IN ETHANOL SESSILE DROPS UNDER EVAPORATION,” *Proceedings of the 14th International Heat Transfer Conference*, Washington, DC, USA, ASME Paper No. IHTC14-22185.

[6] Chu, H., and Yu, B., 2009, “A new comprehensive model for nucleate pool boiling heat transfer of pure liquid at low to high heat fluxes including CHF,” International Journal of Heat and Mass Transfer, **52**, pp. 4203-4210, doi:10.1016/j.ijheatmasstransfer.2009.04.010.

[7] Narumanchi, S., Troshko, A., Bharathan, D., and Hassani, V., 2008, "Numerical simulations of nucleate boiling in impinging jets: Applications in power electronics cooling," International Journal of Heat and Mass Transfer, **51**, pp. 1-12, doi:10.1016/j.ijheatmasstransfer.2007.05.026.

[8] Pezo, M. and Stevanovic, V., 2011, "Numerical prediction of critical heat flux in pool boiling with the two-fluid model," International Journal of Heat and Mass Transfer, **54**, pp. 3296-3303, doi:10.1016/j.ijheatmasstransfer.2011.03.057.

[9] Theofanous, T. G., Tu, J. P., Dinh, A. T., and Dinh, T. N., 2002, "The boiling crisis phenomenon Part I: nucleation and nucleate boiling heat transfer," Experimental Thermal and Fluid Science, **26**, pp. 775-792

[10] Kim, T. H., Kommer, E., Dessiatoun, S., and Kim, J., 2012, "Measurement of two-phase flow and heat transfer parameters using infrared thermometry," International Journal of Multiphase Flow, **40**, pp. 56-67, doi:10.1016/j.ijmultiphaseflow.2011.11.012.

[11] Truong, E., 2013, "Cryogenic Single-Phase Heat Transfer in a Microscale Pin Fin Heat Sink," BS. Thesis, OSU, USA.

[12] Chen, Q., Luo, X., Zhou, S., and Liu, S., 2011, "Dynamic junction temperature measurement for high power light emitting diodes," review of scientific instruments, **82**.

[13] Kaltsas, G., Petropoulos, A., Tsougeni, K., Pagonis, D. N., Speliotis, T., Gogolides, E., and Nassiopoulou, A. G., 2007, "A novel microfabrication technology on organic substrates – Application to a thermal flow sensor," Journal of Physics: Conference Series, **92**, Doi: 10.1088/1742-6596/92/1/012046.

[14] Abad, E., Mazzolai, B., Juarros, A., Mondini, A., Krenkow, A., and Becker, T., 2010, "Fabrication and Encapsulation Processes," Radio Frequency Identification Fundamentals and Applications, Design Methods and Solutions, pp. 237-251, ISBN: 978-953-7619-72-5.

[16] Lee, G., Huang, F., Lee, C., and Miau, J., 2004, "A New Fabrication Process for a Flexible Skin with Temperature Sensor Array and Its Application," ACTA Mechanica Sinica, **20(**2), ISSN: 0567-7718.

[17] Lee, G., Wu, J., and Miau, J., 2002, "A New Fabrication Process for a Flexible Skin with Temperature Sensor Array," Journal of the Chinese Institute of Engineers, **25(**6), pp. 619-625.

[18] Yusoff, A., Syahrul, M., and Henkel, K., 2007, "Film adhesion in amorphous silicon solar cells," Bull Mater. Sci., **30**(4), pp. 329-331.

[19] *Nickel as a Coating Material*, 2011, Materion Brush Performance Alloys: Technical Tidbits, (34)

[20] Guereca, G. R, 2007, "Explosive vaporization in microenclosures and boiling phenomena on submicron thin film strip heaters," DScTech, Universidad Carlos III de Madrid, Spain.

[21] Xiao, S., Che, L., Li, X., and Wang, Y., 2007, "A cost-effective flexible MEMS technique for temperature sensing," Microelectronics Journal, **38**, pp. 360-364, Doi: 10.1016/j.mejo.2007.01.022.

[22] Chia, B. T., Chang, D., Liao, H., Yang, Y., Shih, W., Chang, F., Fan, K., 2007, "Temperature Sensor Array Using Flexible Substrate," MEMS, pp. 589-592.

[23] Petropoulos, A., Goustouridis, D., Speliotes, T., and Kaltsas, G., 2009, "Demonstration of a New Technology Which Allows Direct Sensor Integration on Flexible Substrates," The European Physical Journal Applied Physics, **46**(1),
Doi: 10.1051/epjap/2009020.

[24] Siegel, J., Lyutakov, O., Rybka, V., Kolska, Z., and Svorcik, V., 2011, "Properties of gold nanostructures sputtered on glass," Nanoscale Research Letters, **6(**96), doi:10.1186/1556-276X-6-96.

[25] Scammell, A. and Kim, J, 2015, "Heat transfer and flow characteristics of rising Taylor bubbles," International Journal of Heat and Mass Transfer, **89**, pp. 379-389, http://dx.doi.org/10.1016/j.ijheatmasstransfer.2015.05.068

[26] Solotych, V., Kim, J., and Dessiatoun, S. V., 2014, "LOCAL HEAT TRANSFER MEASUREMENTS WITHIN A REPRESENTATIVE PLATE HEAT EXCHANGER GEOMETRY USING INFRARED (IR) THERMOGRAPHY," Journal of Enhanced Heat Transfer, **21**(4-5), pp. 353-372, DOI: 10.1615/JEnhHeatTransf.2015012408

[27] Thompson, J. C, 2015, "A STUDY ON CRITICAL HEAT FLUX MECHANISMS AND THE TRANSITION TO FILM BOILING," MS. Thesis, UMD, College Park, USA.

[28] Lorenz, M., Horbach, T., Schulz, A., Bauer, J., 2013, "A Novel Measuring Technique Utilizing Temperature Sensitive Paint-Measurement Procedure, Validation, Application, and Comparison With Infrared Thermography," Journal of Turbomachinery, **135**, DOI: 10.1115/1.4006638

[29] Kenning, D. B. R., 1992, "Wall temperature patterns in nucleate boiling," International Journal of Heat Mass Transfer, 35(1), pp. 73-86, Pergamon Press plc, Great Britain

[30] Farina, D. J., 1995, "Making surface temperature measurements using liquid crystal thermography," Test & Measurement, Electronic-Cooling, available at: http://www.electronics-cooling.com/1995/10/making-surface-temperature-measurements-using-liquid-crystal-thermography/

[31] Azar, K. and Benson, J. R., 1991, "Liquid Crystal Imaging for Temperature Measurement of Electronic Devices," *Seventh IEEE SEMI-THERMTM Symposium*, pp. 23-33.

[32] Lou, J., Hatton, T. A., Laibinis, P. E., 1997, "Fluorescent Probes for Monitoring Temperature in Organic Solvents," Analytical Chemistry, **69**(6), pp. 1262-1264, American Chemical Society.

[33] Angell, J. J., 2011, "SYNTHESIS AND CHARACTERIZATION OF CDSE-ZNS CORE-SHELL QUANTUM DOTS," MS. Thesis, California Polytechnic State University, USA.

[34] Matsuda, Y., Torimoto, T., Kameya, T., Kameyama, T., Kuwabata, S., Yamaguchi, H., and Niimi, T., 2013, "ZnS–AgInS2 nanoparticles as a temperature sensor," Sensors and Actuators B: Chemical, **176**, pp. 505-508.

[35] Gui, C., Wang, K., Li, C., Dai, X., and Cui, D., 2014, "A CCD-based reader combined with CdS quantum dot-labeled lateral flow strips for ultrasensitive quantitative detection of CagA," Nanoscale Research Letters, Springer open Journal.

[36] Jorge, P. A. S., Mayeh, M., Benrashid, R., Caldas, P., Santos, J., L., and Farahi, F., 2006, "Quantum dots as self-referenced optical fibre temperature probes for luminescent chemical sensors," Measurement Science and Technology, **17**, pp. 1032-1038, Institute of Physics Publishing, doi:10.1088/0957-0233/17/5/S16

[37] Sakaue, H., Aikawa, A., Iijima, Y., Kuriki, T., and Miyazaki, T., 2012, "Quantum Dots as Global Temperature Measurements," *Quantum Dots – A variety of New Applications*, pp. 137-152, Intech, A. Al-Ahmadi, eds, ISBN: 978-953-51-0483-4, available from: http://www.intechopen.com/books/quantum-dots-a-variety-of-new-applications/quantum- dots-for-global-temperature-measurements, Chap. 7.

[38] Murray, C., Kagan, C., and Bawendi, M., 2000, "Synthesis and Characterization of Monodisperse Nanocrystals and Close-Packed Nanocrystal Assemblies," Annual Review Material Science, **30**, pp. 545-610, available from: http://www.annualreviews.org/doi/abs/10.1146/annurev.matsci.30.1.545.

[39] Baskoutas, S. and Terzis, A., 2006, "Size-dependent band gap of colloidal quantum dots," Journal of Applied Physics, **99**, available from: http://scitation.aip.org/content/aip/journal/jap/99/1/10.1063/1.2158502.

[40] Bueno, A., Suarez, I., Abargues, R., Sales, S., and Pastor, J. P. M., 2012, "Temperature Sensor Based on Colloidal Quantum Dots–PMMA Nanocomposite Waveguides," IEEE Sensors Journal, E. H. Yang, eds, **12**(10), pp. 3069-3074, E. H. Yang, DOI: 10.1109/JSEN.2012.2210037, available from: http://ieeexplore.ieee.org.

[41] Liu, W., Zhang, Y., Wu, H., Feng, Y., Zhang, T., Gao, W., Chu, H., Yin, J., Cui, T., Wang, Y., Zhao, J., Yu, W. W., 2014, "Planar temperature sensing using heavymetal-free quantum dots with micrometer resolution," Nanotechnology, **25**, IOP Publishing Ltd, UK, doi:10.1088/0957-4484/25/28/285501.

[42] Wang, H., Yang, A., Chen, Z., and Geng, Y., 2014, "Reflective Photoluminescence Fiber Temperature Probe Based on the CdSe/ZnS Quantum Dot Thin Film," Optics and Spectroscopy, **117**(2), pp. 235-239, Pleiades Publishing, Ltd.

[43] Bastida, G. d., Arregui, F. J., Goicoechea, J., and Matias, I. R., 2006, "Quantum Dots- Based Optical Fiber Temperature Sensors Fabricated by Layer-by-Layer," IEEE Sensors Journal, **6**(6), pp. 1378-1379, Eugenii Katz, eds, DOI: 10.1109/JSEN.2006.884436, available from: http://ieeexplore.ieee.org.

[44] He-lin, W., Ai-jun, Y., and Cheng-hua, S., 2013, "Luminescent high temperature sensor based on the CdSe/ZnS quantum dot thin film," Optoelectronics Letters, **9**(6), pp. 421-424, Tianjin University of Technology and Springer-Verlag Berlin Heidelberg.

[45] Larrion, B., Hernaez, M., Arregui, F. J., Goicoechea, J., Bravo, J., and Matias, I. R., 2009, "Photonic Crystal Fiber Temperature Sensor Based on Quantum Dot Nanocoatings," Journal of Sensors, Hindawi Publishing Corporation, doi:10.1155/2009/932471

[46] Shepherd, M., 2012, "Correct Sampling of Diffraction Limited Images," California Institute of Technology, online document, available at: http://wiki.astro.cornell.edu/twiki/pub/CCAT/CCAT_Memos/DiffractionLimitedSampling111212.pdf.

[47] Li, S., Zhang, K., Yang, J., Lin, L., and Yang, H., 2007, "Single Quantum Dots as Local Temperature Markers," Nano Letters, **7**(10), pp. 3102-3105, American Chemical Society.

[48] Yu, H. C. Y., Leon-Saval, S. G., Argyros, A., and Barton, G. W., 2010, "Temperature effects on emission of quantum dots embedded in polymethylmethacrylate", Applied Optics, **49**(15), Optical Society of America.

[49] Valerini, D, Cretí, A., and Lomascolo, M., 2005, "Temperature dependence of the photoluminescence properties of colloidal CdSe/ZnS core/shell quantum dots embedded in a polystyrene matrix," Physical Review B, **71**.

[50] Shen, Y, 2008, "Photoluminescence spectral study of single CdSe/ZnS Colloidal Nanocrystals in Poly(methyl methacrylate) and Quantum Dots molecules," Ph.D. thesis, UC, San Diego, local identifier: b6636099, available from: https://escholarship.org/uc/item/8w79q35z

[51] Maruyama, H., Masuda, T, and Arai, F., 2011, "LOCAL TEMPERATURE MEASUREMENT AND CONTROL USING FUNCTIONAL GEL-TOOL CONTAINNING A QUANTUM DOT BY COLOR ANALYSIS OF FLUORESCENCE SPECTRUM," *15th International Conference on Miniaturized Systems for Chemistry and Life Sciences*, pp. 1953-1955, Seattle, Washington, USA.

[52] Annoni, J., Green, A., and Puerto, M., 2012, "TEMPERATURE DEPENDENCE OF THE ENERGY GAP OF INP QUANTUM DOTS: A SOPHOMORE-LEVEL NANOMATERIALS EXPERIMENT," American Society for Engineering Education.

[53] Franceschetti, A., 2007, "First-principles calculations of the temperature dependence of the bandgap of Si nanocrystals," Physical Review B, **76**.

[54] Varshni, Y., 1967, "Temperature Dependence of the Energy Gap In Semiconductors," Physica, **34**, pp. 149-154.

[55] Cheng, C. and Yan, H., 2009, "Bandgap of the core–shell CdSe/ZnS nanocrystal within the temperature range 300–373 K," Physica E, **41**, pp. 828-832.

[56] Torchynska, T., 2012, "InAs Quantum Dots in Symmetric InGaAs/GaAs Quantum Wells," *Fingerprints in the Optical and Transport Properties of Quantum Dots*, pp. 153-180, Intech, A. Al-Ahmadi, eds, ISBN: 978-953-51-0648-7, available from: http://www.intechopen.com/books/fingerprints-in-the-optical-and-transportproperties-of-quantum-dots/inas-quantum-dots-in-symmetric-ingaas-gaas-quantum-wells, Chap. 6.

[57] Ru, E. L., Fack, J., and Murray, R., 2003, "Temperature and excitation density dependence of the photoluminescence from annealed InAs/GaAs quantum dots," Physical Review B, **67**(24), DOI: http://dx.doi.org/10.1103/PhysRevB.67.245318.

[58] Pugh-Thomas, D., Walsh, B., and Gupta, M., 2011,"CdSe(ZnS) nanocomposites luminescent high temperature sensor," Nanotechnology, **22**(18), doi: 10.1088/0957-4484/22/18/185503.

[59] Allahverdi, C. and Yukselici, M., 2008, "Temperature dependence of absorption band edge of CdTe nanocrystals in glass," New Journal of Physics, **10**.

[60] Lee, J. J., Dutton, J. C., and Jacobi, A. M., 2007, "Application of Temperature-Sensitive Paint for Surface Temperature Measurement in Heat Transfer Enhancement Applications," Journal of Mechanical Science and Technology, **21**, pp. 1253-1262.

[61] Shibuya, A., Ueki, R., Suzuki, Y., and Tange, 2016, M., "Temporal Temperature Distribution Measurement Of A Heat Transfer Surface Of A Flow Boiling Heat Sink With A Micro-Gap Using Temperature Sensitive Paint," Proceedings of the First Pacific Rim Thermal Engineering Confernece,

[62] Kurits, I, 2008, "QUANTITATIVE GLOBAL HEAT-TRANSFER MEASUREMENTS USING TEMPERATURE SENSITIVE PAINT ON A BLUNT BODY IN HYPERSONIC FLOWS," MS. Thesis, UMD, College Park, Maryland, USA.

[63] Bhandari, P., 2012, "Evaluation and Improvement Of Temperature Sensitive Paint Data Reduction Process Through Analysis Of Tunnel Data," MS. Thesis, UMD, College Park, USA.

[64] Schramm, J. M., Hannemann, K., Ozawa, H., Beck, W., and Klein, C., 2015, "Development Of Temperature Sensitive Paints For The High Enthalpy Shock Tunnel Gottingen, HEG," 8th European Symposium on Aerothermodynamics for Space Vehicles.

[65] Huang, C., 2005, "Molecular Sensors for MEMS," PhD. Thesis, PURDUE UNIVERSITY GRADUATE SCHOOL, West Lafayette, Indiana, USA

[66] Yang, L., Erdem, E., and Kontis, K., 2011, "Application of Pressure-and Temperature-Sensitive Paint in a Hypersonic Double Ramp Flow," 28th International Symposium on Shock Waves, pp. 759-765

[67] Ozawa, H., Laurence, S. J., Martinez Schramm, J., Wagner, A., and Hannemann, K., 2014, "Fast-response temperature-sensitive-paint measurements on a hypersonic transition cone," International Journal of Multiphase Flow, **56** (2015), doi:10.1016/j.ijmultiphaseflow.2011.11.012.

[68] Long, S. R., 2011, "a Temperature-Corrected Dual-Luminophore Pressure-Sensitive Paint System," BS. Thesis, Ohio State University, USA

[69] Huang, C., Li, C., Wang, H., and Liou, T., 2013, "The application of temperature-sensitive paints for surface and fluid temperature measurements in both thermal developing and fully developed regions of a microchannel," Journal of Micromechanics and Microengineering, doi:10.1088/0960-1317/23/3/037001

[70] Kose, M. E., 2005, "Multi-Luminophore Coatings For Pressure Sensitive Paint Applications," PhD. Thesis, University of Florida, USA

[71] Sefiane, K., Moffat, J. R., Matar, O. K., and Craster, R. V., 2008, "Self-excited hydrothermal waves in evaporating sessile drops," Applied Physics Letters, **93**, American Institute of Physics

[72] Garnier, N., Chiffaudel, A., and Daviaud, F., 2006, "Hydrothermal Waves in a Disk of Fluid," *Dynamics of Spatio-Temporal Cellular Structures*, pp. 147-161, Springer, New York, I. Mutabazi, J. E. Wesfreid, eds, ISBN: 978-0-387-25111-0, available from: http://link.springer.com/chapter/10.1007%2F978-0-387-25111-0_8, Chap. 8.

[73] Brutin, D., Zhu, Z., Rahli, O., Xie, J., Liu, Q., and Tadrist, L., 2010, "Evaporation of Ethanol Drops on a Heated Substrate Under Microgravity Conditions," Microgravity Science Technology, **22**, pp. 387-395, Springer Science+Business Media B.V., DOI: 10.1007/s12217-010-9200-2.

[74] Brutin, D., Sobac, B., Rigollet, F., and Niliot, C. L., 2011, "Infrared visualization of thermal motion inside a sessile drop deposited onto a heated surface," Experimental Thermal and Fluid Science, **35**, pp. 521-530, doi:10.1016/j.expthermflusci.2010.12.004.

[75] Karapetsas, G., Matar, O. K., Valluri, P., and Sefiane, K., 2012, "Convective Rolls and Hydrothermal Waves in Evaporating Sessile Drops," Langmuir, **28**, pp. 11433-11439.

[76] Nukiyama, S., 1934, "The Maximum and Minimum Values Of The Heat Q Transmitted From Metal To Boiling Water Under Atmospheric Pressure," International Journal of Heat and Mass Transfer, **9**, pp. 1419-1433

[77] Carey. V. P., 2008, "Pool Boiling," *Liquid-Vapor Phase-Change Phenomena*, pp. 253-344, Taylor & Francis Group, LLC, New York, S. Scholls, eds, ISBN: 1-59169-035-8, Chap. 7.

[78] Patankar, N. A., 2010, "Supernucleating surfaces for nucleate boiling and dropwise condensation heat transfer," The Royal Society of Chemistry, **6**, pp. 1613-1620, DOI: 10.1039/b923967g

[79] Lobo, L. N., 2010, "Photographic Study of Nucleate Boiling On the Surface of a Heated Rod," MNG. Thesis, University of Toronto, Canada

[80] Hsu, Y. Y., 1962, “On the size range of active nucleation cavities on a heating surface,” Journal of Heat Transfer-Trans. ASME **84**, pp. 207–213.

[81] Kotthoff, S., Gorenflo, D., Danger, E., and Luke, A., 2006, “Heat transfer and bubble formation in pool boiling: Effect of basic surface modifications for heat transfer,” International Journal of Thermal Sciences, **45**, pp. 217-236, doi:10.1016/j.ijthermalsci.2005.01.011.

[82] Benjamin, R. J. and Balakrishnan, A. R., 1997, “Nucleation Site Density in Pool Boiling of Saturated Pure Liquids: Effect of Surface Microroughness and Surface and Liquid Physical Properties,” Experimental Thermal and Fluid Science 15 pp. 32-42

[83] Jung, J., Kim, S. J., and Kim, J., 2014, “Observations of the Critical Heat Flux Process During Pool Boiling of FC-72,” Journal of Heat Transfer, **136**, DOI: 10.1115/1.4025697

[84] Howard, A. H. and Mudawar, I., 1999, “Orientation effects on pool boiling critical heat flux (CHF) and modeling of CHF for near-vertical surfaces,” International Journal of Heat and Mass Transfer, **42**, pp. 1665-1688.

[85] Pioro, I. L., Rohsenow, W., and Doerffer, S. S., 2004, “Nucleate pool-boiling heat transfer. I: review of parametric effects of boiling surface,” International Journal of Heat and Mass Transfer, **47**, pp. 5033-5044, doi:10.1016/j.ijheatmasstransfer.2004.06.019.

[86] Zhao, Y., Tsuruta, T., and Ji, C., 2003, “Experimental study of nucleate boiling heat transfer enhancement in confined space” Experimental Thermal and Fluid Science, **28**, pp. 9-16

[87] Kandlikar, S. G., 2002, “Insight into Mechanisms and Review Of Available Models For Critical Heat Flux (CHF) In Pool Boiling,” 1st international Conference on Heat Transfer, Fluid Dynamics and Thermodynamics, kruger National, South Africa.

[88] Stephan, K. and Abdelsalam, M., 1980, “Heat-Transfer Correlations For Natural Convection Boiling,” International Journal of Heat and Mass Transfer, **23**, pp. 73-87.

[89] Sakashita, H., 2015, “Pressure effect on CHF enhancement in pool boiling of nanofluids,” Journal of Nuclear Science and Technology, **53**(6), pp. 797-802, DOI: 10.1080/00223131.2015.1072482., online document, available at: http://dx.doi.org/10.1080/00223131.2015.1072482

[90] Xiao, B. and Yu, B., 2007, “A fractal model for critical heat flux in pool boiling,” International Journal of Thermal Sciences, **46**, pp. 426-433.

[91] Nikolayev, V.S., Beysens, D. A., Lagier, G., Hegseth, J., 2001, “Growth of a dry spot under a vapor bubble at high heat flux and high pressure,” International Journal of Heat and Mass Transfer, **44**, pp. 3499-3511.

[92] Yu, C. and Mesler, R. B., 1977, “A Study of Nucleate Boiling Near The Peak Heat Flux Through Measurement of Transient Surface Temperature,” International Journal of Heat and Mass Transfer, **20**, pp. 827-840.

[93] Nikolayev, V. S., Beysens, D. A., Hegseth, J., and Garrabos, Y., 2000, “Boiling Crisis as a Non-Equilibrium Drying Transition,” 14th Symposium on Thermophysical properties, Boulder, Colorado

[94] Gao, M., Zhang, L., Cheng, P., and Quan, X., 2012, "An investigation of microlayer beneath nucleation bubble by laser interferometric method," International Journal of Heat and Mass Transfer, 57, pp. 183-189, online document, available at: http://dx.doi.org/10.1016/j.ijheatmasstransfer.2012.10.017

[95] Zuber, N., 1959, "Hydrodynamic Aspects of Boiling Heat Transfer," PhD. Thesis, University of California, USA

[96] Leinhard, J. H. and Dhir, V. K., 1973, Extended Hydrodynamic Theory of The Peak and Minimum Pool Boiling Heat Fluxes, National Aeronautics and Space Administration

[97] Kutateladze, S. S., 1948, "On the Transition to Film Boiling under Natural Convection," Kotloturbostroenie, (3), pp.10-12. (referenced in Kandlikar [86])

[98] Kutateladze, S. S., 1951, "A Hydrodynamic Theory of Changes in a Boiling Process under Free Convection," Izvestia Akademia Nauk, S.S.S.R., Otdelenie Tekhnicheski Nauk, (4), pp. 529 (referenced in Zuber [94]).

[99] Haramura, Y. and Katto, Y., 1983, "A New Hydrodynamic Model of Critical Heat Flux, Applicable Widely to Both Pool and Forced Convection Boiling On Submerged Bodies In Saturated Liquids," International Journal of Heat and Mass Transfer, **26**(3), pp. 389-399.

[100] Zhao, Y., Masuoka, T., and Tsuruta, T., 2002, "Unified theoretical prediction of fully developed nucleate boiling and critical heat flux based on a dynamic microlayer model," International Journal of Heat and Mass Transfer, **45**, pp. 3189-3197.

[101] Sefiance, K., Benielli, D., and Steinchen, A., 1998, "A new mechanism for pool boiling crisis, recoil instability and contact angle influence," Colloids and Surfaces A: Physicochemical and Engineering Aspects, **142**, pp. 361-373.

[102] Nikolayev, V. S. and Beysens, D. A., 1999, "Boiling crisis and non-equilibrium drying transition," Europhysics Letters, 47, pp. 345-351.

[103] Theofanous, T. G., Dinh, T. N., and Tu, J. P., and Dinh, A. T., 2002, "The boiling crisis phenomenon Part II: dryout dynamics and burnout," Experimental Thermal and Fluid Science, **26**, pp. 793-810.

[104] Xu, D. and Chen, J., 2013, "Accurate estimate of turbulent dissipation rate using PIV data," Experimental Thermal and Fluid Science, Elsevier Inc, **44**, pp. 662-672

[105] Končar, B., Krepper, E., and Egorov, Y., 2005, "CFD Modeling of Subcooled Flow Boiling For Nuclear Engineering Applications," Proceedings of the International Conference Nuclear Energy for New Europe

[106] Končar, B., and Matkovič, M., 2010, "Numerical Simulation of Turbulent Subcooled Boiling Flow in a Rectangular Channel," Proceedings of the International Conference Nuclear Energy for New Europe

[107] Kim, S., Ryu, S., Euh, D., and Song, C., 2017, "Experimental Study on the thermal stratification in a pool boiling with a horizontal heat source," Annals of Nuclear Energy **106**, pp. 235-246

[108] "CCD and CMOS Image Sensor Technologies," lecture Slide, course: CSE467, University of Washington Computer Science & Engineering, 2008, available from: https://courses.cs.washington.edu/courses/cse467 /08au/pdfs/lectures/07-cmos-ccd- imagers.pdf.

[109] Moaveni, S. and Kim, J, 2017, "An inverse solution for reconstruction of the heat transfer coefficient from the knowledge of two temperature values in a solid substrate," Inverse Problems in Science and Engineering, 25(1), pp. 129-153, DOI: 10.1080/17415977.2016.1161035

[110] Mills, A., 1997, "Optical oxygen sensors utilising the luminescence of platinum metal complexes," Platinum Metals Rev, **41**(3), pp. 115–127

[111] Kim, H.(2011), "Enhancement of critical heat flux in nucleate boiling of nanofluids: a state-of-art review," Nanoscale Research Letters, a Springer Open Journal, 6(415)

[112] Kim, H., DeWitt, G., McKrell, T., Buongiorno, J., and Hu L-w., On the quenching of steel and zircaloy spheres in water-based nanofluids with alumina, silica and diamond nanoparticles," International Journal of Multiphase Flow, Vol. 35, pp. 427-438.

[113] Unal, C., Daw, V., Nelson, R. A. (1993), "Unifying the controlling mechanism for the critical heat flux and quenching: the ability of liquid to contact the hot surface," ASME Journal of Heat Transfer, Vol. 114, pp. 972-982.

[114] Chu, I., No, H. C., and Song, C., 2013, “Visualization of boiling structure and critical heat flux phenomenon for a narrow heating surface in a horizontal pool of saturated water ,” International Journal of Heat and Mass Transfer, **62**, Elsevier Ltd, pp. 142-152.

[115] Chu, I., No, H. C., Song, C., and Euh, D. J., 2014, “Observation of critical heat flux mechanism in horizontal pool boiling of saturated water,” International Journal of Heat and Mass Transfer, **62**, Elsevier Ltd, pp. 189-199.

[116] Choi, J. Y., No, H. C., and Kim, J., 2016, “Development of a dry patch model for critical heat flux prediction,” International Journal of Heat and Mass Transfer, **100**, Elsevier Ltd, pp. 386-395.

[117] Rodgers, J. L. and Nicewander, W. A., 1988, “Thirteen Ways to Look at the Correlation Coefficient,” The American Statistician, **42**(1), pp. 59-66

[118] Teodori, E., Moita, A. S. , Teodori, E., and Moreira, A. L. N., 2013, “Evaluation of pool boiling heat transfer over micro-structured surfaces by combining high-speed visualization and PIV measurements,” 10TH INTERNATIONAL SYMPOSIUM ON PARTICLE IMAGE VELOCIMETRY – PIV13,

[119] Teodori, E., Moita, A. S., and Moreira, A. L. N., 2013, “Characterization of pool boiling mechanisms over micro-patterned surfaces using PIV,” International Journal of Heat and Mass Transfer, Elsevier, **66**, pp. 261-270.

[120] Filella, A., Ern, P., and Roig, V., 2015, "Oscillatory motion and wake of a bubble rising in a thin-gap cell," Journal Fluid Mechanics, **778**, Cambridge University Press, pp. 60-88.

[121] Wang, X., Wolfbeis, O., and Meier, R., 2013, "Luminescent probes and sensors for temperature," Chem Soc Rev, 42, pp. 7834-7869, DOI: 10.1039/c3cs60102a.

[122] Al Hashimi, H. and Kim, J., 2016, "Quantum Dot Temperature Sensor Ab Initio Test: Droplet Vaporization Heat Transfer," In ASME 2016 Heat Transfer Summer Conference collocated with the ASME 2016 Fluids Engineering Division Summer Meeting and the ASME 2016 14th International Conference on Nanochannels, Microchannels, and Minichannels (pp. V002T08A012-V002T08A012). American Society of Mechanical Engineers.

[123] Al Hashimi, H., Hammer, C., Lebon, M. and Kim, J., 2017, "Phase Change Heat Transfer Measurements Using Optical Techniques," 9th World Conference on Experimental Heat Transfer, Fluid Mechanics and Thermodynamics

[124] Al Hashimi, H., Hammer, C., Lebon, M., Zhang, D. and Kim, J., 2017, "Phase Change Heat Transfer Measurements Using Temperature Sensitive Paints," Journal of Heat Transfer, ASME